Interactions between Multi-Walled Carbon Nanotubes and Low-Pressure Glow Discharges in the Presence of Electric Fields

Leron Vandsburger

Doctoral Thesis

Department of Chemical Engineering

McGill University

Montréal, Québec

August 2013

Thesis submitted in partial fulfillment
of the requirements for the degree of
Doctor of Philosophy

EPIGRAPH

"The traveller hasteth in the evening"

ACKNOWLEDGEMENTS

It is my great pleasure to acknowledge the important contributions of both of my research supervisors to the completion of this challenging project. Professors Sylvain Coulombe and Jean-Luc Meunier have overseen the work I've done with patience, professionalism, and minimal severity. I have learned what seems to me to be an inordinate amount on many topics, including professional conduct, research techniques, and the French language. The lessons I have learned have come both from direct instruction and from observation of their methods. I have every confidence that both these lessons and their acquaintance will prove vital to me in my future career.

I would like to also acknowledge the collegial environment fostered by my groupmates in the Plasma Processing Lab. I have found frequent and significant inspiration in the atmosphere of critical debate and impassioned discussion of ideas. The full list is long, but I would like to specifically acknowledge Mr. Nathan Hordy, Mr. Felipe Aristizabal, Prof. Jocelyn Veilleux, Prof. Jason Tavares, and the new students Mr.s Mathew Evans and Mark McArthur.

I feel the need to acknowledge the expertise of the technical staff of the chemical engineering department. Mr. Ranjan Roy and Mr. Frank Caporuscio provided both advice and help without which I couldn't have achieved the results I've presented here.

A research department is a community that thrives on interdisciplinary cooperation. During my studies I benefited from many bilateral interactions with students and professors from other groups. Mr. Mehdi Dargahi and Prof. Sasha Omanavic deserve recognition for granting me access to their FT-IR microscope. I would also like to take this opportunity to thank Prof. Anne Kietzig for allowing me to give two lectures in her course this past year. Teaching is the privilege of a professor; and I was glad to be allowed the chance to be an imposter.

Finally, I would like to thank my family, who have been stalwarts throughout my studies. My parents gave consistent guidance to draw me in “the right direction.” My brothers provided me with an invaluable frame of reference by which to better understand my personal development during my time at McGill.

ABSTRACT

This thesis presents the systematic study of the interaction between Multi-Walled Carbon Nanotubes (MWNTs) and charged particles, in the presence of strong electric fields. MWNTs were energized by applying a strong Direct Current (DC) bias in order to recruit charged particles from a glow discharge. The MWNTs acted both as electrodes and as charged particle sinks by sustaining a glow discharge either locally on the MWNT-covered sample surface, or remotely via a capacitively coupled radio-frequency (RF) glow discharge. The intention of the work was to develop a holistic description of the degradation mechanism of MWNTs under charged particle bombardment, with specific explanations for the roles of ion bombardment, electron bombardment, and plasma-chemical reactions.

A dual-mode DC-RF plasma chamber was designed for the purpose of exposing MWNTs to plasma particles. Operating in DC mode allowed for the study of the combined effects of electric current and ion bombardment. RF operation facilitated the separation of the two effects by decoupling the generation of the plasma from the polarity of the MWNT surface bias. Plasma cations were recruited to the MWNT surface with a negative DC bias and electrons by a positive bias.

The composition of the plasma gas was carefully controlled to study the species produced during MWNT degradation. The plasma was studied with absorption and emission spectroscopy techniques. Chemical residues resulting from MWNT degradation were analyzed by GC-MS and FT-IR. Data from these measurements provided important findings that indicated two distinct effects of electron and ion bombardment, and a third effect of plasma-phase reactions.

Bombardment of energized MWNTs by oxygen cations was found to elicit tip-localized covalent functionalization. Absorption (OAS) and emission (OES) spectroscopy

and GC-MS data confirm that the oxidation is anhydrous and is caused first by adsorption of oxygen ions onto the surface MWNTs, with subsequent functionalization. In particular, OAS and GC-MS techniques identified 2,3-para napthalic anhydride as a stable product of MWNT oxidation. Single-point energy calculations confirm that this species is a stable product of MWNT oxidation.

MWNTs respond differently to electron bombardment, revealing the importance of MWNT resistivity in degradation mechanisms. It was found that electron bombardment causes thermal evaporation of CNTs in a similar tip-localized degradation pattern. The products of electron bombardment degradation were identified as short-chain unsaturated hydrocarbons in GC-MS. Time-resolved optical emission spectroscopy showed a kinetic behaviour that indicated the decoupling of gaseous carbon concentration from O_2 consumption. This finding indicates that short hydrocarbons are produced by MWNT degradation, rather than by plasma chemical reactions.

The effect of plasma composition was found to affect the plasma phase reactions that occurred during MWNT degradation. Plasma synthesis of polycyclic aromatic hydrocarbons (PAHs) and short pyrrolic plasma polymers was detected both in OAS and GC-MS. Plasma polymer deposits were detected on the MWNT surfaces by FT-IR measurements subsequent to degradation experiments. The synthesis of PAHs was sensitive to plasma composition. Synthesis of short PAHs was favoured in oxygen plasmas, while plasma polymers and larger PAHs were detected in nitrogen and argon plasmas.

ABRÉGÉ

Cette thèse présente l'étude systématique des phénomènes d'interaction présents entre les nanotubes de carbone à parois multiples (NTCPM) et les particules de gaz ionisées sous l'influence de champs électriques intenses. Afin d'attirer les particules de gaz chargées vers les NTCPM, une différence de potentiel, en courant continu, (DC) est appliquée sur les échantillons comportant les NTCPM. Il en résulte que ces derniers acquièrent de l'énergie de manière simultanée tout en attirant les particules chargées. Une décharge luminescente est soutenue de manière locale à la surface des NTCPM ou bien à distance éloignée par une décharge capacitive à radiofréquence (RF). Les nanotubes de carbone agissent à la fois comme des électrodes et à la fois comme des dissipateurs pour les particules de gaz chargées. L'intention primaire de cet ouvrage est de développer une description holiste du mécanisme de dégradation des NTCPM reliée à l'effet du bombardement ionique/électronique, tout en fournissant des explications spécifiques à propos du rôle que jouent ceux-ci ainsi que les réactions portant à la chimie des plasmas.

Un réacteur à plasma à nature double (DC - RF) a été conu dans le but d'exposer les échantillons comportant les NTCPM au plasma. Dans un premier temps, l'opération du réacteur en mode DC a permis l'étude des effets reliés au bombardement ionique et au courant électrique. Dans un second temps, l'opération en mode RF a facilité la ségrégation des deux effets mentionnés en découplant la génération du plasma de la polarité des NTCPM imposé par le biais DC. Les cations, produits dans le plasma, ont été attirés vers les NTCPM en appliquant une tension DC négative. D'une manière semblable les électrons ont été attirés par l'effet d'une tension DC négative.

La composition du gaz plasmagène a été sélectionnée et contrôlée rigoureusement dans le but d'étudier et d'observer les espèces produites lors de la dégradation des

NTCPM par bombardement. Le plasma généré a été analysé en employant des techniques de spectroscopie optique autant en absorption (SOA) qu'en émission (SOE). Les résidus provenant de ce procédé ont été analysés par chromatographie en phase gazeuse couplé à la spectroscopie de masse (GC-MS) et par spectroscopie infra rouge par transformée de Fourier (FT-IR). Les données obtenues ont permises de découvrir deux effets distincts reliés au bombardement ionique de plus qu'un troisième effet portant à la chimie des plasmas.

Le bombardement des échantillons avec des cations d'oxygène a permis de susciter la fonctionnalisation en pointe des NTCPM. L'oxydation des nanotubes est de nature anhydre et provient, en premier lieu, de l'adsorption du cation d'oxygène en surface de l'échantillon et, en deuxième lieu, de la fonctionnalisation de ces derniers. Ceci a été confirmé par la SOA, la SOE ainsi qu'avec le GC-MS. Le 2,3-para naphthalic anhydride a été identifié comme étant un produit stable du procédé d'oxydation des NTCPM. Des calculs d'énergie en point unique confirment que cette espèce chimique est un produit stable provenant de la réaction d'oxydation des NTCPM.

Les NTCPM réagissent de manière différente au bombardement électronique qu'au bombardement électronique. Cette différence démontre l'influence et l'importance de la résistivité électrique des NTCPM lors de l'étude du mécanisme de dégradation. Il a été observé que le bombardement électronique des NTCPM cause l'évaporation thermique en pointe de ceux-ci. Les produits de cette réaction ont été identifiés via des analyses au GC-MS comme étant des hydrocarbures non-saturés à chaine courte. Les mesures de SOE résolue dans le temps démontrent un comportement cinétique indiquant le découplage du carbone en phase gazeuse de la consommation d'O_2. Ceci indique que bel et bien des hydrocarbures à chaine courte sont produits par la dégradation des NTCMP plutôt que par la chimie des plasmas.

La composition du gaz plasmagène a un effet sur les réactions en phase plasma

qui prennent place lors de la dégradation des NTCPM. La synthèse par plasma des hydrocarbures aromatiques polycycliques et des polymères pyrroliques a été observée en employant la SOA ainsi que le GC-MS. Des dépôts de polymères synthétisés par plasma ont été détectés à la surface des nanotubes de carbone par des mesures de FT-IR prises suite aux expériences de dégradation. La synthèse des hydrocarbures aromatiques polycycliques parait tre sensible par rapport à la composition du gaz plasmagène. Ces derniers sont favorisés par l'utilisation d'un plasma d'oxygène, tandis que les polymères synthétisés par plasma et les hydrocarbures aromatiques polycycliques plus larges ont été détectés en utilisant des plasmas d'azote et d'argon.

STATEMENT OF CONTRIBUTIONS

This manuscript-based thesis contains three chapters that were either published or accepted for publication in peer-reviewed journals:

i Chapter 4 has been published as Degradation of Carbon Nanotubes in Low-Pressure Oxygen Glow Discharges in CARBON, Vol. 57, No. 0, pp. 248-258 (2013).

ii Chapter 5 has been Published as Electron Bombardment Degradation of Carbon Nanotubes in Radio Frequency Discharge Afterglows in the Journal of Physics D: Applied Physics 46-47 485301 (2013).

iii Chapter 6 has been accepted for publication in Plasma Processes and Polymers as Carbon Nanotube–Polypyrrole Composite Electrode Materials Produced by Electron Bombardment in Radio Frequency Afterglows.

The three manuscripts were authored by Leron Vandsburger (the Ph.D. candidate), Sylvain Coulombe, and Jean-Luc Meunier (the research supervisors). The articles were written by the Ph.D. candidate based on the research work he accomplished over the course of his project. The work was primarily experimental, with limited validation by theoretical methods. The research supervisors provided guidance and suggestions throughout the project and revised the manuscripts before submission.

CONTENTS

LIST OF FIGURES

LIST OF TABLES

CHAPTER 1

INTRODUCTORY MATERIAL

1.1 Project Impetus

It often happens during the exploration of a new scientific field that the development of new and useful applications outpaces the fundamental understanding of the field's underlying phenomena. Existing techniques and approaches to problem solving can be adapted, and can meet with success, without waiting for any theoretical explanation to address the differences between the new system and those that preceded it. Opportunities for theoretical groundwork arise, however, when the adapted techniques do not yield the expected results. Such problems can only be solved by working out an understanding of the physical and chemical phenomena that can lead to the intended results, and then exploiting them properly.

Nanotechnology is a young field, but has already produced many important developments and applications. Graphitic carbon has become in a matter of two decades, the intended solution to many of the most pressing issues facing technologists and scientists, alike. Graphene, for example, is being explored to replace metals and transparent conductors in display technology, to develop supercapacitors that will one day replace batteries, and to form the basis for a whole array of sensor technologies to detect everything from biomarkers to toxic gases. Carbon nanotubes (CNTs), which are the focus of this work, have already found successful application in composite materials, nanofluid suspensions for numerous purposes, and nano-electronics. CNTs are also being targeted for application in varied sensor devices and as bio-compatible electrodes.

The molecular structure of CNTs leads to an inherent chemical stability and anisotropic electrical and heat conductivity. These properties, in turn, are the source of

the potential for implementation of CNTs in so many different applications. Electrical conductivity and thermal stability have already been exploited to produce successful improvements on high voltage electron sources, under high vacuum, and with this success came a rapid burst in development of CNT-based enhancements to many types of electrode materials.

In order to explain the mechanism of operation of CNT field emitters, it was initially thought that CNTs could be approximated as nanoscale metal wires. The effectiveness of CNT electron emitter technology was attributed to one-dimensional quantum confinement in the axial direction and nanoscale field enhancement, termed the "field enhancement effect". Although this approach adequately described the successful operation of CNT emitters, experimental work probing the extremes of stability revealed significant deviations from the metal nanowire description. CNT emitters were found to be sensitive to many factors, as a consequence of imperfections in the CNT graphitic lattice, termed "defects", formed during synthesis. Electrical current was found to cause changes in CNT molecular structure, which in turn affected CNT morphology. Thermal effects such as evaporation and melting were observed. Under alternating current, field-induced mechanical vibrations could cause structural failure of CNT-emitters. The effect of pressure proved important, and the impact of ion bombardment on CNT stability was very quickly identified as a cause of instability and failure in CNT emitters.

The effect of pressure on the chemical stability of electrified CNTs has been studied by experimental and theoretical work on CNT-plasma interactions. Plasmas are energized gases containing ion, electron, and neutral constituents. A plasma is ignited when the gas is ionized, causing charge separation to the point that collisional processes become self-sustaining. This can happen spontaneously in high-voltage applications such as CNT electron-emitters, but can be elicited by direct electron beam ionization or by UV-excitation. Development in the field of CNT-plasma interactions has been rapid and

vigorous, and work on surface chemical functionalization has been leading the charge toward applications of CNTs in unconventional media and composites.

CNT functionalization by plasma treatment is a recent development, but it has already proven useful in many ways. It allows for the tailoring of CNT chemical properties, such as hydrophilicity, without the problematic requirement of suspension in liquid media. CNT-nanometal hybrid materials can be produced easily, and plasma polymerization reactions produce improved compatibility with polymer phases and with biological environments. That being said, the technique is still in its infancy with respect to fundamental understanding, and there is much that is still unclear about the processes of CNT functionalization by plasmas. For that reason, the principal goal of this doctoral study has been to develop a detailed explanation for the chemical processes that occur during exposure of CNTs to ion and electron bombardment in low-pressure applications.

1.2 Detailed Objectives

In the effort to understand the overall chemistry of CNT-plasma interactions, the various potential effects of plasma exposure were identified for isolated study. The system that was chosen comprised energized CNTs acting as nanostructured electrodes and either a locally or remotely sustained plasma. The specific objectives that have been achieved by this doctoral work were as follow:

- To delineate the mechanism of electric field-induced degradation of CNTs by exposure to low-pressure non-thermal glow discharges;
- To understand the respective effects of ion and electron bombardments in the CNT degradation mechanism;

- To explain the effect of plasma composition on CNT chemical reactivity in the presence of both ion and electron bombardment;
- To develop a mechanistic explanation for the covalent functionalization of CNTs by exposure to oxygen plasma;
- To identify potential applications based on the techniques developed.

1.3 Structure of the Thesis

This is a manuscript-based thesis, comprising a total of 7 chapters. A detailed introductory section has been prepared to provide the necessary background information on plasmas, carbon nanostructured materials, CNT-plasma interactions, and experimental and computational techniques used, but not explained, in the following chapters. A total of three manuscripts have been prepared, resulting from work on the previously stated objectives, and these will make up the bulk of the thesis itself. Chapter 3 will provide detailed information on the methodology used for experimental investigations of CNT-plasma interaction. Each subsequent chapter will be taken from the manuscripts accepted, submitted, or to be submitted. Chapter 4 has been published as *"Degradation of Carbon Nanotubes in Low-Pressure Oxygen Glow Discharges"* in *CARBON*, and addresses the first and second objectives. Chapter 5 has been accepted for publication in *Journal of Physics D: Applied Physics* as *"Electron Bombardment Degradation of Carbon Nanotubes in Radio Frequency Discharge Afterglows"*, and addresses the third and fourth objectives. Chapter 6 addresses the final objective. It has been submitted to *Plasma Processes and Polymers* as *"Carbon Nanotube-Polypyrrole Composite Electrode Materials Produced by Electron Bombardment in Radio Frequency Afterglows"*. Each chapter that has been written as a manuscript is preceded by a preface that describes the relevance of the chapter to the doctoral work as a whole.

CHAPTER 2

THEORETICAL BACKGROUND

The following chapter presents the necessary theoretical basis for the thesis, preceding the descriptions of the methods and hypotheses. Each section contains both a review of important literature and a detailed summary of material available in reference texts. Whenever possible this section avoids repeating subject matter that has been presented in subsequent chapters. Some redundancy, however, is inevitable. This chapter covers the fundamentals of plasmas, including physics and chemistry topics. Next, the synthesis, properties, chemistry, and applications of carbon nanotubes are covered.

2.1 Plasmas

Non-thermal plasma treatment and the interaction of CNTs with plasmas are the main subjects of this thesis, so it is important to provide descriptions of the basic principles of plasma science. This section addresses the physics of plasmas, such as collisional processes and thermalization, and the types of plasmas and their generation. This section also discusses the important topic of energy distribution functions, in connection with thermal equilibrium. A brief section will also focus on topics of plasma chemistry, such as plasma polymerization and cyclization. The primary source for this section is the work entitled, *Physics of Collisional Plasmas: Introduction to High-Frequency Discharges* [Moisan and Pelletier, 2012]. The discussion of excitation/de-excitation is supplemented with material from works by Herzberg [Herzberg, 1944]. These sources are referenced globally here to avoid repeatedly referencing the same works in subsequent sections.

2.1.1 Fundamentals of Plasmas

The basic principle of plasmas is that their constituent particles interact over relatively large distances when compared to what is typical of gaseous phases. This is a result of the presence of charged particles in the plasma, as both electrons and ions, in addition to neutral gas particles. These charged particles exert Coulomb forces upon one another that far outweigh the effects of van der Waals forces, which govern the behaviour of neutral phases. This is true for both plasmas and ionized gases, where the difference is in the degree of ionization, which refers to the fraction of particles in the gas that are charged. The degree of ionization is typically calculated assuming the single ionization of gas particles, and is the number fraction of ions in the gas. It can range from full ionization (100%), as in stellar plasmas, to very low degrees of ionization ($10^{-10} - 10^{-6}$) in weakly ionized gases [Conrads and Schmidt, 2000]. An ionized gas can be said to behave like a plasma when the degree of ionization is greater than 10^{-6}[Moisan and Pelletier, 2012]. For processing plasmas the degree of ionization is typically in this range, from 10^{-6} to 10^{-1} [Christophorou and Olthoff, 2004]. Since cold plasmas are not fully ionized, they contain a large percentage of neutral gas atoms or molecules and neutral particles far outnumber the charged particles in most plasma applications.

A plasma contains both positive and negative ions that interact with each other, with free electrons in the plasma, and with photons that are both emitted by excited particles in the plasma and that are introduced externally. This leads to a large number of possibilities for energy to be exchanged between particles, either by absorption of electrons or photons or by collisions with ions and electrons. These are termed collisional processes, and are characterized by measures of probability, called cross-sections, that are specific to the type of interaction that is occurring. Collision cross-sections are expressed in terms of an effective cross sectional area of a particle, and are dependent on the energies

of both of the participating particles. In the case of an electron absorption collision, for example, the cross section would be calculated for the gas atom or molecule that would absorb the electron, and would be dependent on the energy of the gas particle and on the energy of the incident electron. Each type of collision is highly sensitive to these energies, and often each will have a specific range of energies over which it will be the dominant form of collision for the particles in the plasma.

The free electrons in the gas are driven by an externally applied electric field, which imparts to them the energy necessary to further ionize other neutral particles in the gas. Ionization collisions release newly freed electrons that, in turn, ionize more neutral particles in a process called the electron ionization avalanche. Ionization impact collisions are the necessary first step to forming a conductive medium in the gas that leads to the eventual formation of a completely ionized plasma. Electron absorption collisions occur simultaneously with ionization, thereby opposing the trend toward thermalization. For this reason, the power requirement for igniting and sustaining a plasma includes the energy that must be provided to counteract the neutralization of ions.

The relative energies of the different types of particles in a plasma are important for determining the dominant collisional processes, but they are also useful to characterize the plasma. Assuming that single-ionization is most common, electrons and ions are typically considered to be present in equal densities in a plasma. That being said, they are not necessarily at equivalent average energies. The kinetic energy of the particles in a plasma is related to temperature through the Boltzmann constant. In cold plasmas, there is a large difference between the temperature of the electrons and the temperatures of the heavy species in the the gas. The electron temperature, denoted by T_e, is generally larger than the gas temperature, T. This occurs as a result of the higher mobility of electrons, relative to ions and neutral particles. Electrons respond more rapidly to electric fields than ions, owing to their considerably smaller mass, so electron-electron elastic

collisions occur more frequently. The resulting momentum transfer between electrons leads to an increase in kinetic energy, and thus temperature.

Collisions also lead to momentum transfer between electrons and both neutrals and ions. The effect of elastic collisions between electrons and heavy species on the momentum of the heavy particle is small, due again to the great disparity in masses between the two types of particles. Nonetheless, the gas temperature is affected by the electron temperature in systems where the collision frequency is high. Although each electron-ion or electron-neutral collision transfers little energy, the combined effect of all the collisions in a plasma can lead to an increase in the gas temperature to approach the electron temperature. Thermalization is the term used for this process involving the equalization of the two temperatures. Pressure is an important parameter leading to thermalization, since the frequency of collisions is directly tied to particle density. Thermalization leads to a state of thermal equilibrium, which occurs when the two temperatures are equal. This also serves as the definition of an equilibrium plasma.

An important topic to discuss when considering collisional processes is electron energy distribution functions, because this helps to explain the previously outlined concept of collision cross-sections. The electrons in a plasma can usually be assumed to be in equilibrium between themselves. As such, there is a certain probability that an electron will be found at a specific energy, based on various properties of the plasma such as pressure, T_e, the electron density, and other more specific quantities that depend on the type of distribution that is observed. The Maxwell-Boltzmann energy distribution function (EDF) is typically found to be accurate when describing the electron energy distribution, but plasma waves and other electrodynamic phenomena can cause deviations from this behaviour [Moisan and Pelletier, 2012]. The equation is shown symbolically in Eq. 2.1, where E is the energy, k is the Boltzmann constant, and T is the average electron temperature, T_e. The function has also been plotted for three values of energy in Fig.

2.1. This equation not only applies to electrons, but also to ions and neutrals when the plasma in in thermal equilibrium.

$$f_E\, dE = 2\sqrt{\frac{E}{\pi}}\left(\frac{1}{kT}\right)^{3/2} \exp\left[\frac{-E}{kT}\right] dE \tag{2.1}$$

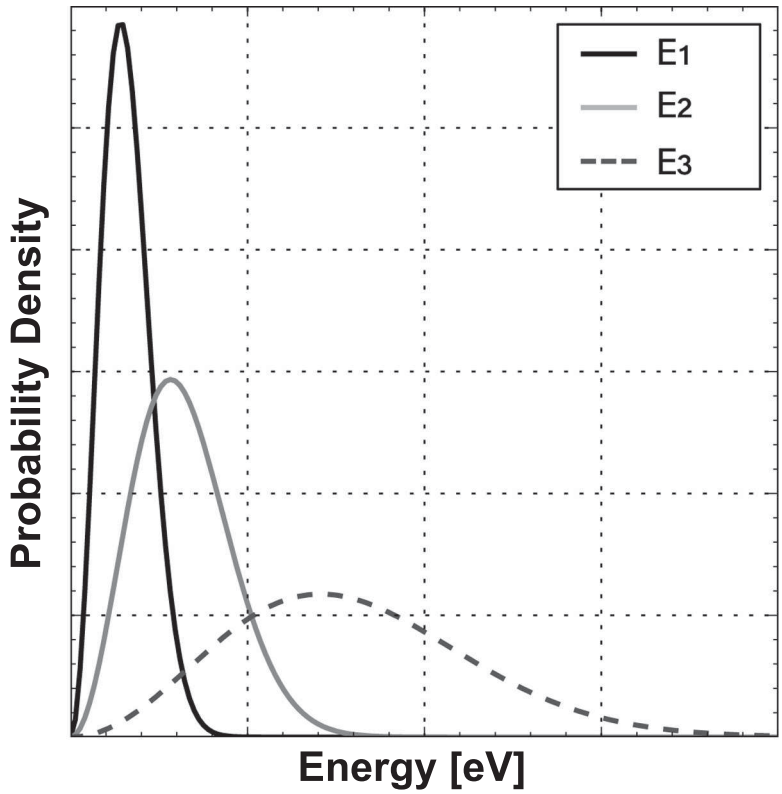

Figure 2.1: The Maxwell-Boltzmann energy distribution function for three average temperatures in increasing order From E1 to E3

The EDF reveals that a significant number of electrons can be observed with enough energy to elicit a desired reaction, even when the average temperature of the electrons in a plasma may be below the energy of that particular collision. The importance of this effect is such that it is understood that most plasma processes are caused by the most energetic electrons in a plasma, while the majority of the free electrons in a plasma

contribute relatively little. The EDF also shows that the largest number of electrons are found in a particular region of the energy spectrum. This indicates that the collisions whose energies are nearest to that region of the EDF will be preferred in the plasma over other transitions that have energy requirements both higher and lower. The effect of the electron energy distribution is important when designing plasma systems, since ionization collisions are required to sustain the plasma. Enough electrons must be present with the correct energy to cause ionization in the plasma gas to outweigh the effect of electron capture and ion neutralization. This is closely connected to operating parameters, such as electrode gap, operating voltage, operating pressure, and plasma gas composition.

2.1.2 Plasma System Design

The manner of producing plasmas depends most on the intended application, with the energy density requirement and reactivity of the system being two important factors. The technologies can be classified by the type of imposed electric fields that are used to generate the plasma. In general, these are standing fields and alternating fields, but the alternation frequency is very important, so plasmas are typically classified as either low-frequency or high-frequency. Low frequency discharges extend from 0 Hz, or direct current, to up to 1 MHz, where the radio-frequency spectrum is said to begin. High frequency plasmas can use excitation frequencies either in the radio-frequency range, up to 100 MHz, or in the microwave spectrum that extends to the GHz range.

The effect of exposure to non-thermal plasmas on chamber materials is minimal, even though electron temperatures can easily reach values over 10,000 K. This is due to the minuscule mass of electrons and the corresponding low level of energy transfer per elastic collision between electrons in the plasma and the chamber walls. The low gas temperatures of non-thermal plasmas make it possible to construct plasma devices from

a wide variety of materials, while sustaining an electron temperature that is sufficient for energetic reactions to occur.

Inert systems, like fluorescent lamps, can use electrodes in direct contact with the plasma. For DC plasma systems, the electrodes must be immersed in the plasma to close the circuit across the discharge gap. Highly reactive systems or systems that require strict isolation of the plasma, on the other hand, use external electrode designs that operate at frequencies above 1 MHz. The basic types of plasma electrode configurations are shown schematically in Fig. 2.2. Dielectric barrier discharges (DBD) are an important example of atmospheric pressure discharge that operate at the full range of operating frequencies from DC to RF [Conrads and Schmidt, 2000]. DBD electrodes are covered in ceramic dielectric materials to prevent the glow-to-arc transition, and can operate in either glow discharge or streamer modes. In Fig. 2.2 the two modes are shown in the same diagram, although the combination is not possible in actual systems.

Glow discharges produce diffuse non-thermal plasmas that are characterized by low degrees of ionization (10^{-6}-10^{-4}) and low electron densities (10^{8}-10^{12} cm^{-3}) [Conrads and Schmidt, 2000, Eliasson and Kogelschatz, 1991]. They are frequently used as light-sources and as a mild means of affecting surface treatments, such as biological sterilization and sputter coating/etching. Among the many possible collisions that occur between the particles in the plasma, two equally important types of inelastic collisions are excitation and electron absorption/capture. Non-thermal plasmas are particularly well suited for plasma chemistry, since these collisions lead to an high average density of free-radicals relative to thermalized plasmas. This attribute makes them more appropriate for radical-reactions such as polymerization and cyclization, both of which are discussed in this thesis.

Many means exist for producing non-thermal plasmas, which depend closely on the desired operating pressure. In general all ranges of frequencies are possible, especially

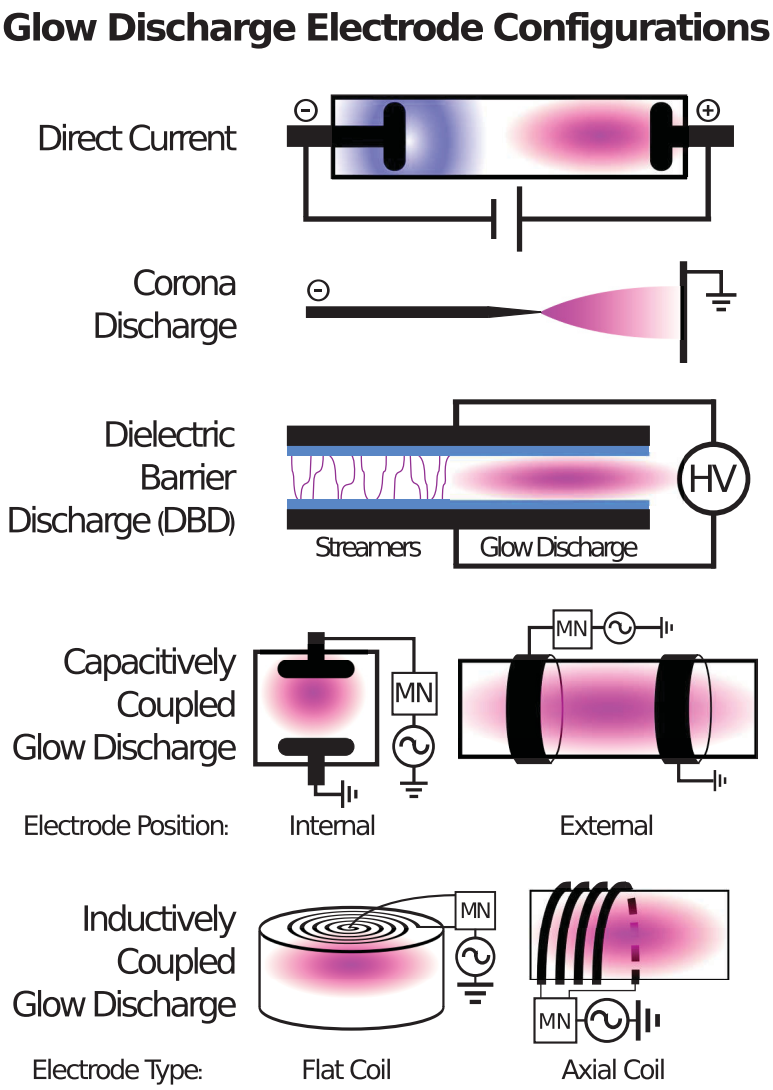

Figure 2.2: Diagram showing common electrode arrangements for important types of non-thermal plasmas. The DC glow-discharge is shown with the negative glow and positive column. Capacitively coupled RF discharge is shown with both an internal and external electrode arrangements.

when using DBDs. Capacitively and inductively coupled radio frequency discharges may be ignited remotely at low operating pressures, but this is not possible at high pressures. At atmospheric pressure or higher, the voltage requirements for sustaining a plasma become considerable and require the constriction of the inter-electrode gap distance. Dielectric barrier discharge designs or corona discharges are commonly used to produce plasmas under such conditions. Since this project used only low-pressure DC and RF capacitively coupled plasma sources, further description of plasma sources is omitted in the interest of brevity. A short list of the technologies available to produce non-thermal plasmas and their applications is given in Table 2.1 [Conrads and Schmidt, 2000, Eliasson and Kogelschatz, 1991]. The operating parameters are given as order-of-magnitude ranges, because the actual values depend greatly on system parameters. The electron temperatures given for DC discharges describe the positive column and the negative glow (in parentheses). The negative glow is a region that forms near the surface of the cathode and is the region where the largest voltage drop occurs. Electrons in the negative glow are at a much higher energy than in the rest of the plasma. The positive column forms in the volume and can scale to fill the volume between the anode and a dark-space that follows the negative glow. It is the positive column that is used for light generation in fluorescent lamps. Both the negative glow and the positive column are shown in the DC discharge diagram in Fig. 2.2.

2.1.3 Plasma chemistry, plasma polymerization, and radical cyclization

Plasmas offer the possibility of producing targeted reactions between energized gaseous species and solid or liquid surfaces in a way that is not possible with conventional chemistry methods [Yasuda, 1985]. The composition of the reacting medium can be controlled in many ways, such as through the plasma power, plasma density, and plasma composition. Unlike conventional wet chemistry, continuous synthesis systems are

Table 2.1: Summary of Non-Thermal Plasma Technologies

Plasma Type	**Operational Window**	**Application(s)**
Direct Current - Glow Discharge	P: 1 mtorr - 760 torr T_e: 1-10 eV (100 eV) n_e: 10^8-10^{11} cm^{-3}	Light Sources Sputter/Etching
Corona Discharge	P: 760 torr T_e: 5 eV n_e: 10^{13} cm^{-3}	Electrostatic-Precipitation GC-MS
Dielectric Barrier - Discharge	P: 760 torr T_e: 5 eV n_e: 10^{13} cm^{-3}	Surface Treatment Plasma Display
Capacitively Coupled - Glow Discharge	P: 1 mtorr - 10 torr T_e: 1-10 eV n_e: 10^{11} cm^{-3}	Chemical Processing
Inductively Coupled - Glow Discharge	P: 1 mtorr - 10 torr T_e: 1-10 eV n_e: 10^{12} cm^{-3}	Plasma Chemistry Diagnostics

fairly simple to achieve by confining the plasma to a small region in a flowing gas stream [Ostrikov et al., 2013]. This is the principle that underlies nano-powder synthesis/coating techniques and other reactions that are sensitive to kinetic parameters such as phase change. Charged particles in a plasma can be directed to a surface by electric fields, as is done in ion bombardment etching in the semiconductor industry [Christophorou and Olthoff, 2004]. This is also possible in wet chemistry, as is seen in electro-plating, but plasmas offer the added possibility of working with strict control on processing parameters, such as surface selectivity, nanoscale confinement, as well as specification of the EDF. Reactions within the plasma itself can also provide the reactants for complex organic synthesis of plasma polymers and polycyclic aromatic hydrocarbons [Yasuda, 1985].

Research into non-thermal plasmas and their interaction with surfaces has grown considerably in recent years, concurrent with the development of the field of nanoscience [Ostrikov et al., 2013]. This trend began mostly in the field of semi-conductor processing in the second half of the twentieth century, but it has now grown to include almost all fields of chemistry, biology, and physics. In many areas, non-thermal plasma treatment is the only solution for surface chemical treatments or modification. Sterilization of sensitive biological surfaces, for example, requires very low plasma energy densities [Artemenko et al., 2012], while semiconductor surface modification treatments require very strict control of surface flux to prevent thermal effects such as melting and annealing [Moisan and Pelletier, 2012]. Exposure of sensitive surfaces to even low power plasmas can cause significant degradation [Vandsburger et al., 2013a], as will be discussed in this thesis.

The high concentration of free radicals in low pressure plasmas that contain organic species leads to the spontaneous formation of polymeric materials that possess a high degree of cross-linking [Yasuda, 1985]. These are formed in the plasma itself, where

the radical density is highest, and are deposited on all the grounded surfaces of the plasma chamber as uniform films [Yasuda, 1985]. The presence of oxygen in the plasma limits the formation of plasma polymers, since the tendency is for the organic species to oxidize into CO_2 and CO, but oxygen functional groups and oxidized plasma polymers can be formed in this way [Artemenko et al., 2012]. Plasma polymers have been used for some time to produce thin film coatings on surfaces to prevent bio-fouling or to increase hydrophobicity [Kochkodan and Sharma, 2012], but they are now also being explored for in flight-coating of nanoparticles [Qin and Coulombe, 2007, Tavares et al., 2008] and *in situ* coating of nanostructured surfaces such as CNTs and carbon nanofibers [Ramos-deValle et al., 2008, Shi et al., 2002, Ye et al., 2011]. Both of these techniques are important for the development of new nanocomposite materials that require stable suspension of nanomaterials in polymer solutions [Hordy et al., 2013].

2.1.4 Excitation, de-Excitation, and Optical Spectroscopy of Glow Discharge Plasmas

Excitation and de-excitation of gas particles have already been mentioned as processes that occur in plasmas. Their role however, is more complex than ionization impact or elastic collisions, because they provide both energized species for plasma chemical reactions and produce characteristic photons. Photon emission by de-excitation of excited species in plasmas provides important information about the relative concentrations of excited species as well as a direct means of measuring the electron temperature of the plasma.

The absorption of photons to excite electrons in atomic and molecular orbitals is exploited in many ways, for example to produce plasmas by laser pumping. Laser excitation is also used for diagnostic purposes to measure the concentration of gaseous species by exciting non-radiative or fluorescent transitions. Raman spectroscopy and

laser induced fluorescence are two important techniques that use laser excitation of atoms. Lasers did not form a part of this thesis, however, so their use will not be discussed further.

The measurement of emission is a key tool for the characterization of plasmas, because it gives information about both plasma temperature and plasma composition. In general, the intensity of emission from a characteristic wavelength of a particular species is proportional to the concentration of that species, N, and is dependent on the electron temperature of the plasma as well as several other physical parameters, the activation energy of the transition, E, the partition function, Z, and the Boltzmann constant, k_B. The mathematical dependence of emission on electron temperature and species concentration is shown in Eq. 2.2.

$$I(T_e) \propto \frac{N(T_e)}{Z(T_e)} exp\left(\frac{-E}{k_B T_e}\right) \tag{2.2}$$

2.2 Carbon Nanotubes: Structure, Synthesis, and Chemistry

Although carbon nanotubes (CNTs) are still a subject of intense research, the topics of CNT synthesis, structure, and properties are sufficiently well understood to be published in reference works. The contents of this section are mostly based on a set of recent books [Dresselhaus et al., 2000, Dresselhaus and Eklund, 2000, Jorio et al., 2008], with some subject matter adapted from peer-reviewed journal articles. This section will specifically discuss the definition and metrology of the macro-molecular structure of CNTs, the resulting thermal and electrical properties of CNTs, CNT synthesis methods and mechanisms, and important applications of CNTs. CNT applications that take advantage of electrical and chemical modification of the CNT surface chemistry will be described in particular detail, as will the production of CNT-polymer composites for

advanced applications.

2.2.1 CNT Structure and Metrology

The description of the macro-molecular structure of CNTs is helped greatly by the accompaniment of numerous diagrams, so this section will present a simultaneous description of CNT structure and the common techniques used to observe and measure them. CNTs are closely related to the other forms of graphitic carbon, in that they are composed of one or more concentric shells of axially symmetric graphene[Hu et al., 1999]. A ball and stick model of the relationship between CNTs and graphene is shown in Fig 2.3. In the figure it can be seen that both graphene and CNTs, in the ideal case at least, consist of repeating hexagonal units of sp^2 hybridized carbon atoms arranged in a two-dimensional lattice. The importance of this structure cannot be exaggerated, as it is the source of many of the unique thermal, electronic, and chemical properties of CNTs that will be discussed in this section. Each lattice is anisotropic, and is described by a chirality vector that also indicates its electrical conductivity. The chirality vector expresses the angle between the axis of the CNT and what is defined as the major axis of the lattice shell. This is shown for an ideal graphitic sheet in Fig. 2.3, C [Odom et al., 2002]. The chiral vector is defined by an ordered pair of coordinates, (n,m), relative to an arbitrary starting point (0,0). It is denoted by the symbol C_h, and defined such that it is perpendicular to the z-axis when the graphitic sheet is superimposed on a cylindrical geometry. The values of n and m each correspond to an integer number of carbon atoms between the two ends of the vector in the x and y directions, respectively.

The axial electrical conductivity of a CNT depends on the chirality of its constituent concentric shells. In terms of axial conductivity, CNTs are classified as either non-conducting, semi-conducting, or conducting, depending on the magnitude of the characteristic chiral vector. A chiral vector of (n,n) indicates that the major axis of the

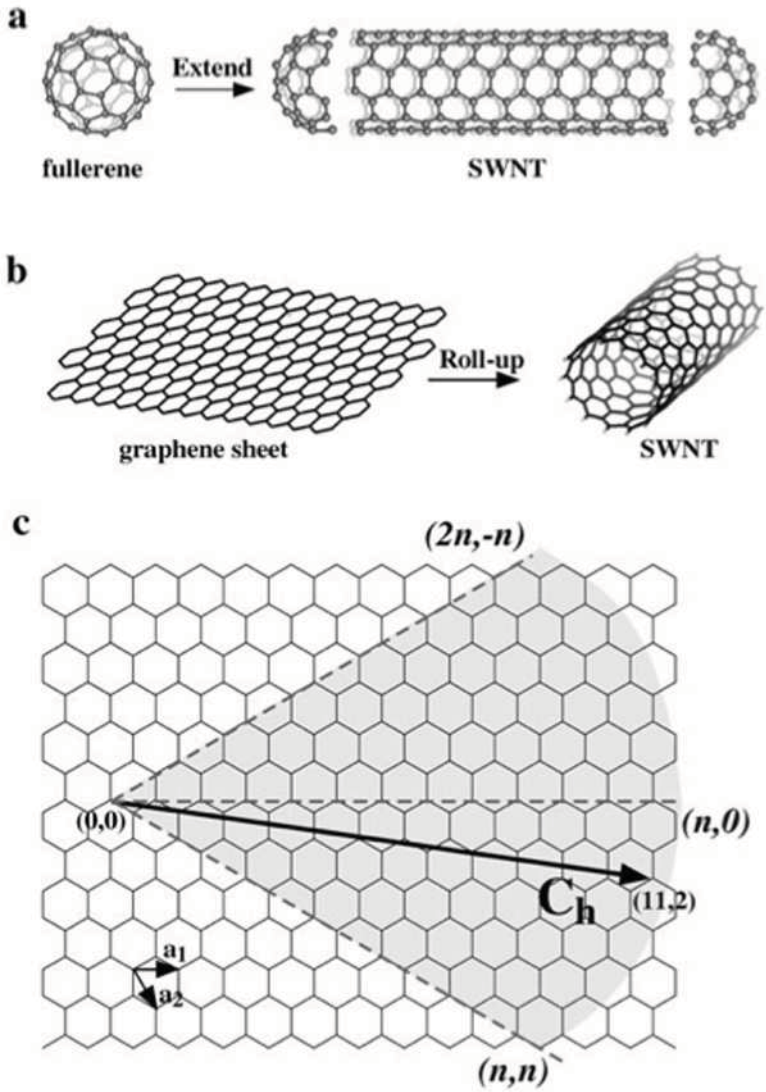

Figure 2.3: The three low-dimensional allotropes of graphitic carbon: **A:** "Zero-dimensional" C_{60} **B:** "One-dimensional" Single-wall carbon nanotube **C:** The chiral vector defined visually for a graphitic lattice [Odom et al., 2002]

graphene lattice is normal to the CNT axis. This corresponds to a CNT that is non-conducting. At the other extreme is the chiral vector that indicates the two axes are coincident, or (n,0), meaning that electrons will travel with little resistance along the axis of that particular shell. These two cases are given the names "arm–chair" and "zig–zag", corresponding to their resemblance to the geometric-isomers of cyclohexane. In between these two end-cases the alignment is non-ideal for conductivity, and the CNT shell will be semi-conducting. This is of course a simplified explanation, since the actual conductivity depends on the diameter of the CNT, the number of concentric shells, and the molecular ideality of the graphene lattice. An important point to make with regard to the number of concentric shells, however, is that CNTs with multiple concentric shells are almost always conductive. This is due to the combined effect of inter-shell coupling of molecular orbitals and the likelihood that at least one shell will be conductive.

The measurement and direct observation of lattice shells of CNTs is most often done by transmission electron microscopy (TEM) and scanning-tunnelling microscopy (STM). Scanning electron microscopy (SEM), while being a useful technique for observing CNTs at high magnification, does not reveal the atomic scale detail that is useful for characterization of the molecular structure of CNTs. Since these techniques were not used widely during the course of this thesis, description will focus on the results of TEM and STM imaging, which will be used to help illustrate the structure of CNTs. TEM uses a collimated beam of electrons that passes through a sample to form a shadow image on a phosphor screen or charge-coupled device. The resolution of this technique readily allows for the visualization of diffraction patterns formed by the concentric walls of CNTs, and in some cases has even succeeded in imaging the hexagonal lattice of CNTs with only one shell, called single wall carbon nanotubes (SWNTS)[Rodriguez-Manzo and Banhart, 2009]. This is shown in Fig. 2.5.

STM uses measurements of electron-tunnelling to produce images of the inner or-

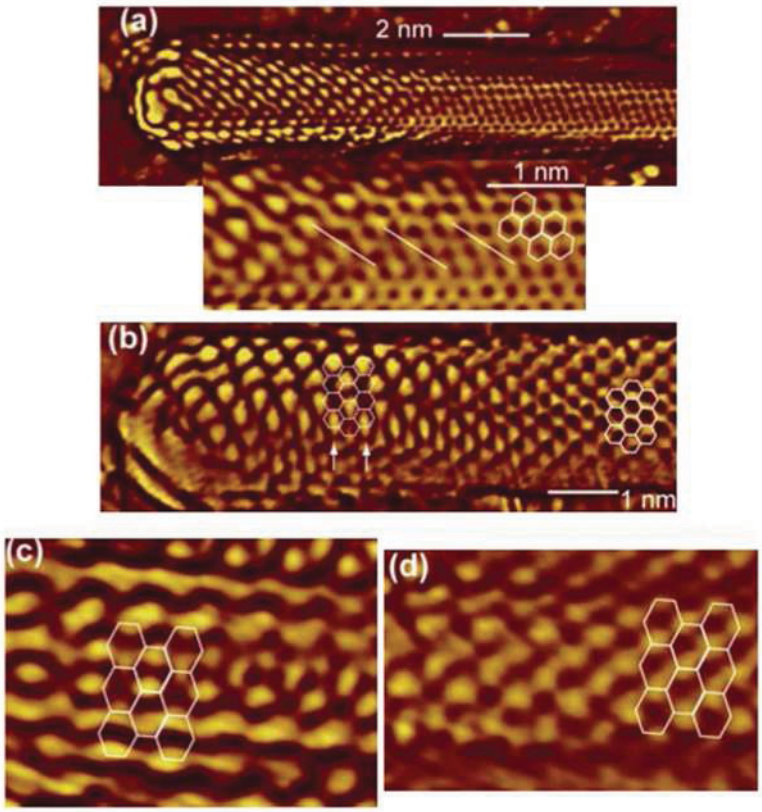

Figure 2.4: STM images **(a-d)** of CNTs measured near the end-caps, showing axial variation in lattice chirality caused by tube closure. [Furuhashi and Komeda, 2008]

bitals surrounding the carbon atoms in a CNT lattice[Odom et al., 2002]. Measurement involves the placement of a probe tip within close proximity to a CNT surface and measuring the electron current that is produced at a given voltage. The electron-tunnelling current that is induced by a set probe voltage is proportional to the electric field barrier at the tip, which is itself dependent on the presence of atomic nuclei. Positively charged atomic nuclei reduce the barrier for electron-tunnelling, thereby increasing the probe current. In this way, a two dimensional map can be produced showing the position of carbon atoms by keeping tight control on the position of the probe and scanning it over a CNT surface. STM imaging can reveal detailed changes in CNT lattice chiralities, such as those that occur around defects or proximal to CNT end-caps. The results of this approach are shown in Fig. 2.4 [Furuhashi and Komeda, 2008].

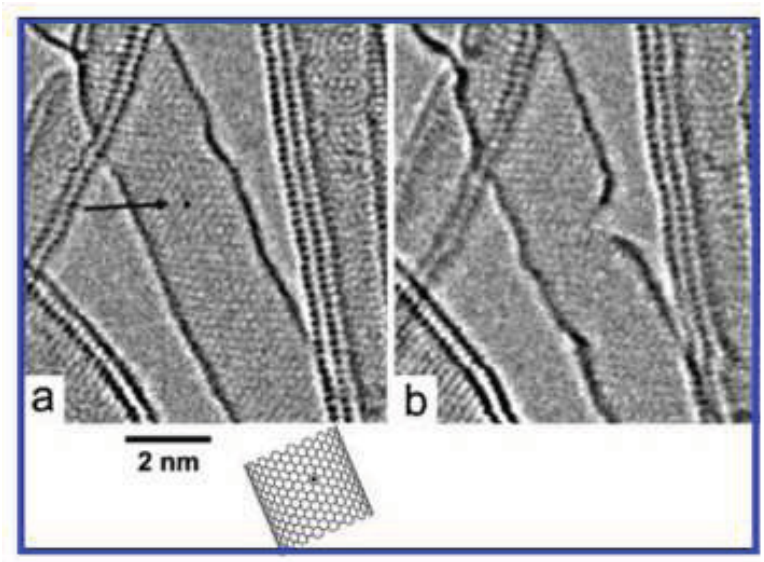

Figure 2.5: Scanning TEM images of an (18,18) armchair single- wall carbon nanotube before (a) and after 10 s of irradiation (b) with a 1 Åelectron beam spot at room temperature.[Rodriguez-Manzo and Banhart, 2009]

In addition to direct imaging of CNT structure, spectroscopic techniques help to

describe the electronic and chemical properties of CNTs. Raman spectroscopy is a laser fluorescent approach that detects the various resonant modes of CNT molecular orbitals. The principle involves the previously described concept of radiative transitions elicited by photon absorption. Specifically, a laser probe is absorbed by a CNT sample and the resulting de-excitation emission is detected by a monochromating spectrometer. This technique is important to describe the difference between conducting and non-conducting CNTs in terms of molecular orbital structure. In CNTs with multiple concentric shells, called multi-walled carbon nanotubes (MWNTs), as well as in SWNTs, the radial breathing modes are detected along with a pair of peaks labeled by convention the D and G bands [Zhao et al., 2002]. This is shown in Fig. 2.6, which also shows the difference between conducting and non-conducting SWNTs. For a typical Raman spectrum taken from MWNTs, refer to Fig. 5.2. The radial breathing modes are inversely proportional to the CNT diameter, which allows for an estimate of CNT size in SWNTs or of the presence of many internal shells in MWNTs. The axial conductivity of the CNT affects the resonance between the CNT electron structure and the incident laser beam. This axial resonance affects the intensity of the G band peak, so it is sensitive to the number of concentric shells in MWNTs. The intensity of the D band peak is proportional to the amount of disorder (also known as defects) in a CNT lattice, so it is often used to to assess the ideality of the CNT lattice. Both peaks are also proportional to the quantity of MWNTs present in a sample. Raman spectroscopy is rarely used to quantify MWNTs, however, since spectra are sensitive to many other factors.

Lattice ideality is an important topic of research for both fundamental investigations and for the development of applications, alike. The presence of defects in the regular repeating structure of the graphene lattice interrupts the electron conductivity of CNT shells, as has been previously mentioned. Lattice defects also affect the chemical reactivity of CNTs by introducing points of high lattice strain [Liu et al., 2013].

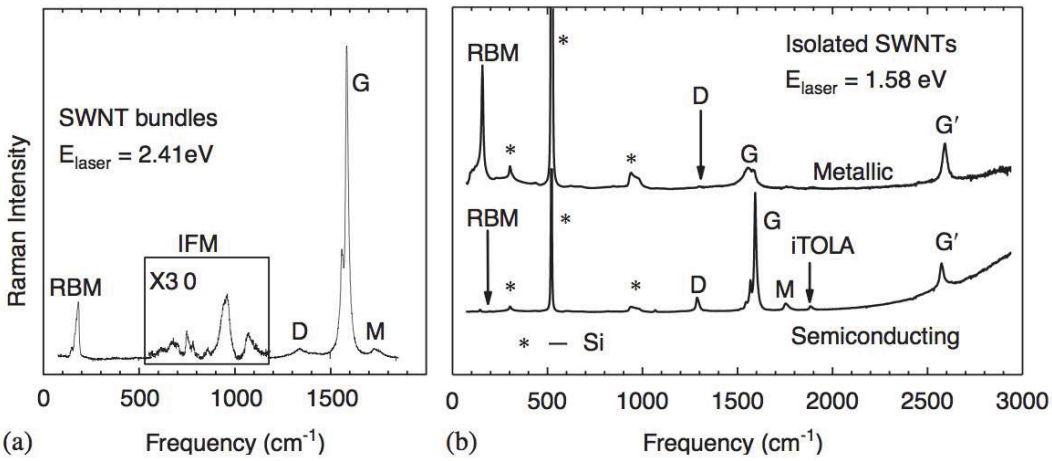

Figure 2.6: **A:** Raman spectrum from SWNT bundles. **B:** Raman spectra from a metallic (top) and a semiconducting (bottom) SWNT [Dresselhaus et al., 2005].

Lattice defects can be detrimental to applications that target transport properties, such as in field-effect electron sources [Minoux et al., 2005]. Thermal annealing is a common approach to approach to ameliorate these defects, and is used as a pretreatment for field-emitter devices. In many cases where covalent functionalization is part of the CNT application, however, defects are necessary as sites of nanoparticle nucleation or chemical reactivity, for example [Felten et al., 2005, 2007]. CNT reactivity will be addressed in more detail in a subsequent section.

2.2.2 CNT Synthesis

An unavoidable aspect of all CNT synthesis techniques is that CNTs are self-assembling nanostructures that form as a thermodynamically preferred product of carbon precipitation. Some level of control over the morphology, structure, and size of CNTs has been achieved by careful experimental development of many different synthesis methods, but large scale synthesis, length control and chirality selection are still issues being

addressed. The work presented in this thesis used only thermal-chemical vapour deposition (t-CVD) to synthesize CNTs and that process will be discussed in detail in the chapter 3. This section will summarize the various methods of CNT synthesis, and explain the underlying principles of CNT growth and chemical vapour deposition in more detail.

CNT Synthesis Methods

The first report of CNTs was made from soot samples that had been collected downstream of a graphite arc discharge [Iijima, 1991]. The high temperatures and vaporization of graphite fragments led to the thermodynamic nucleation of soot particles, which included some CNTs. DC arc discharge technology has become the current method of choice for large scale production of bulk CNT powders [Joselevich et al., 2008]. A transition metal-doped graphite electrode is evaporated using a DC arc in an inert plasma, and the iron nanoparticles that form downstream of the plasma act as nucleation sites for the formation, termed ”growth”, of CNTs [Shi et al., 1999]. CNT growth occurs in the gas phase and sample collection can be achieved easily by electrostatic precipitation [Joselevich et al., 2008]. Work on improving sample collection has led to the development of CNT length-sorting techniques, whereby CNTs are collected in bins on a biased surface [Joselevich et al., 2008]. The separation is based on surface charging during exposure to the electrons in the DC plasma, or by exposure to a secondary corona discharge that further charges the CNT surfaces.

The use of iron nanoparticles for CNT growth is a standard procedure, and has been somewhat inaccurately called catalysis. In reality, the effect of iron in the synthesis of CNTs lies in the size confinement of carbon precipitation by nano-sized iron particles and in the temperature dependence of carbon solubility in iron. Studies on the role of iron catalysts in CNT growth have shown that the diameter of the catalyst particles has

a direct effect on the average diameter of the CNTs that are produced [Joselevich et al., 2008]. Specifically, the diameter of catalyst particles confines the maximum diameter of CNTs that can form. Fig. 2.7 illustrates this concept by showing the growth of MWNTs from iron nanoparticles [Rodriguez-Manzo et al., 2007]. Conversely, iron microparticles and continuous iron surfaces are used in synthesis of other carbon forms [Hirsch, 2010], showing that without nanoscale confinement carbon precipitation does not lead to CNT growth.

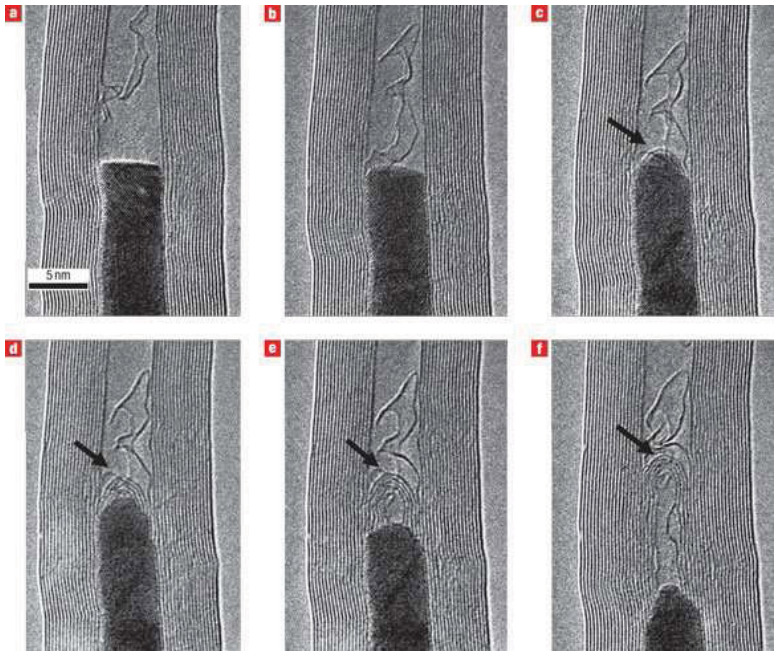

Figure 2.7: TEM images of MWNT growth from an iron catalyst particle. Taken *in situ* during CNT growth experiment [Rodriguez-Manzo et al., 2007].

The thermodynamic stabilization of iron-carbon solutions by phase change limits the precipitation of carbon during cooling, and can inhibit CNT growth. CNT growth further depends on phase change kinetics, since both temperature and carbon content affect the phase structure of iron. Nano-sized iron particles serve an added purpose

in this regard, by trapping the iron atoms in a particular phase [Schaper et al., 2004]. The energy requirement of rearranging the atoms in nanoparticles is too high for phase change in many cases, owing to high surface to volume ratio and the resulting high surface energy.

Carbon atoms that are present in the gas phase in most CNT synthesis techniques are absorbed into iron catalyst particles while at elevated synthesis temperatures. The solubility of carbon in iron decreases during the subsequent cooling of the reactants and causes the precipitation of carbon out of the iron matrix. The carbon atoms migrate through the iron crystal lattice to the surface of the catalyst particle to form either graphitic or amorphous carbon. The formation of graphitic carbon is necessarily a slower process than amorphous carbon formation, since it involves the ordering of individual atoms into a macromolecule. Amorphous carbon, on the other hand, is a disordered precipitate that is composed of agglomerations of small carbon molecules. Graphitic carbon is the preferred product when carbon precipitation occurs on roughly the same time scale as the formation of the graphitic molecules [Schaper et al., 2004, Rodriguez-Manzo et al., 2007]. The temperature and heating rates must therefore be carefully controlled to ensure the necessary conditions for graphitic carbon synthesis [Meunier et al., 2012]. This introduces added complexity to CNT synthesis, by coupling the temperature dependency of carbon solubility to the phase change kinetics of carbon-iron solutions.

Various other techniques are also used to produce similar conditions to those found in DC arc discharge synthesis. The two main approaches are laser ablation of transition metal-doped graphite [Guo et al., 1995], and chemical vapour deposition. In the former a high fluence laser is used to vaporize a graphite target, and the resulting iron-rich carbon plasma provides the conditions required for CNT growth. Chemical vapour deposition (CVD), on the other hand, does not allow for gas phase CNT growth. CVD

exploits catalytic surface sites to precipitate CNTs. The method uses thermally decomposed carbon gases that have been absorbed into a heated catalyst layer.

Chemical Vapor Depostion

CVD synthesis requires the preparation of a nanostructured iron surface, since synthesis occurs on a substrate rather than in the gas phase. Iron catalyst nanoparticles are produced either by thin-film methods [Fan et al., 1999] or by surface modification of bulk iron samples [Baddour et al., 2009]. In the former, the typical approach uses a thin film of iron that is coated onto a semiconducting substrate, such as silicon [Nyamori et al., 2008, Fan et al., 1999]. The film is thermally annealed to form nano-scale iron islands to act as catalyst particles [Li et al., 2001, Cheung et al., 2002]. This technique allows for tight control of catalyst particle size, as shown in Fig. 2.8[Cheung et al., 2002], and also can be combined with nano-lithography or masking to produce specific geometries for CNT deposits [Fan et al., 1999]. By controlling catalyst particle size, CVD methods also afford tight control on CNT diameter, and typically produce CNTs with a high degree of geometric uniformity.

CNT growth depends the absorption of carbon into the iron catalyst particles. Saturated hydrocarbons like methane are used [Kong et al., 1998], as are unsaturated hydrocarbons like acetylene [Ren et al., 1998]. At the temperatures of synthesis these small molecules decompose into atomic carbon and hydrogen and the carbon present in the gas is drawn into the iron particles by diffusion. For obvious reasons, CVD must be carried out in an inert atmosphere, since oxygen or other reactive species will consume the atomic carbon in competing synthesis reactions. Nitrogen gas and argon are common carrier gases for CVD. N_2 can take part in CNT synthesis when temperatures exceed the threshold for N_2 decomposition, as occurs in flame or arc discharge methods [Ayala et al., 2010]. The synthesis of CNTs by CVD is illustrated in Fig 2.9.

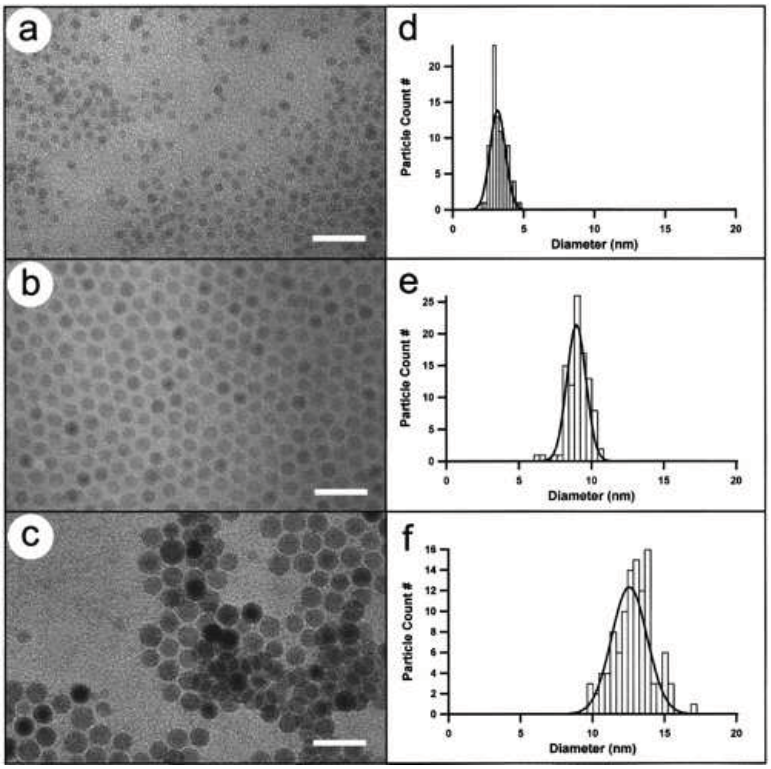

Figure 2.8: TEM images of iron nanoparticle catalysts and corresponding particle diameter distribution histograms [Cheung et al., 2002]

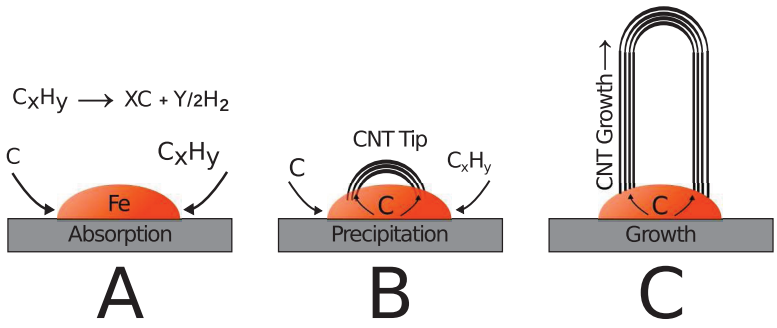

Figure 2.9: Diagram showing the simplified process of thermal CVD growth of MWNTs by the "root mechanism". **A:** The initial decomposition of the hydrocarbon precursor gas and the dissolution of carbon into the iron catalyst particle; **B:** The beginning of the precipitation phase when the iron nanoparticle is saturated; **C:** The growth phase, during which the MWNT grows out from the sample surface.

After the initial carbon injection stage, the CVD procedure offers a great deal of control over the rate of precipitation by heating the sample externally. Unlike in DC or ICP plasma torch and laser ablation techniques, the heat for carbon absorption in CVD can be provided by a furnace that is capable of controlled temperature changes. By adjusting the temperature in a controlled way, the issues arising from uncontrolled carbon precipitation can be avoided. It has been shown that significant reproducibility and uniformity of CNT samples is possible with CVD. Details of the CVD procedure adopted for this work, including temperatures used and timing schedules, are given in chapter 3, and will be omitted here.

The CVD method used in this thesis follows the previously described approach, with the unique difference that the synthesis substrate is not decorated with iron nanoparticles, but rather is prepared from a native stainless steel surface. Although the mechanism is not fully understood, the procedure involves heating a stainless steel substrate in the presence of trace amounts of oxygen. This has been shown in literature to produce

nanoscale iron surface features during a process called sensitization [Chung and Chung, 2003, Cho et al., 2000]. The chromium migration that occurs during sensitization serves as a hypothetical basis for understanding the success of this technique.

2.2.3 CNT Surface Modification

Their graphitic structure makes CNTs suitable for covalent chemical modification. Modification can be affected by reactive addition of many different types of atoms and molecules, but the basic principles of chemical modification are best demonstrated by exploring oxygen and nitrogen addition. The graphene lattice of CNTs can be oxidized, or doped, in many different ways, as shown in Fig. 2.10. A high degree of oxidation can occur before the integrity of the CNT lattice structure is compromised [Collins et al., 2001].The addition of oxygen is a first step in the process of more complex modifications of CNTs, aside from being useful in itself. For example, oxidation of graphitic carbon has been explored as a means of introducing a controllable band gap into CNT surfaces for photoluminescence [Jhi et al., 2000] and carbonyl and carboxyl functional groups can be targeted for conjugation with other organic molecules, including polymers [Hu et al., 2004, Peng et al., 2003, Nishino et al., 2002, Lamberti et al., 2013].

The two main methods of CNT surface modification differ in the use of liquid suspension for chemical reaction. Wet methods, which require suspension of CNTs in the reaction medium, have been thoroughly developed and can produce impressive functionalization results. These include both covalent functionalization, such as oxidation, and coating procedures[Tasis et al., 2006]. For example, polypyrrole and polyaniline coatings have been produced on suspended CNTs with very tight control of film thickness [Yu et al., 2005, Ginic-Markovic et al., 2006]. Typically, a commercially prepared CNT powder is suspended in a liquid by simple sonication. The reaction proceeds either until the CNTs agglomerate and settle or the reaction is terminated by removing

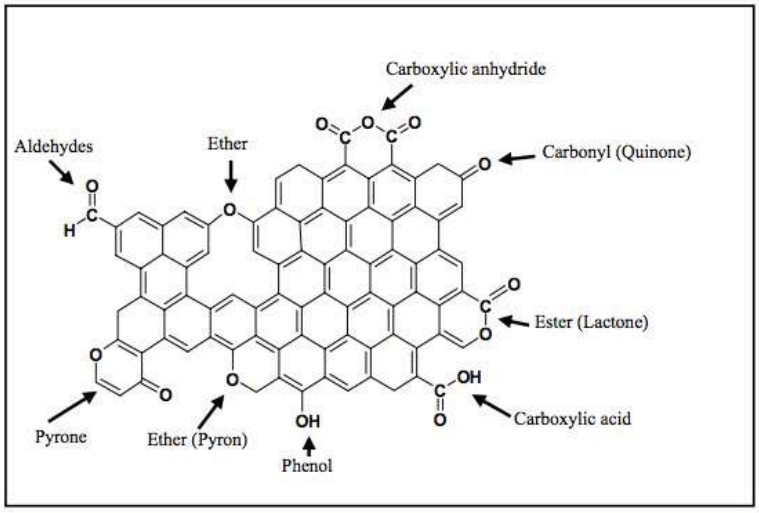

Figure 2.10: Illustration of possible oxygen functionalities that can be introduced into CNT shells by reactive addition.

the CNTs through medium exchange or filtration. Difficulties abound in this approach, however, owing to poor suspension stability, low purity and reactivity of CNT reactants, requirements for medium exchange, and broad distributions in reaction extent caused by non-uniform suspension of commercial CNT powders. Some of these issues have been addressed in experimental work, such as CNT feedstock purity, but most arise from physical limitations to suspension of CNTs in liquids, which is in itself a flourishing topic of functionalization research.

Dry functionalization, which does not require suspension in liquid media, is accomplished *in situ* by several methods. The first is thermal treatment in a reactive gas. This can be used to add halogen functionalities, oxygen, or amine groups[Hirsch and Vostrowsky, 2005]. CNTs can be annealed by heat treatment as well[Andrews et al., 2001], which is a non-reactive form of surface modification to remove lattice defects. The most effective dry method, however, is plasma-induced surface functionalization.

The energized species that are produced in a plasma greatly increase the effectiveness of surface modification reactions, and offer the added possibility of producing uniform coatings of plasma polymers. A short list of the types of surface modifications that have been achieved by plasma treatment is given in Table 2.2.

The mechanisms of plasma functionalization are not well understood, forming a large part of the impetus of this project. That being said, the development of experimental work on the subject has been rapid. Within the preceding decade, work has progressed from initial reports of plasma hyrophilization [Vohrer et al., 2007] to detailed analyses of the impact of many plasma parameters, such as gas composition, plasma power, and treatment time, on the surface chemistry of CNTs [Felten et al., 2005]. It has been decided that the overall effect of plasma functionalization is that active plasma species react with the sidewalls of CNTs in a random manner. The surface energy of carbon atoms helps to determine the preferred sites for reactive addition by focusing the reactions at high-energy sites such as defects and points of high curvature [Chen et al., 1998]. Theoretical studies confirm that curvature and lattice strain play a major role in plasma functionalization [Guo et al., 2010b]. The mechanism responsible for surface localization is a multi-step process. It begins with adsorption of atoms from the plasma on CNT surfaces and is followed by migration of the adsorbed atom, or adatom, into an energetically favourable position on the surface. The final step in the process is a reaction of the adatom with the carbon structure to form a new surface functional group.

Computational chemistry investigations have revealed important information regarding the adsorption of oxygen atoms onto CNTs, providing a further motivation for the theoretical component of this project. It was found that the chirality of a CNT affects the orientation of oxygen functional groups on the surface [Liu et al., 2013], and that oxygen ad-atoms tend to migrate into positions most closely aligned with the basis vector of the CNT lattice, and align with the CNT axis in metallic CNTs [Guo et al., 2010a]. Rel-

Table 2.2: CNT Surface Modification by Plasma Treatment

Functionalization	**Plasma Type**	**Application**	**References**
Covalent Oxidation	Surface Wave Microwave Discharge	Hydrophilization	[Chen et al., 2009]
Oxidation-Amination	Dielectric Barrier Discharge	Hydrophilization	[Naseh et al., 2010]
Amination	Surface Wave Microwave	Hydrophilization	[Chen et al., 2010]
Polymer Coating w/ Acrylic Acid	Radio Frequency Glow Discharge	Ploymer-CNT Composites	[Neira-Velázquez et al., 2013]
Defect Study H_2/O_2	Radio Frequency	CNT Synthesis	[Nozaki et al., 2012]
Polymer Grafting	Corona in Air 1 atm	Epoxy Nanocomposites	[Xu et al., 2010]
Oxidation-Hydrogenation	Radio Frequency	Ploymer-CNT Composites	[Gilman et al., 2012]
$O_2/N_2/H_2/CH_4$ Functionalization	Radio Frequency	Analytical Study	[Zschoerper et al., 2009]

atively few theoretical studies have been reported on plasma functionalization of CNTs, but many have been published within the last five years on oxygen atom mobility on graphitic materials. These are summarized in Table 2.3, and all show similar effects of surface energy and lattice strain.

Surface reactions between adatoms and CNTs have also been described, showing that oxygen atoms tend to form double bonds with carbon atoms in the CNT lattice. This causes local disruption of the continuity of the CNT lattice by reassigning valence electrons from planar C-C single bonds to the C-O double bond. Models have shown that this reaction can be exploited for the ordered unzipping of CNTs into graphene nano-ribbons [Wang et al., 2011b], which are a desirable starting material for organic micro-electronics [Kosynkin et al., 2009].

2.2.4 Applications of CNTs in New Technologies

Graphitic carbon is now being explored as a solution for many of today's most pressing technological challenges by exploiting its many morphologies, unique transport properties, and chemical functionalization potential. CNTs, as well as graphene, graphene flakes, and carbon nanofibers, are being incorporated into technology aimed at nanoscale heat transfer, micro-electronics, sensors, and energy technologies[De Volder et al., 2013].

Applications Making Use of Thermal and Electronic Properties

The arrangement of carbon atoms in a repeating lattice in CNTs leads to anisotropic conductivity properties. Electronic conductivity has already been discussed, but what has not yet been mentioned is that the CNT axis also acts as a preferred direction for heat transport by lattice vibrations, which are called phonons. Phonon propagation is confined to the axial direction due to the radial symmetry of CNTs, depending on CNT diameter and whether the CNT has numerous concentric shells. The near-two dimen-

Table 2.3: Theoretical studies of CNT Surface Modification

Functionalization	**System**	**References**
Oxygen Mobility	Graphene Grain Boundaries	[Wang et al., 2013]
Oxygen Migration	Graphene Lattice	[Radovic et al., 2011a]
Oxygen Migration Thermochemistry	Graphene Lattice	[Radovic et al., 2011b]
Unzipping CNTs by Oxidation	CNTs	[Li et al., 2012]
Oxygen Mobility w/ Electric Fields	CNTs	[Chen et al., 2013]
Unzipping CNTs - Metal Catalyzed	CNTs	[Wang et al., 2011b]
Strain Induced Unzipping	Graphene	[Ma et al., 2012]
Functionalization Review	Graphene	[Tang et al., 2013]
O_2 Chemisorption	CNTs vs. Graphene	[Silva-Tapia et al., 2012]

sional confinement of atomic vibration within the lattice of a SWNT is the atomic scale mechanism behind the phonon propagation phenomenon. In MWNTs the added effect of inter-shell interaction and radial heat transport reduces the impact of the anisotropy in heat conduction. In SWNTs the presence of lattice defects inhibits phonon propagation[Dresselhaus and Eklund, 2000], causing applications based on thermal effects to be dependent on the purity of CNT feedstocks.

Thermal transport in CNTs has been targeted for use in applications that seek to improve both heat removal and heat storage. Devices such as microscale heat sinks have been developed with bundles of SWNTs acting as cooling fins[Kordas et al., 2007]. CNTs have been incorporated as nanoscale heat pipes for combined electron-heat transport in micro-electronic devices[Green and Hersam, 2011, Rotkin et al., 2009]. SWNT and MWNT colloidal suspensions were initially found to have anomalously enhanced thermal transport properties, but recent work has done much to attribute these findings to inaccuracies in measurement and improper interpretation[Veilleux and Coulombe, 2010]. At the time of writing this thesis, work on applications of CNT thermal transport is focussing on solar thermal harvesting and storage, such as advanced CNT nanofluid suspensions for solar energy collection[Taylor et al., 2013].

Electron conductivity of CNTs is a more reliable property and, combined with thermal and tensile properties, numerous new applications have been developed to improve current technologies. Microelectronic devices have been developed using CNTs as both nanoscale wires[Yu et al., 2011] and as circuit elements, such as field effect transistors[Green and Hersam, 2011] and y-junction switches[Bandaru, 2012]. CNTs are particularly well suited for use as micro-circuit interconnects, which are used to connect different circuit components and as interfaces to larger scale metal contacts[Kreupl et al., 2002]. These applications take advantage of the small diameters of CNTs, since metal wires lose conductivity at the nano-scale [Kitaura et al., 2009]. Microelectronic

circuits and switches have been produced using CNTs as interconnects even in high power applications[Dahmardeh et al., 2013], owing to their high thermal stability. The tensile strength of CNTs has allowed for the development of flexible plastic electronics using CNTs as wire paths[Park et al., 2013]. CNTs are deposited as cross-linked films in many of these applications, rather than being used as wires individually.

Applications Making Use of Surface Chemical Modification: Sensing and Energy

Chemical functionalization and surface modification of CNTs make them an ideal material for applications in biological and chemical sensing and in energy storage and conversion. CNT materials can be produced with high surface area and with specific surface functional groups, including conjugated bio-chemicals such as proteins [Peng and Wong, 2009, Zhao and Stoddart, 2009, Liu et al., 2009]. When attached to a conductive surface, the conductivity of functionalized or otherwise modified CNTs will respond to small changes in surface interactions. Chemical sensors based on CNTs operate by measuring the change in one of these properties as an indirect measurement of the presence and concentration of a species of interest. Furthermore, in sensors that incorporate CNT-forest structures[Bsoul et al., 2011] or webs[Musameh et al., 2011], the high surface area helps to improve sensor response. Since this project is concerned with the chemical functionalization of CNT forest-covered metal substrates, a list of references reporting CNT-based sensor applications, including the type of modification used, has been presented in Table 2.4.

The high surface area and a broad range of possible surface modifications also make CNTs ideally suited for use as nanostructured supports for energy conversion and storage technologies. The typical approach involves preparing the CNTs by modifying them. The type of preparation treatment is specific to the intended application, but in general CNTs are decorated or coated with either metal [Li et al., 2010, Sahoo

Table 2.4: Experimental Reports of CNT Sensor Technologies

Application	**Analyte**	**Reference**
Electrochemical Sensors	Bio-chemicals	[Wang, 2005]
Surface Adsorption Sensor	Gas & Chemical Vapor Sensing	[Li et al., 2003]
Electrochemical Impedance Spec.	DNA & Genes	[Bonanni and del Valle, 2010]
MWNT-Polymer Composite	DNA & Genes	[Xu et al., 2004]
Electroanalytical Sensing	Proteins&Bio-Chemicals	[Lourdes et al., 2008]
Functionalized CNT Electrochem. Sensing	Review	[Wildgoose et al., 2006]
Field-Induction Effect Sensing	Review	[Allen et al., 2007]

et al., 2011] or semiconducting[Meng et al., 2011, Wang et al., 2011a] nanoparticles or organometallic functional groups[Luo et al., 2011]. In some cases, oxygen defects are first introduced by oxidative functionalization. This is done as a means of improving the adhesion strength of polar coatings or to induce a band-gap for semiconductor properties. The decorated CNTs are then incorporated into a composite electrode material, either by deposition of CNT ink suspensions or, in the case of CNTs grown by CVD, attachment of the CVD growth substrate to an electrical contact.

Composite electrodes are used in wet chemical electrolysis cells[McCreery, 2008], wet fuel cells, or in photovoltaic devices made from CNT-semiconductor composites [Liu et al., 2011]. In nickel catalyzed electrolysis of water, for example, CNTs that have been decorated with Ni nanoparticles act as nanostructured catalysts supports that are connected to a metallic anode in an electrochemical circuit [Kalra et al., 2012]. The electrical conductivity of the CNTs allows electrons to travel from the bulk electrode to the nanoparticles on the CNT surface, thereby completing the circuit with the catalyst particles. The main improvements of using CNT nanostructured electrodes are improved catalyst activity by using nanoparticles and increased active surface area relative to bulk materials and to nanostructured nickel surfaces, while CNT reactivity in such systems is still a matter of active research.

CHAPTER 3

EXPERIMENTAL METHODOLOGY

The major part of this thesis describes experimental work on plasma degradation mechanisms of MWNTs, and brief descriptions of experimental methods are included in each chapter represented by a submitted manuscript. That being said, important details relating to the preparation of samples and the experimental procedures used have been described in depth in this chapter in an effort to aid future students and to provide a full record of the work done. Specifically discussed are the design and construction of the plasma chamber, the different chamber configurations used during experiments, and considerations when producing samples, and the analytical techniques employed.

3.1 Experimental Considerations

3.1.1 Plasma Chamber Setup

The experimental setup was designed to be capable of operating in both direct-current and radio-frequency (RF) modes, and thus had a dual-purpose counter electrode that could act as either a grounded relative anode or as a live RF electrode. The setup, as assembled for RF tests, with a cutaway showing the position of the electrodes in the chamber, is shown in Fig. 3.1. Stainless steel meshes with CNT coatings were attached using copper threads to a wire connector and via a vacuum DC feedthrough to an AMETEK XG-600-1.4 DC power supply. This was used to bias the CNT sample for both DC and RF operation modes. The method of preparing the samples with electrical contacts will be described further in the sample preparation section. The chamber was assembled from Quick Flange (KF) parts and was arranged in such a way to form the plasma upstream of the sample position. The direction of gas flow was important, to minimize the

exposure of any species produced by MWNT degradation to plasma chemical reactions.

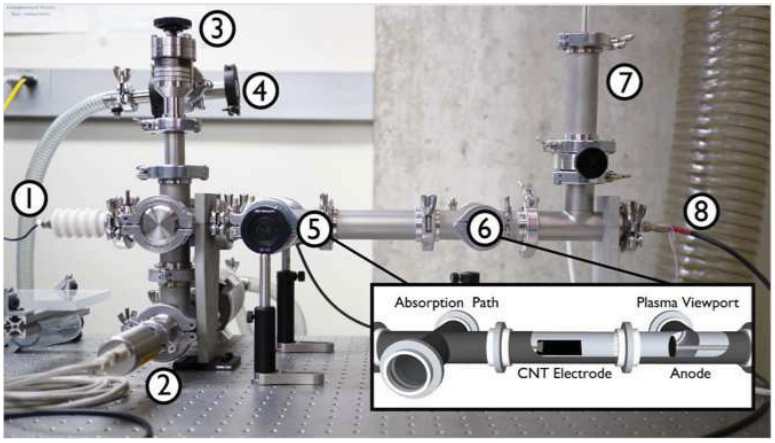

Figure 3.1: Plasma chamber, as assembled for RF afterglow degradation experiments. 1) DC feed-through, 2) Pressure gauge, 3) Vacuum exhaust valve, 4) Cold trap, (5 & 6 as labeled), 7) Gas feed, 8) RF feed-through. **Inset:** Cutaway view of sample/electrode positions

A gas supply system was assembled using compressed gas sources of O_2, N_2, and Ar and a single Edwards 5 sccm mass flow controller. Although the flowmeter was calibrated for nitrogen, the actual flow rate for any gas could be calculated by adjusting the calibration constant. A mixture of gases could be injected by opening multiple compressed gas cylinders simultaneously, but a single gas was used for most experiments. Using a dual stage Alcatel Pascal 2021SD series rotary vane pump and an Adixen MDP 5011 molecular drag pump the chamber base pressure was measured at 6×10^{-6} Torr. For the rotary stage alone the base pressure was approximately 1 mTorr.

Two crosses were placed on either side of the section where the sample would be placed. The downstream cross was equipped with quartz windows on either side, for use in the molecular absorption spectroscopy path, while the upstream cross was equipped with a quartz window only on one side, for emission spectroscopy of the RF discharge

itself. For DC tests, these sections were replaced with a pyrex type 5072 double-ended glass break, for direct visualization of the negative glow regions. The appearance of the sample within the glass section is shown in Fig. 3.2 part A, and with the surface DC discharge ignited in part B.

Spectra were collected using a Princeton Instruments Acton SpectraPro 2300 0.3 m imaging triple grating (300, 600, 1200 BLZ) monochromator spectrograph, a Pixis 256 CCD camera and the Winspec 32 software package. A commercially available 300W tungsten incandescent lamp was used as the source for molecular absorption spectroscopy. The procedure of spectroscopy measurements will be described in detail in the following section.

A small conical reducer was included downstream of the bellows valve, to hold sorptive material. This was used during tests to condense organic vapors using external cooling provided by a reservoir of dry ice. The chamber could also be equipped with a Scientific Systems Smartprobe ALD Unit Langmuir probe for plasma diagnostic measurements, which were done to calculate the plasma potential, ion concentration and the electron temperature. The Langmuir probe data are presented and discussed in Chapter 4.

3.1.2 Experimental Procedure

A set of experimental parameters were held constant for each experiment, regardless of the type of data that was collected. Before beginning evacuation, the chamber was checked for organic deposits from previous experiments. If significant deposits were found, the chamber was disassembled and cleaned. For similar reasons, the oil in the pump was replaced regularly. For each experiment a new MWNT sample electrode was prepared, and was placed into the chamber after being attached to the DC feedthrough. Finally, new compressed carbon pellets were loaded into the condensible vapour col-

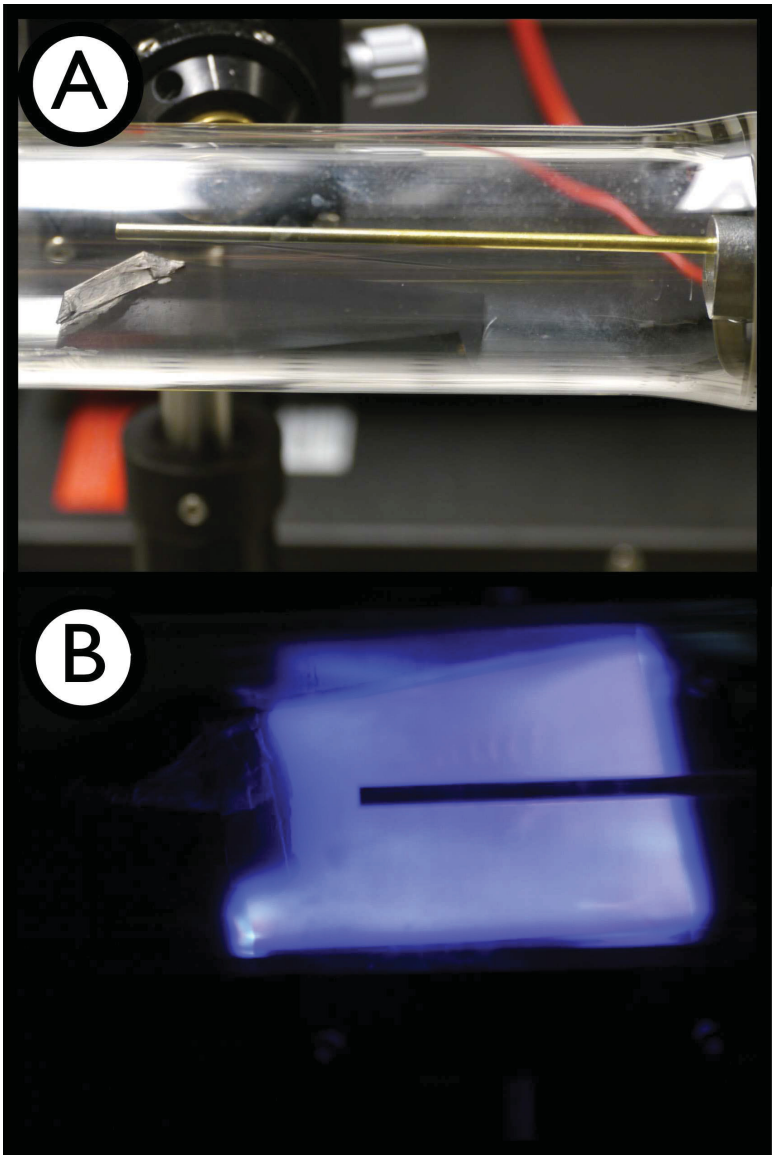

Figure 3.2: Plasma chamber setup for DC glow experiments. **A:**the appearance of the sample in the glass section. **B:** A photograph of the DC glow discharge in operation

lection point, which is described in more detail in the following section on analytical techniques.

After these steps had been completed, the chamber was sealed and the valve to the rotary vane mechanical pump would be opened. The chamber was evacuated to approximately 20 mTorr by the rotary stage, and then the molecular drag pump would be used to bring it to a base pressure of approximately $1x10^{-6}$ torr. After the molecular drag pump was deactivated, the new base pressure for the rotary stage would be approximately 6 mTorr. At this point, the gas supply system would be opened, and 5 sccm of plasma gas would be injected into the chamber for the duration of the experiment. The operating pressure at this flow rate was 0.75 Torr. Special operating conditions were used for DC experiments, but these are described in detail in chapter 4.

The total duration for all experiments was limited to a maximum of 60 minutes. This was found to be the time at which the MWNT layer had been completely degraded, regardless of the plasma composition. At this point, the path of least resistance for electrons in the MWNT sample would be through the now exposed surface of the stainless steel mesh substrate, so it was no longer useful to continue plasma treatment.

To reduce the time required to reach the chamber base pressure in subsequent experiments, the chamber was always re-pressurized by filling it with dry nitrogen. This prevented the adsorption of water vapour and other ambient contaminants onto the chamber walls. Compressed carbon pellets were removed from the collection point immediately after experiments by sealing the exhaust valve between the plasma chamber and the exhaust line, and opening the flange between the two. After removal, the vapour collection point was then reloaded with carbon pellets and the exhaust line was resealed and placed under vacuum.

3.2 Sample Preparation Techniques

The techniques used to produce the samples for this study were developed during several prior projects in the Plasma Processing Laboratory (PPL) at McGill University. The initial development was reported in Carbon, in 2009 [Baddour et al., 2009]. The procedure involves the thermal-chemical vapour deposition synthesis of CNTs using acetylene as a carbon source gas, and stainless steel 304 meshes (100x100 threads per square inch) as the substrate. Stainless steel meshes are degreased and cleaned in acetone, in a sonic bath, for 30 minutes. After drying in a fume hood, the samples are moved to a ceramic boat and placed into a quartz tube that is housed within the furnace. All CVD experiments were done in a Lindberg/Blue HTF 55000 series furnace (120 V / 30 A). Argon is used as an inert carrier gas, as well as a purge gas to remove the oxygen from the system prior to heating the furnace to the required temperature for CNT synthesis. A diagram of the furnace setup is shown in Fig. 3.3. After an initial 10 minute purge of oxygen from the quartz tube, the furnace is heated to 700 ^{o}C, requiring approximately 12 minutes. After a total of 15 minutes, acetylene is introduced to the reaction chamber at a flow rate of approximately 45 sccm for a total of 2.5 minutes. Following the injection of acetylene, the chamber is held at 700 ^{o}C for a further 30 minutes prior to cooling to room temperature.

Samples produced by this method show uniform and dense coverage of the stainless steel surface by an entangled forest of multi-walled carbon nanotubes (MWNTs). Since the MWNTs are grown directly from a conductive substrate, they are in strong electrical contact with it. This property served as the basis for the method of producing MWNT-composite electrode materials.

To connect the CNT meshes to a DC feedthrough, samples were first pierced in three places, using a thin needle. Cleaned and degreased copper threads were passed through

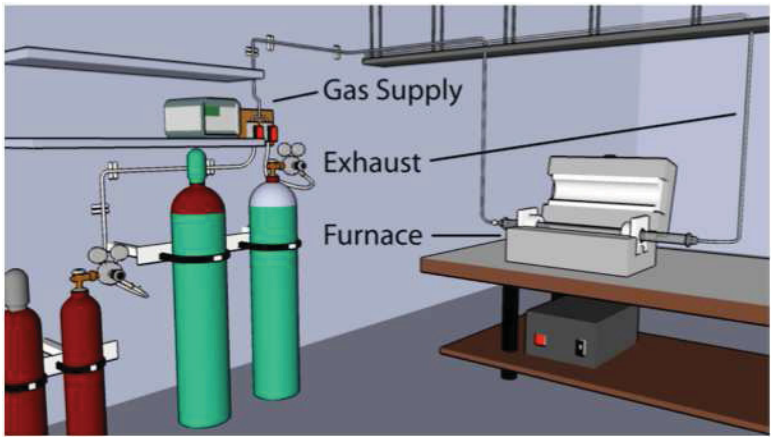

Figure 3.3: Schematic diagram of the CVD setup with important components labeled.

each hole and were wound together to form a braided wire. This wire was then coiled around a solid copper wire that could be fitted by tension to the DC feedthrough, which had been fitted with a copper sleeve around the connection. This process is summarized in Fig. 3.4.

It was found during early tests that the exposed copper wiring would act as a preferred location for the glow discharge to form. Vacuum safe carbon tape and non-conductive carbon paint was added in sequential layers to cover any exposed copper. After drying, the covered area would become much less conductive than the sample. In this way, the MWNT covered sample, and the MWNTs themselves, became the least resistive path for current transfer.

3.3 Analytical Techniques

This section provides a brief description of the analytical techniques used during the study. In general, techniques were chosen for simplicity of implementation while still providing important data regarding the reaction products of MWNT degradation. Considering also the capabilities of the in-house facilities, experimental data collection fo-

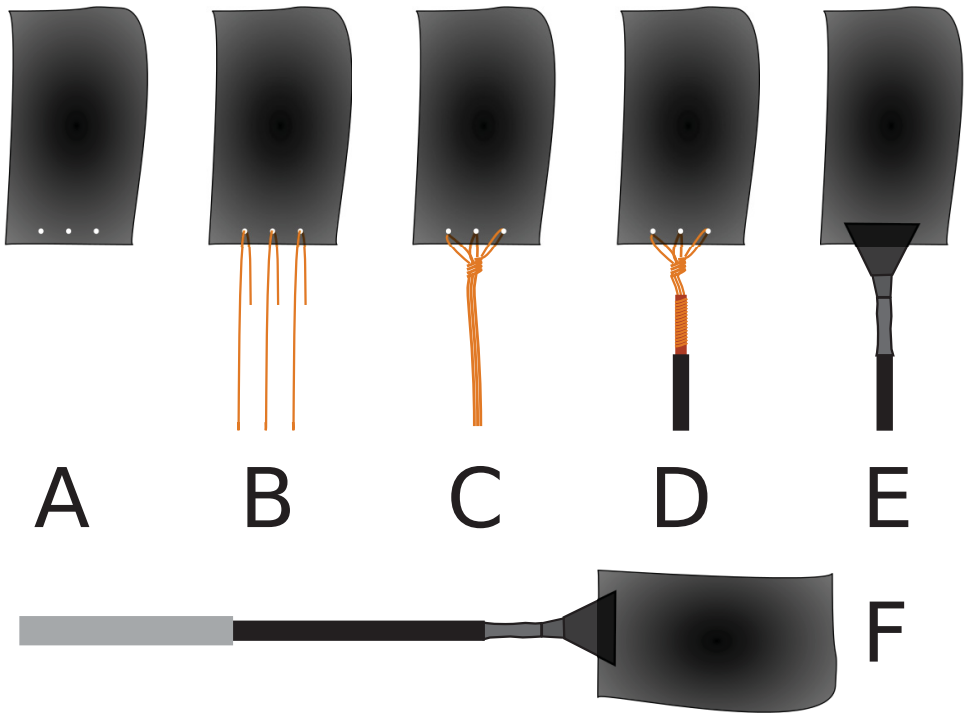

Figure 3.4: MWNT electrode assembly process illustrated: **A:**MWNT-covered mesh sample, **B:** copper threads fitted into the sample, **C:** copper threads wound into a braided wire, **D:** The braided connection after coiling around a copper stem, **E:** exposed copper covered with carbon tape and carbon paint, forming the finished electrode sample, **F:** electrode sample inserted into the sleeve of the DC feedthrough, ready for placement in the vacuum chamber.

cused on spectroscopic techniques that could be accomplished *in situ*, GC-MS data provided by a departmental instrument, and FE-SEM imaging available to the department through the McGill Facility for Electron Microscopy (FEMR) in the Materials Characterization Lab.

3.3.1 Optical Spectroscopy

Spectroscopic Measurements

Both optical emission and molecular absorption spectroscopy techniques were employed during degradation experiments. The same Princeton Instruments monochromating spectrometer was used for both types of measurements by repositioning the optical probe between experiments. The two approaches were intended to measure excited atomic species present in the RF glow discharge and larger molecular constituents of the plasma gas. The molecular absorption beam path was arranged such that it passed through the chamber above the surface of the MWNT covered stainless steel sample. This corresponded to approximately 30 cm along the length of the treatment section. This is shown in part A of Fig. 3.5. The absorption beam path was further placed outside of the glow region, as it was desired to avoid detection of any photons emitted by the plasma in these measurements. This was an important consideration, to prevent changes in emission during the experiment from affecting the absorption spectra. A set of two pinholes restricted the light that reached the optical probe to reduce the impact of unwanted effects, such as scattering and reflections, as well as indirect emission from the plasma.

A tungsten filament incandescent lamp was used as the light-source for absorption measurements. OAS spectra were calculated according to the Beer-Lambert law for gases. This approach was considered appropriate because the concentration of absorb-

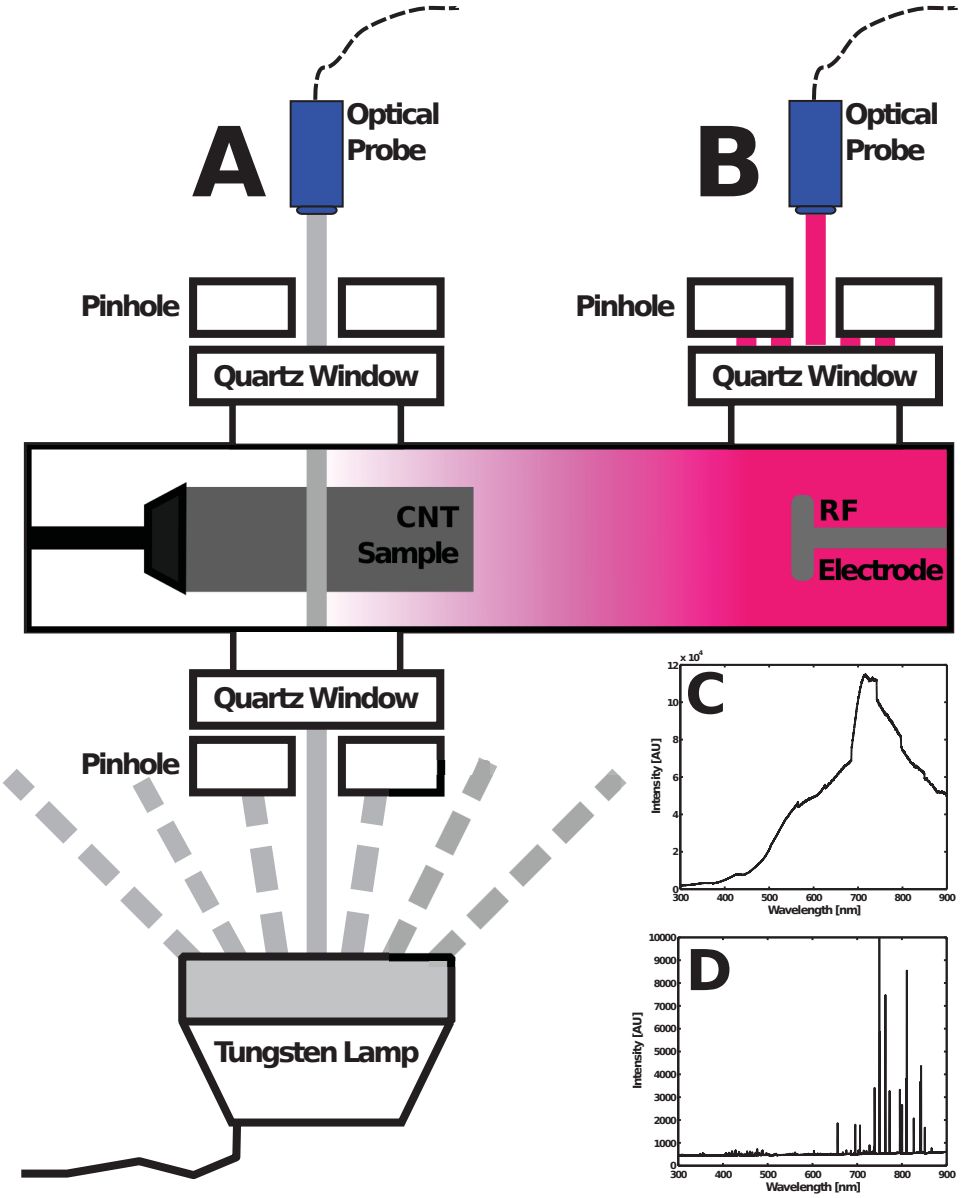

Figure 3.5: Diagram of spectroscopy setup employed during experimental study. **A:** Optical Absorption Spectroscopy (OAS); **B:** Optical Emission Spectroscopy (OES); **C:** Typical output spectrum of incandescent tungsten light source; **D:**Typical OES spectrum for RF glow discharge in Ar during a DC MWNT experiment.

ing species was low, so scattering could be neglected. The light output was not uniform in the wavelength range, as shown in part C of Fig. 3.5, but the non-uniformity did not affect OAS measurements, since the Beer-Lambert law uses a ratio of spectra to calculate absorbance. The equation used for calculating absorbance is:

$$A'(t) = ln\left(\frac{I_o}{I(t)}\right) \tag{3.1}$$

where A' is absorbance, I_o is the reference spectrum and I is the sample spectrum, at time t.

OES measurements, labeled B in Fig. 3.5, were collected directly from the RF glow. The light emitted by the plasma was measured through a quartz window by a Thor Labs BF13 UV-transmitting optical fibre bundle patch-cable. An example of an OES spectrum is shown in part D of Fig. 3.5.

3.3.2 Mass Spectroscopy

GC-MS data proved invaluable when determining the products of MWNT degradation. By sampling the species produced during plasma experiments, the main reactions that occurred during MWNT degradation could be deduced. The collection of gaseous species was difficult in this system, due both to low pressure operation and to the nature of the organic species being collected. In a preliminary approach a mobile MS instrument was connected to the chamber, upstream of the foreline trap, but sampling was unsuccessful under vacuum. It was found that back flow of air was occurring from the instrument into the chamber, so an *in situ* approach was deemed unfeasible.

A technique was developed that comprised a two step process to condense volatile organic vapours under vacuum, then to run GC-MS analysis on a separate instrument. A thermal desorption headspace analysis technique was selected to avoid difficulties with

liquid extraction procedures, as required by liquid chromatography. Initially, silica gel beads were used to adsorb organic vapours in the exhaust stream, but these proved to be unstable during thermal desorption. Strong peaks from silica fragments were detected in test spectra, so it was decided to switch to a thermally stable substrate for organic vapour adsorption.

The final technique, which is summarized in Fig. 3.6, used compressed activated charcoal pellets as the collection medium. Cooling was also implemented, to improve collection efficiency. The design, shown in part A of Fig. 3.6, used a cold finger, cooled externally by dry ice, to lower the temperature of the carbon pellets to -80 ^{o}C. The sample collection stage was adapted from a straight NW25 section in the vacuum chamber that was downstream of the MWNT sample position. Quick Flange NW25 o-rings with mesh screens were placed on each side of the vacuum chamber piece, to hold the pellets in place during re-pressurization. After the conclusion of each experiment the cold pellets were placed in a sealed vial and stored in a freezer prior to GC-MS analysis.

GC-MS measurements were done using a Thermo-Scientific ISQ-LT GC-MS instrument equipped with a headspace analyzer. As mentioned before, headspace analysis uses thermal desorption to separate adsorbed gases from the collection substrate. The procedure developed by Mr. Ranjan Roy specified that samples would be heated to 150 ^{o}C for 30 minutes. This was based on preliminary calculations of the temperature required to desorb species that had adsorbed at -80 ^{o}C. Following the thermal desorption step, the headspace above the carbon pellets was sampled automatically by a 1000 μL syringe, as shown in part B of Fig. 3.6. The gas was then injected into the GC sample inlet, part C in Fig. 3.6, which was kept at a relatively low temperature of 100 ^{o}C. The GC used a non-polar column with He as the carrier gas to separate the various hydrocarbon species, in order to improve the MS analysis. The non-polar column also selectively re-

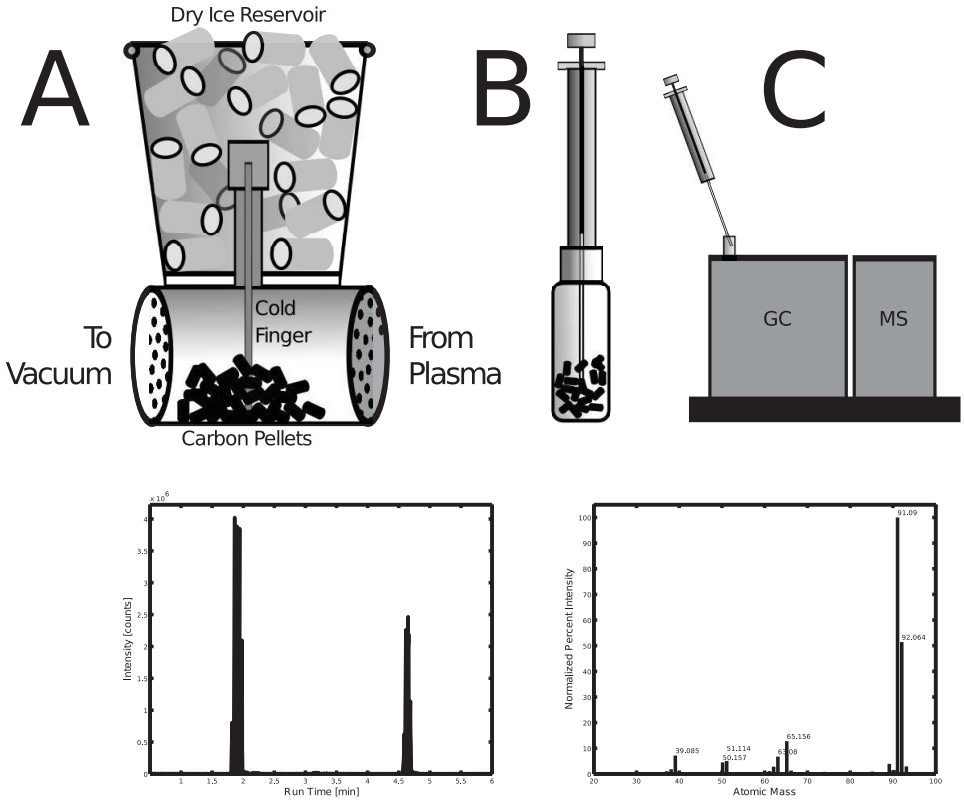

Figure 3.6: Diagram of the GC-MS sample collection and analysis technique. **A:** The collection stage that was implemented into the downstream section of the plasma chamber. **B:** The sampling of the headspace around the pellets after heating. **C:** The injection of the headspace gas into the GC-MS instrument. Also shown are two sample spectra produced by MS analysis. **Left:** a gas chromatogram, and **Right:** a mass-spectrum (*toluene*)

tained non-polar species, such as pump oil that may have back-diffused into the vacuum chamber and contaminated the samples. In preliminary tests of the sample collection procedure, MS spectra did contain signals from pump oil, registering as long alkanes and regularly spaced fragments in intervals of 12 amu. A secondary foreline trap was then installed on the exhaust line of the plasma chamber that was filled with silica gel beads, after which the pump oil was no longer detected.

GC analysis used a thermal ramp from 100 ^{o}C to 350 ^{o}C over a period of 20 minutes. The ramp in temperature was used to further improve separation of the components of the headspace gas, thereby improving the specificity of the MS spectra. Species that eluted from the GC were fed directly to the MS and analyzed. The results of GC-MS analysis were presented as a chromatogram and a mass-spectrum. Examples of these are shown in part D of Fig. 3.6.

3.3.3 Grazing-Angle FTIR Spectroscopy

IR spectroscopy was used for characterization of the surface chemical changes that occurred during plasma treatments. Since MWNT surfaces are not reflective and cannot be measured in an instrument with diamond windows, an approach was developed to use an FTIR microscope in transmission mode for grazing angle measurements. The technique is shown in a diagram in Fig. 3.3.3.

MWNT-covered mesh samples have inner surfaces that are tangential to the path of the IR beam in transmission mode. The IR beam is sent through a sample as shown in part A, and focused on the plane transecting the sample. Grazing angle FTIR measurements can be made of MWNTs in air by focusing the beam at the plane of intersection with the mesh sample, as shown in part B. A typical spectrum obtained by the technique requires careful removal of background information, by using control samples as references. Also, since water vapour and carbon dioxide both absorb IR radiation, the effects

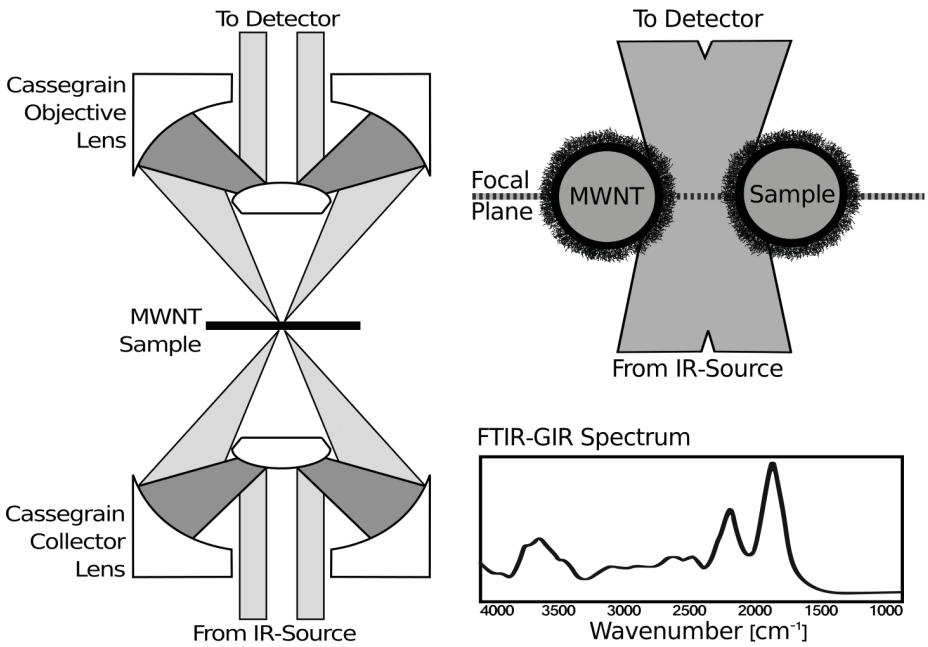

Figure 3.7: Diagram of the transmission mode GIR analysis technique. **A:** The beam path and the Cassegrain lenses that are used to focus the IR beam at the mid-plane of the sample. **B** A magnification of the sample cross-section to illustrate the grazing angle absorption technique. **C:** The FTIR-GIR spectrum that results, after reference and background removal.

of both must also be removed from measurements. The final product of this technique is an FTIR spectrum of the surface groups on the MWNTs, as shown in part C of Fig. 3.3.3.

3.3.4 Raman Spectroscopy

A method was developed to assess the effect of electron bombardment on the chemical structure of MWNTs. Raman spectra were collected at regular intervals on the surface of MWNT-covered samples. The approach was based on the fact that electron bombardment on the surface was non-homogeneous. The intensity of bombardment was inversely proportional to the distance from the RF electrode. For this reason, the greatest degeneration of MWNTs was observed at the edge of the sample nearest the RF glow discharge. The extent of degradation was contained in a "transition region", ranging from complete degradation at the outer edge to minimal damage at the inner edge. This effect was also seen in SEM images (see sections 4.5, 5.4, and 6.4).

Table 3.1: Raman Spectroscopy Parameters

Parameter	**Short Exposure**	**Long Exposure**
Laser Power	50 mW	50 mW
Laser Wavelength	754 nm	754 nm
Spot Size	50 μm^2	50 μm^2
Integration Time	80 sec	120 sec
Coadditions	2	3
Resolution	3.5 cm^{-1}	3.5 cm^{-1}

Starting at the edge that experienced the most severe degradation, Raman spectra

were collected at regular intervals of 0.5 mm and 1 mm on the sample surface. The spacing was measured by a remote controlled motorized sample stage through a built-in optical microscope. The approach is summarized in a diagram given in Fig. 3.3.4. Raman signal intensity is very sensitive to environmental conditions as well as to the laser beam power, fluence, and exposure time. This makes it very important to tightly control the parameters of the instrument during comparative measurement. The effect of the instrument on sample measurement was carefully controlled by keeping the laser settings constant and by using a consistent technique for focussing the laser beam on the sample surface. The settings used are summarized in Table 3.1 The effects of the environment and of non-uniformities in the sample surface were addressed by repeating measurements at various times of day on each sample, and by repeating the measurement procedure on multiple samples. Each sample was measured across a distance of 5 mm, either at 5 or 10 sampling positions, with three spectra measured at evenly spaced lateral-positions for each vertical position. Spectra for use in preparation of figures were measured using the long-exposure parameters, while most spectra were collected using the fast measurement parameters.

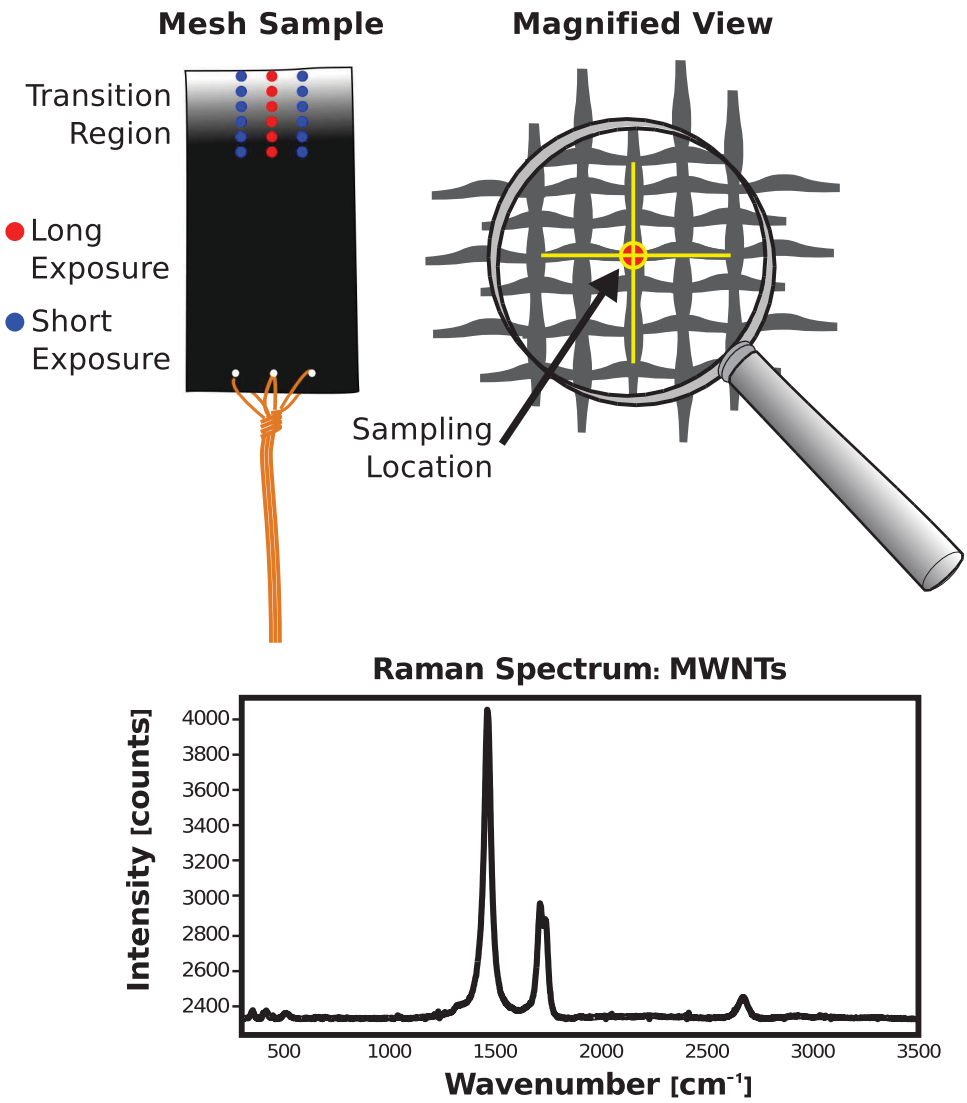

Figure 3.8: Diagram describing Raman measurement method. Sample shown with sampling location, with a magnification of the location on the mesh where laser was focussed. Sample spectrum of MWNTs is given.

CHAPTER 4

ION BOMBARDMENT INDUCED COVALENT FUNCTIONALIZATION

Preface

This chapter presents an article that has been published in the journal *CARBON* [Vandsburger et al., 2013a]. The complete citation of the published article is:

> L. Vandsburger, S. Coulombe, J.L. Meunier, *Degradation of carbon nanotubes in oxygen glow discharges*, **Carbon**, Volume 57, June 2013, Pages 248-258.

The work was planned, executed, and analyzed by L. Vandsburger. Research supervision and reviewing of the manuscript were the shared responsibilities of the two academic advisors, S. Coulombe and J.L. Meunier.

The manuscript describes a comprehensive study of the role of oxygen ion bombardment-induced covalent functionalization of MWNTs. The surface chemical reactions occurring during exposure to plasmas containing oxygen ions are studied through the analysis of MWNT degradation products in both DC and RF afterglow plasmas. Ion bombardment was elicited by imposing a surface bias on MWNT-covered stainless steel meshes, as described in Chapter 3. The article also contains a brief methods section to complement the previously described experimental methods of OAS, OES, and GC-MS. Langmuir probe data from the RF afterglow are presented for the first time in this chapter to confirm the presence of charged particles at the sample position.

Findings show that oxygen ion bombardment is a covalent process that removes oxygen from the plasma in the vicinity of the electrode surface. Furthermore, the specificity of covalent functionalities is determined from GC-MS and OAS measurements. It is found that carboxylic anhydride groups are formed as a final product of oxygen func-

tionalization, even in the presence of hydrogen in the plasma. Carboxylic anhydrides are a common form of oxygen functional group, as shown in Fig. 2.10.

Degradation of Carbon Nanotubes in Oxygen Glow Discharges

L. Vandsburger, S. Coulombe, J.-L. Meunier

Plasma Processing Laboratory, McGill University, Department of Chemical Engineering, M.H. Wong Building, 3610 rue University, Montreal, Quebec, H3A 0C5

4.1 Abstract

A study has been undertaken of the degradation of carbon nanotube (CNT)-covered stainless steel mesh cathodes during exposure to low-pressure oxygen glow discharges. Emission spectroscopy and molecular absorption spectroscopy in DC glow discharge and in RF afterglow experiments, as well as morphological evidence, mass spectrometry spectra of condensed oxidation products, and molecular structure models have shown that plasma oxidation favors the production of 2,3 naphthalic anhydride. Absorption spectra taken during plasma oxidation match both literature sources for 2,3 naphthalic anhydride, as well as spectra of a chemical standard. MS data indicate that the only heavy compounds produced during plasma oxidation are poly-cyclic aromatics that can be attributed either directly to 2,3 naphthalic anhydride or to toluene, its major plasma decomposition product. Morphological observations using the scanning electron microscope support the conclusion that the reaction is facilitated by the field enhancement effect that accelerates oxygen ions to the tips of CNTs, where the oxidation takes place. Tests using water vapor show that oxidation is anhydrous, even in the presence of hydrogen.

4.2 Introduction

In recent years, work on carbon nanotubes (CNTs) has begun to shift from investigation of innate properties to scientific and technological applications, with the electronic

properties of CNTs becoming a particular focus of attention. Experiments and calculations have shown that the high aspect ratio of metallic CNTs leads to localized electric field enhancement when a standing field is applied [Zou et al., 2010]. This has the effect of concentrating the electric field, creating a much higher local field strength than that produced between two flat and bare metal electrodes. Theoretical work has extended the application of this phenomenon to arrays of CNTs on a metallic electrode, using regularly spaced CNTs to create wide area electric-field enhanced electron emission surfaces [Dionne et al., 2008]. This work has found experimental application in flat-screen scintillator displays and other high-vacuum devices [Kim et al., 2000, Neupane et al., 2012, Zhang et al., 2008].

Work has also begun to apply these field emission properties of arrays of CNTs to low-pressure gas devices [Tsakadze et al., 2010], making possible the use of CNT emitters in previously unforeseen applications like gas discharge light sources (e.g. fluorescent lighting) and plasma television displays. These types of devices are especially interesting for their potential to operate in the presence of alternative UV-source gases, which would address the growing concern over the current use of mercury vapor in all fluorescent bulbs and plasma screen devices. Water vapor has been identified as a UV-emitting species that could fill the place of mercury vapor [Shuaibov et al., 2008, 2009, General et al., 2010], but no successful application of CNTs as electrodes in a low-pressure gas discharge light source has been published.

In the process of working on the development of such a device, the work here reported seeks to explain the oxidation reaction mechanism for CNTs that are exposed to oxidizing species, which has been observed to severely affect CNT structures during glow discharge operation. An explanation of the mechanism of oxidation is important for future work, to decide whether the conditions can be exploited, for example by devising a technique whereby CNTs may be continuously rebuilt by in situ plasma

enhanced chemical vapor deposition [Richter and Howard, 2000], or if the CNT field-emitter approach must be entirely avoided for low-pressure gas discharge applications where oxidizing species are present.

With their electrical properties in mind, the current study sought to design CNT composite electrodes for use as replacements for conventional tungsten electrodes. The material comprises a layer of CNTs grown directly from a stainless steel (SS) surface [Baddour et al., 2009, Hordy et al., 2013], which has been used in the present study as an electrode in both direct current glow discharges and as a negatively-biased positive ion sink in radio-frequency discharge afterglow tests. The focus of the work is to determine the mechanism of oxidation, based on observations of the glow discharges produced using CNT-covered SS mesh cathodes, the nature of the degradation using electron microscope images, and analysis of reaction products. The degradation of CNTs has been studied and found to produce a single dominant species of polycyclic aromatic hydrocarbon: 2,3 naphthalic anhydride. The mechanism described here has been developed by combining observations of oxidative degradation in experiments with literature reports of theoretical models dealing with oxidation of CNTs and with reports of wet chemistry synthesis and chemical modification of similar species to those produced during the reported glow discharge plasma treatments.

4.3 Background

4.3.1 Plasma functionalization of CNTs

The covalent addition of species to CNTs by means of plasma functionalization has been reported in literature by numerous sources. Addition of oxygen ions to CNTs has been reported to produce unsaturated C-O bonds in the absence of hydrogen [Tseng et al., 2009]. The gradual covalent addition of oxygen species into CNTs has been shown

by X-ray photoelectron spectroscopy in [Felten et al., 2005, 2007]. Such studies have shown that carbonyl bonds form preferentially [Chen et al., 2011a, Zhao et al., 2012a] and FT-IR studies also show a tendency for oxygen to be added in unsaturated bonds, favoring carbonyl groups [Vandsburger et al., 2009]. In the absence of any external force, such as an electric field, oxidation was shown to occur preferentially at defect sites in the CNT lattice with no obvious point of localization on the surface [Tong et al., 2010]. No work has yet isolated the effect of localized electric fields on the oxidation of CNTs, but work has shown that field emission causes thermal degradation at the CNT tips [Dionne et al., 2009]. This indicates that the concentration of an electric field at the CNT tips would recruit positive ions to that location, thereby increasing oxidation.

4.3.2 Spectroscopy of polycyclic aromatic hydrocarbons

Polycyclic-aromatic hydrocarbons (PAHs) were identified as possible oxidation products through preliminary experiments, where initial molecular absorption measurements of the products of CNT degradation in pure O_2 showed broad absorption in the near UV range. Although many species other than PAHs absorb in this region, the class of low ring number anhydrides was judged to be the most likely species present, considering the system contained only graphitic carbon and oxygen. Gas phase molecular absorption spectroscopy was selected as the primary method to detect in situ molecular signatures, and mass spectroscopy (GC-MS) was chosen to identify equilibrium products.

The seminal work in the field of UV absorption spectroscopy of PAHs was published by Friedel-Orchin, in 1951 [Friedel and Orchin, 1951]. This work reports an exhaustive collection of absorption spectra for qualitative identification of unknown hydrocarbons. Although the Friedel-Orchin index contains spectra for hundreds of compounds, the carboxylic anhydrides of napthalene will be discussed specifically, since they are the focus of the current work. A characteristic spectrum for 2,3 napthalic anhydride consists of a

broad absorption band between 220 and 380 nm that has a fine structure between 270 and 350 nm and a strong absorption band between 220 and 270 nm corresponding to typical absorption by aromatic rings. The spectrum given for 1,8 napthalic anhydride lacks a fine structure, but shares the aromatic absorption band. This description is corroborated in two reports by Barros et al. on the photophysical and photochemical properties of PAHs. In the first, the UV absorption spectra of 1,8 and 2,3 naphthalic anhydride and their associated acids are presented [Barros et al., 1993]. The second also deals with 1,8 and 2,3 naphthalic anhydrides, and describes in detail the hydrolysis of their respective structures, focusing on kinetics, but again showing the effect of bond saturation on absorption of UV photons [Barros et al., 2001]. The presence of the unsaturated dicarboxylic group, with both carboxyl groups linked by a shared oxygen atom, produced in both species a pronounced absorption band near the long wavelength limit of the UV range. For 2,3 naphthalic anhydride the absorption band appeared between 320 and 390 nm with a maximum value occurring at approx 360 nm and a noticable shoulder from 340 to 350 nm. The absorption band of 1,8 napthalic anhydride occurred in a shorter wavelength range, between 275 and 370 nm and was more symmetrical. In both molecules, hydrolysis of the ether-type bond between the two molecules eliminated this peak, but absorption due to aromatic rings remained at 260 nm. The absorption band of naphthalic anhydride at 260 nm is also reported in other work, [de Barros et al., 2011, Hrdlovic et al., 2001].

4.3.3 Oxidation reaction mechanisms of aromatic hydrocarbons and CNTs

Reaction mechanisms of partial oxidation of PAHs and covalent oxidative functionalization of CNTs have been shown to occur in several specific ways, depending closely on the structural conformation of aromatic rings, and in the case of CNTs, on both lattice chirality and CNT shell symmetry and diameter. Synthesis of pthalic anhydride

from a simple aromatic precursor was first reported by Gibbs and is now known as the Gibbs-Wohl Oxidation of Naphthalene. Ortho-xylene can also be oxidized to phthalic anhydride. In most reported synthesis mechanisms, ortho or para arrangements are preserved during oxidation [Marx et al., 2011, Wang et al., 2007]. Oxidation of anthracene forms di-carboxylated anthraquinones [Parker, 1970], which can also be a precursor to the formation of phthalic anhydride by further decomposition [Bruckner and Baerns, 1997].

Work on plasma oxidation of aromatics also addresses the formation of poly-cyclic aromatics. RF plasma synthesis of higher ring number PAHs from benzene has been shown to be inhibited by the presence of oxygen in the gas mixture [Shih et al., 2005]. Where in inert plasmas higher order structures were generated, including up to seven ring compounds, the presence of oxygen in the plasma gas removed all traces of multi-ring aromatic hydrocarbons from the reaction products.

Oxidation of CNTs has the added complexity of chirality and lattice strain that modifies the preferred oxidation sites and the types of oxidation that occur. Theoretical models have shown that addition of single oxygen atoms occurs preferrentialy at C-C bonds that are placed at a minimum angle from the CNT axis [Guo et al., 2010a]. This position corresponds to the 2,3 para location of the carbon rings that make up a CNT. Another work by the same author predicts the effect of lattice strain on oxidation, where oxidation is found to occur first at locations of highest curvature in the CNT lattice, when curvature is non-uniform [Guo et al., 2010b]. These findings are corroborated by other researchers who have further found that the epoxide bond is the most energetically stable form of singlet oxygen addition to CNTs [Zhang and Liu, 2006], and that other bond types can be annealed to epoxide bonds. In the case of addition of molecular oxygen, oxygen atoms will also prefer the 2,3 para locations, forming a square bonded structure with the carbon pair of the CNT [Guo et al., 2010a]. Molecular simulations from the

same study show that the oxygen pair can spontaneously rearrange into carbonyl groups by breaking the bonds that join both the oxygen pair and the carbon pair, forming a ten member ring with carbonyls at the 1 and 6 positions. The mobility of oxygen atoms on the surface of CNTs and the potential for an external driving force to facilitate oxygen bond rearrangement are important concepts, as they form a basis for the oxidation mechanism proposed later.

4.4 Methods

An experimental plan was devised to test CNT-covered SS meshes as cathodes, with the added factor that the water vapor-containing glow discharge produced should exploit the UV emission band of OH to produce UV photons. Samples would be negatively biased using a DC power supply, and the glow discharge produced between these CNT cathodes and the grounded chamber would be characterized and studied for its UV emission intensity, as well as for any important chemical compounds produced during operation. Since degradation of CNTs by oxidizing plasmas had been observed in previous work [Vandsburger et al., 2009], a principal goal of the work was to understand the form and manner of oxidation. To help with this, DC discharge tests were accompanied by RF afterglow tests, designed to reduce the effects of surface heating and ion-induced sputtering often associated with high surface ion fluxes, and to allow for operation in pure oxygen.

4.4.1 Sample preparation

CNT-covered SS cathode samples used for all experiments were produced using a thermal-chemical vapor deposition method developed in our group for growing CNTs directly from, and anchored to, a SS surface [Baddour et al., 2009, Hordy et al., 2013, Vands-

burger et al., 2009]. This method produces uniform coverage over the entire SS surface and reliably produces electrically conductive, multi-wall nanotubes (MWNTs) which are in good electrical contact with the SS substrate. In the interest of clarity, MWNTs will henceforth be referred to as CNTs, since the oxidation discussed does not strictly depend on the number of concentric walls present in the CNT samples. SS type 304 was used as the substrate, with a wire size of 400 mesh, acetylene as the carbon source gas, and argon as the inert carrier gas.

4.4.2 Experimental setup

CNTs were oxidized in a cylindrical chamber designed to be used for either DC or capacitively-coupled RF (13.56 MHz, continuous wave) glow discharge generation, shown in Fig. 4.1. The chamber uses a dual-purpose counter electrode that acts as a grounded anode for DC experiments and as a live electrode in RF experiments. The CNT-covered SS mesh cathodes were attached to a dual-polarity DC power supply. This was used to negatively bias the CNT sample for both DC and RF operation modes. Pure O_2 was supplied for RF tests and mixtures of O_2 and Ar or pure Ar were used for DC tests. The chamber reliably held a base pressure of approximately 5-10 mTorr for the rotary stage and $1x10^{-}6$ Torr with the turbo stage running.

In RF experiments the plasma formed between the live electrode and the grounded plasma chamber, upstream of the sample position. Two vacuum cross sections were installed on either side of the reactor section wherein the sample would be placed. The downstream cross was equipped with two quartz windows, for use as a molecular absorption spectroscopy path, while the upstream cross was equipped with a quartz window only on one side, for emission spectroscopy of the RF discharge itself. A 300 W incandescent tungsten lamp was used as the light source for all molecular absorption spectroscopy measurements. Organic vapors were condensed onto compressed carbon

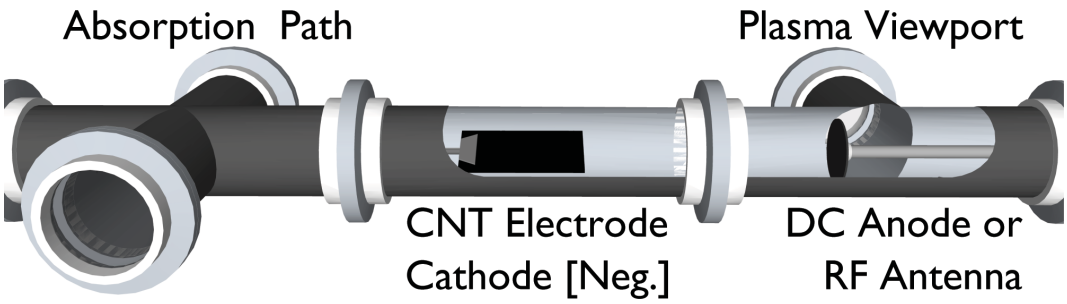

Figure 4.1: Diagram of the electrode arrangement and quartz viewports in the discharge chamber setup

pellets during RF experiments.

For DC experiments, the central sections, including both crosses, were replaced by a double-ended Pyrex glass break to allow for direct visualization and control of the negative glow. It was considered important to control the extent of normal glow for three reasons, since it would be used as a means to obtain information about the stages of oxidation, to gather information about the structure of the negative glow produced by CNT covered mesh cathodes, and to prevent any degradation of the DC feedthrough from affecting the analysis of reaction products.

4.4.3 DC plasma oxidation experiments

Direct current experiments were intended to mimic as closely as possible the conditions considered in work on CNT-emitter arrays in low-pressure glow discharges. A mixture of water vapor and argon was used as discharge gas to investigate the potential for using the hydroxyl ion as a UV-photon source, as previously discussed. The pressure in the chamber was kept at 3 Torr for all experiments, with a 1:1 mix of argon and water vapor. Water vapor was used since it had been identified as an alternative UV-photon source gas in the literature, but experiments using mixtures of Ar-O_2 were also done, following

indications that CNT degradation proceeded by anhydrous oxidation. Argon was fed to the chamber via a mass flow controller, while the water vapor was added by evaporation from a wetted sponge that was held in a separate chamber. The flowrate of Ar was set at 35 sccm and the vacuum bellows valve was adjusted to a stable pressure of 1.5 Torr. A manual butterfly valve controlled the flow rate of water vapor, which was adjusted to maintain the total chamber pressure at 3 Torr. After breakdown, the discharge current was limited to 20 mA by the DC power supply. During discharge operation the negative glow was photographed and the light emitted was analyzed from 300 to 900 nm, subject to the lower limit of transmission of the Pyrex glass break.

Molecular absorption measurements were also taken during DC experiments, although these were done in pure oxygen at 5 sccm and not in water vapor. The chamber was sealed prior to molecular absorption tests to measure the effect of species accumulation. An absorption spectrum for a given time during an experiment was found by calculating the logarithm of the quotient of the initial spectrum and the spectrum taken at that time. A temporal reference spectrum was used as a blank, taken before plasma treatment. CNT samples were imaged in the SEM before and after DC glow discharge experiments to demonstrate the extent of the CNT degradation, as well as to asses whether there was any localization of the degradation. Images showing the intermediate stages of CNT oxidation were taken using a Hitachi S4700 field-effect scanning electron microscope (FESEM) operating at 10 kV and 10 μA.

4.4.4 Radio-frequency O_2 afterglow experiments

RF discharge afterglow operation was chosen as a less aggressive environment that allowed CNTs to be oxidized in a controlled way. This was done over concerns that alternative degradation mechanisms could have been responsible for the observed destruction of the CNTs. The operating pressure was reduced to the range between 0.1 to

2 Torr to allow for the RF afterglow to reach the CNT samples, and maintained at 0.75 Torr during gas condensate collection experiments. All experiments were undertaken in pure oxygen at a RF plasma power of 30 W. The RF plasma afterglow was characterized before running CNT degradation tests. A single tip, ground-referenced Langmuir probe was used to determine the plasma potential and ion density. Plasma parameters were determined from 25 measurements taken at the operating conditions and at a fixed location, corresponding to the position of the sample in the chamber. These are presented in Table 4.1. The plasma potential and floating potential values allow for the correction of the applied bias to match the discharge voltage of DC tests. A positive floating potential indicates that the sample will attract anions when grounded, so negative control experiments were completed with the sample disconnected from any circuit. Emission spectra were collected from the RF glow as a means of assessing the purity of the plasma gas. The presence of ions confirms that at the position of the sample the RF afterglow did provide oxidizing species for CNT degradation. Furthermore, the plasma was found to produce exited states of molecular O_2, determined by emission spectroscopy to consist almost entirely of singlet oxygen. The composition of the plasma is important when considering the mechanism of oxidation, as will be discussed in later sections.

Table 4.1: Characteristic parameters of the RF O_2 afterglow at 0.75 Torr (30 W)

Parameter	Value	Units
Plasma Power	30	W
Floating Potential	12.21	V
Plasma Potential	52.49	V
Electron Density	2.78×10^9	cm^{-3}
Ion Density	1.15×10^9	cm^{-3}

Molecular absorption spectroscopy in RF afterglow experiments followed the same

procedure as for DC experiments, but with the added range of 220 to 380 nm, using the quartz window pathway. Molecular absorption spectra in the UV range were collected separately from the visible range and used longer integration times because of weak UV emission from the tungsten filament lamp that was used as the continuous lightsource. Gas condensate samples were analyzed by a GC-MS headspace analyzer equipped with a non-polar column.

4.5 Results and Discussion

4.5.1 Water vapor and anhydrous oxidation

After the breakdown voltage was reached, a negative glow would form on the face of the CNT-covered SS mesh cathode. In experiments using Ar-H_2O mixtures, gaseous breakdown would typically occur between 370 and 400 V, and the discharge voltage would range between 250 and 280 V. These values were consistent with discharge voltages for Ar-O_2, since in both cases the Ar comprised half the chamber pressure.

During glow discharge operation in argon/water vapor mixtures a distinct red hue could be observed in the negative glow covering the CNT-covered cathodes, as shown in Fig. 4.2. Emission spectra collected during these tests contain atomic emission lines from argon and water decomposition products as well as molecular emission bands. The hydroxyl band at 309 nm was observed as was the H_α line at 656 nm. In CNT trials, the oxygen emission line at 777 nm was absent, which dominates in discharges of pure O_2, but a significant signal was detected from H_α. Emission from H_α in the negative glow was strong relative to the level observed with DC glow discharge experiments using bare SS cathodes. The difference in emission level of the H_α line between the CNT-covered samples and bare SS control samples is demonstrated in a magnified spectrum shown in Fig. 4.2b.

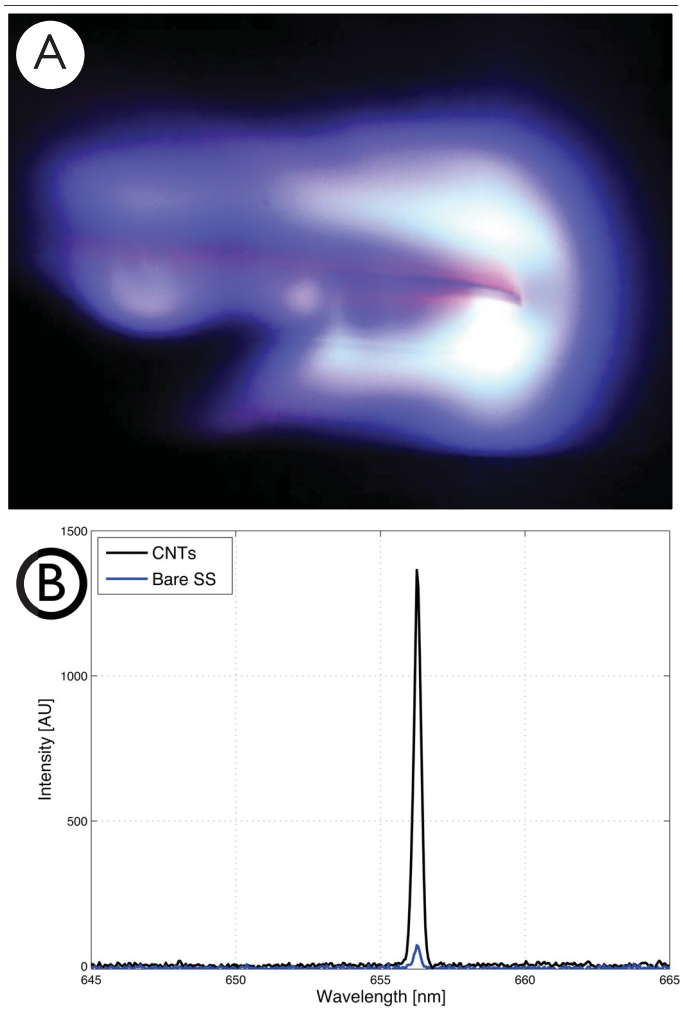

Figure 4.2: Red surface glow observed with CNT-covered SS cathodes in Ar-H_2O. **A:** The overall appearance of a CNT-covered SS mesh sample and **B:** the emission spectrum from the negative glow around the Hα emission line, shown against the emission from a bare stainless steel cathode.

Evidence from both types of experiments indicated that CNTs were degraded by anhydrous oxidation, even when atomic hydrogen was present, as in DC experiments where oxygen was produced by dissociation of water vapor. In the atomic emission spectra taken from DC glow discharge experiments with the CNT-covered cathodes in Ar and H_2O, the H_α emission intensity was approximately fifteen times larger than with the bare SS cathodes under otherwise similar conditions. Since the gas composition and discharge current were held constant for both types of experiments, and the discharge voltage did not vary significantly, the reproducible difference in H_α emission between CNT-covered samples and bare SS samples is attributable to the degradation process. It seems that the oxygen produced by dissociation of water vapor is consumed by CNT oxidation reactions, leaving an excess of hydrogen atoms near the cathode surface. This is supported by literature reports stating that O_2 scavenges active hydrogen and reduces its spontaneous emission [Nozaki et al., 2012]. The consumption of O_2 would therefore explain the greater emission from $H\alpha$.

Emission spectra from RF afterglow experiments with pure oxygen did not show a stronger signal from H_α, but instead showed the presence of water vapor and nitrogen gas from their UV signatures. Hydroxyl groups were present, as were N_2 molecules, but no signs of dissociation of N_2 or atomic hydrogen were found, and the signal from atomic oxygen was an order of magnitude higher than the next strongest impurity.

4.5.2 CNT degradation

The process of CNT degradation was captured in a series of SEM images, as shown in Fig. 4.3. These images were taken from a single sample that had been used as a cathode in a pure oxygen DC discharge. The gas pressure and discharge current were controlled in such a way to limit the discharge to only a small portion of the cathode surface, so the ion density decays with increasing distance from the center of the negative glow. Thus,

a series of images taken at progressively larger distances from the edge of the glow discharge reveals the effect of oxidation rate and the overall CNT degradation profile. Specifically, images were taken every 1 mm, over a distance of about 1 cm. Although all the images presented were taken from the same sample, the effect was consistent in all samples observed. They show a uniform decrease in CNT length that is proportional to discharge intensity, and thus to the extent of degradation, without a noticeable impact on the density of the CNT layer.

It can also be seen from the SEM images that the rate of degradation is not initially uniform. Longer CNTs have considerable length reduction in early stages, but when the length of the CNT layer becomes nearly uniform, the degradation rate becomes consistent across the surface and much slower. The slowing of the degradation rate can be attributed to the conservation of the ion flux, being distributed over more CNTs. From this it can be surmised that field enhancement occurs first at select CNTs, either the longest or the least defective. One may also note that field enhancement effects also occur away from the tip on CNTs and field emission applications of horizontally aligned MWNTs have been reported in literature [Jung et al., 2007]. In this way, ions reaching the surface of a CNT felt-like structure could be directed to the sidewalls of curved CNTs, as these constitute conductive cylinders having a nanoscale diameter.

RF experiments did not show the degradation as clearly as with the DC experiments, because the surface ion flux was purposefully limited by placing the CNT cathodes in the RF afterglow. In DC tests the current in the circuit was controlled, and kept at 20 mA, while in RF tests the current was measured, and was found to remain below 1 mA. The difference in current between DC and RF trials indicates that the total ion bombardment rate was reduced by approximately 20-100 times. The ion concentration in the afterglow, as measured by the Langmuir probe, was sufficient to oxidize the CNT tips, but did not produce the more aggressive conditions prevailing in DC experiments.

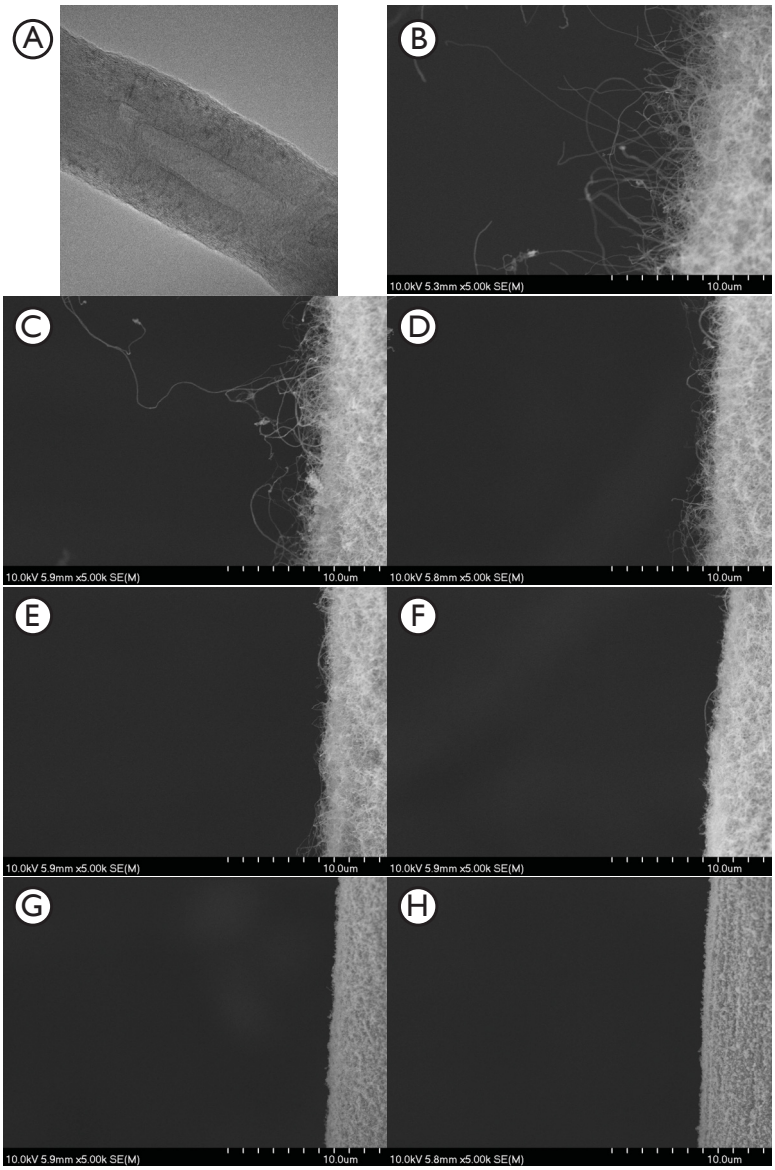

Figure 4.3: Profile of CNT degradation obtained by exposure to a non-uniform DC discharge in Ar-H_2O for 30 min. **(A)** TEM image of a CNT from the sample; **(B)-(H)** gradually increasing exposure (proceeding toward the region of strongest glow intensity). **(H)** complete degradation by oxidation is observed. Any two consecutive SEM images correspond to locations on the CNT-covered SS mesh cathode separated by 1 mm.

The limitation of the surface ion flux was intended to eliminate the possible role of ion bombardment as a source of CNT degradation, through thermal oxidation or by sputtering, since both are common causes of CNT erosion during DC glow discharge operation. In this way, the consistent results observed in the spectroscopic data collected from DC and RF experiments indicate that plasma oxidation is likely the principal cause of the significant degradation of CNTs in DC glow discharge experiments, and that tip-based oxidation was also occurring under RF afterglow exposure.

4.5.3 Radio-frequency O_2 afterglow

Molecular absorption spectra taken during DC glow discharge experiments showed a strong and broadband absorption peak centered at 350 nm, with an indication of fine structure at shorter wavelengths (Fig. 4.4). These spectra were taken after 30 min of DC operation, for a glow that was restricted to a region far from the electrical connection. To check against a potential match for a broad absorbance at 350 nm, which was identified as a signature region in [Friedel and Orchin, 1951], a pure sample of 2,3 napthalic anhydride (cas# 716-39-2, Sigma Aldrich) was vaporized into the chamber after dissolution in anhydrous ethanol, without the presence of any plasma discharge. Anhydrous ethanol was chosen as the solvent due to its low cutoff wavelength of 210 nm. These spectra also showed an absorption band in the same wavelength range, which is shown, in black, in Fig.4.4.

RF discharge afterglow experiments offered another means to verify and expand on the findings from the DC glow discharge experiments. CNT samples were biased at -200 V, to produce an overall potential difference equivalent to the discharge voltage of DC tests when considering the +53 V plasma potential. A typical emission spectrum of the RF afterglow in pure O_2 is shown in Fig. 4.5. This spectrum was collected with quartz windows mounted on the chamber to allow for a greater signal at wavelengths

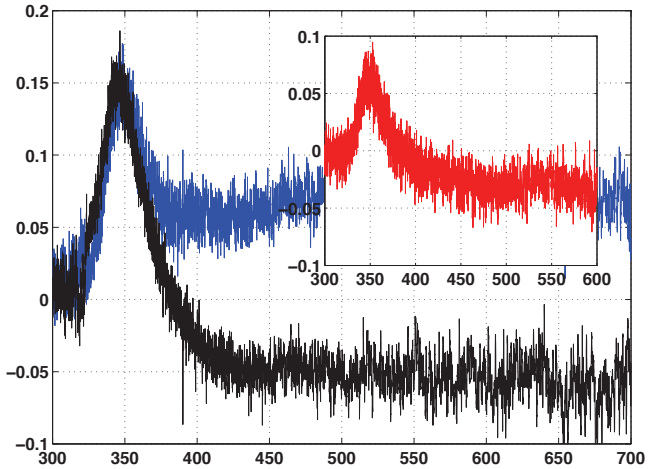

Figure 4.4: Molecular absorption spectra from: **Blue**- a DC glow discharge in Ar-O_2 showing a strong and broad absorption peak centered at 350 nm, **Black** - the pure chemical 2,3 napthalic anhydride vapor, and **Red** (insert) - downstream of the sample in a pure O_2 RF afterglow at 30 W.

shorter than 300 nm. The major emission peaks have been labeled on the figure. Peak identification was made from literature sources [Franceschi et al., 2007, Xie et al., 2005, General et al., 2010]. All peaks correspond to spontaneous de-excitation processes with the exception of the one at 329.4 nm, which is a fluorescence peak attributed to naphthalene. It is important to note the absence of the Swan band of C_2 which normally appears between 450 and 650 nm due the presence of short carbon chains in the plasma gas.

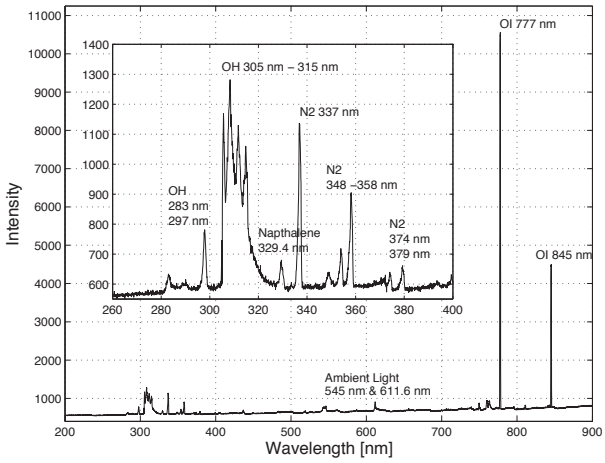

Figure 4.5: Emission spectrum from a RF discharge afterglow at 30 W in pure O_2. Inset: Near-UV range.

Molecular absorption spectra were collected over the UV and visible ranges. For RF discharge afterglow experiments, the near UV-visible range measurements reproduced what was seen in DC experiments, with absorbance observed in the range of 330-380 nm. A spectrum taken after 30 minutes is shown, in red, in Fig. 4.4. A spectrum collected in the UV-range is shown in Fig. 4.6. Spectra collected in this range featured a fine structure between 270 and 340 nm that reproduced the list of peaks found in the standard spectrum of Friedel and Orchin[Friedel and Orchin, 1951]. These peaks

were consistently observed in repeated experiments and are listed in Table 4.2. The Friedel-Orchin spectrum was not printed at high resolution, so peak wavelengths given in Table 4.2 are estimates. Absorbance bands were also seen in the range of 220 to 265 nm, corresponding to aromatic molecules. A weaker absorbance band was observed between 330 and 380 nm, corresponding to the band seen in UV-visible measurements.

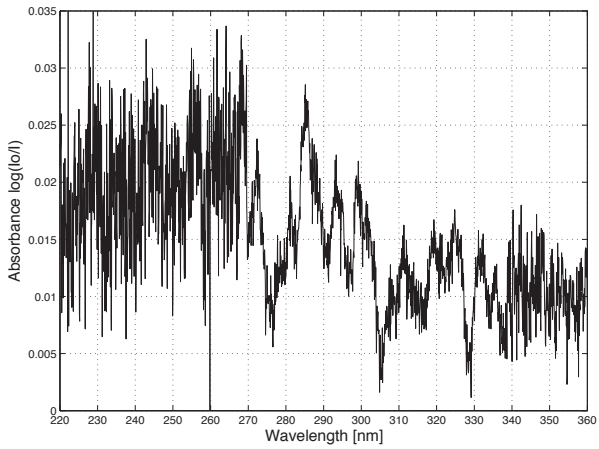

Figure 4.6: UV molecular absorption spectrum for RF discharge in pure O_2 afterglow test with structure matching 2,3 napthalic anhydride.

Absorption spectra provide the clearest indication of the oxidative formation of PAHs in situ. Although aromatics are shown in GC-MS data, these are collected downstream in a cold zone, and so are condensation products. Absorption spectra, on the other hand, were collected in the gas and can be considered to show non-equilibrium products. The spectra in the near UV-visible range, in Fig. 4.4, show a peak that fits the pattern of 2,3 naphthalic anhydride found in several literature sources as well as matching a spectrum taken of pure 2,3 naphthalic anhydride vapor. The position of the peak in all cases further indicates that the form produced during oxidation is the 2,3 and not the 1,8 isomer, and although aminated derivatives of 2,3 naphthalic anhydride

Table 4.2: Peaks observed in RF afterglow molecular absorption measurements [nm]

Peaks in Standard	Peaks in Sample
270	272
282	282
–	285
293	293
–	299
305	304
318	319
327	325
335	333
–	337

compounds also absorb in the same range [Barros et al., 1993], the similarity to the pure substance and the absence of a signal from singlet nitrogen in emission measurements reduce the likelihood that amines form a large part of the oxidation products. The presence of naphthalene derivatives is also indicated by the fluorescence detected in the emission spectra collected during RF afterglow experiments. The fluorescence peak of naphthalene at 329.4 nm has been reported in the literature [Xie et al., 2005].The presence of poly-aromatics in the glow discharge itself also serves as strong evidence for the production of poly-aromatics as non-equilibrium products.

The fine structure observed in spectra taken from 220 to 380 nm further demonstrates the presence of 2,3 naphthalic anhydride. The peaks identified in the absorbance spectra match closely with estimates taken from spectra reported in the literature, since no quantitative source could be found. Qualitatively, the spectra had the characteristic absorbance structure of 2,3 naphthalic anhydride, with a relatively strong absorbance

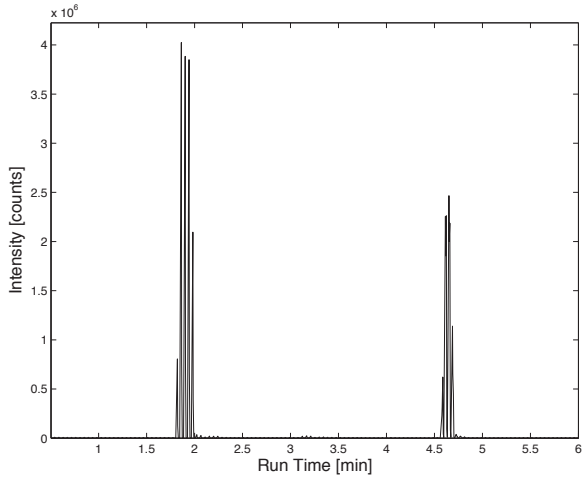

Figure 4.7: Chromatogram for GC-MS headspace measurement of 60 min, 30 W RF afterglow experiment with pure O_2. Left peak corresponds to Fig. 4.8, and right peak corresponds to Fig. 4.9

in the aromatic range between 220 and 265 nm as well as in the 330 to 380 nm range that corresponds to the absorption in the near UV-visible range. The anhydride group absorbs differently from the saturated acid, so the presence of peaks associated with the fine structure of the anhydride helps to support the conclusion that CNT degradation occurs by anhydrous oxidation.

PAHs are also characterized using GC-MS and LC-MS. Phthalic anhydrides and naphthalic anhydrides can be detected in the gas phase, and have parent ion masses of 148 and 198, respectively [Kautzman et al., 2010, Reisen and Arey, 2002]. Mass spectra of samples produced during RF discharge afterglow experiments confirmed the presence of a species with the same peak signature as either 1,8 or 2,3 naphthalic anhydride. Signatures of single ring aromatics were also detected in a later portion of the chromatogram, corresponding to less polar structures, since the GC-MS used a non-

polar column. The strongest signal was found from aromatic rings and from PAHs. The chromatogram presented in Fig. 4.7 was produced during analysis of a sample collected from the same experiment that produced the absorption spectrum shown in Fig. 4.6. The first peak, centered at 1.8 min, was primarily composed of air, along with a PAH that matches the signature of 2,3 napthalic anhydride. The second peak, centered at 4.6 min, was composed almost entirely of a single ring hydrocarbon that was identified as toluene. Mass spectra are given for both of these compounds, in Fig. 4.8 and Fig. 4.9. The signatures identified were found in samples collected during all RF discharge afterglow experiments, and the signatures of phthalic anhyride and anthraquinone were absent from all MS measurements.

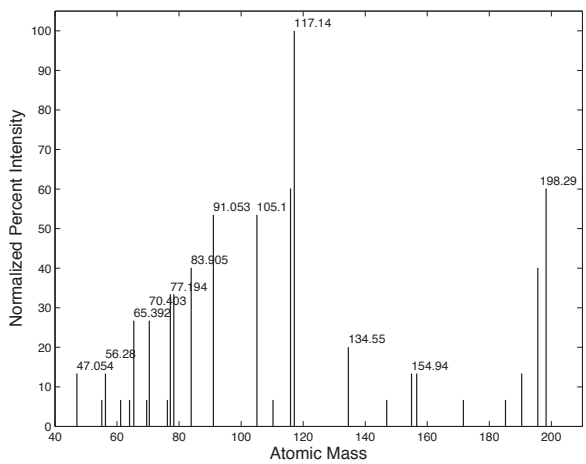

Figure 4.8: Mass spectrum taken from first peak, matching signature of 2,3 napthalic anhydride. Parent ion mass is 198 amu.

Mass spectroscopy provides the final confirmation that PAHs are the principal condensible products of the oxidation of CNTs. The only compounds detected in mass spectra were aromatics or fragments of aromatics. The most prevalent parent ion in mass

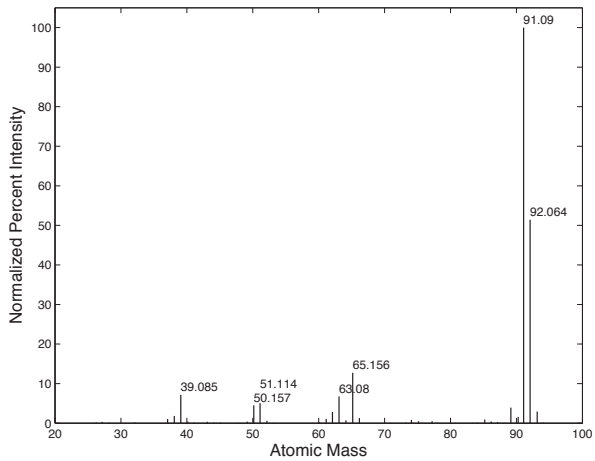

Figure 4.9: Mass spectrum taken from second peak, matching signature of toluene. Parent ion mass is 92 amu.

spectra was toluene, which is not a significant part of the fragmentation pattern of 2,3 naphthalic anhydride. Toluene was detected as a distinct peak of the gas chromatogram, so it is most likely a plasma decomposition product of 2,3 napthalic anhydride, being present in the GC prior to exposure to fragmentation in the MS. Furthermore, carboxylic anhydride groups are susceptible to further oxidation to CO and CO_2 [Onwudili and Williams, 2007], and the oxidation of 2,3 napthalic anhydride produces either toluene or xylene. Oxygen radicals and ions are numerous in low-pressure O_2 glow discharges, so plasma decomposition is common, as discussed in previous work on the subject that showed the reduction of PAHs to single ring aromatics in oxygen containing discharges [Shih et al., 2005].

4.5.4 Single Point Energy Comparison

Molecular structure models help to explain the experimental findings, and can be used to support the experimental evidence of formation of the carboxylic anhydride group. Two oxygen molecules in the square bonded orientation and one epoxide bonded oxygen atom are required for the formation of one carboxylic anhydride group. To judge the relative stability of these structures, their single point energies were calculated. The carboxylic anhydride was found to be the lowest energy structure, so it serves as the reference energy. The structures were modelled using the molecular visualization software, Avogadro, which allows both visualization and analysis [Hanwell et al., 2012]. The lowest energy state of each structure was found by a geometry optimization method using a MMFF94 force field and the steepest descent algorithm, with 500 steps and convergence set at $10x10^{-}7$. The single point energies and corresponding structures are shown in Fig. 4.10. The formation of the anhydride from two oxygen molecules and one oxygen adatom gives a net energy change of at least -1.68 eV. In addition, once the anhydride is formed, geometry optimization shows that the group rotates away from the axis of the CNT. This will serve to increase the energy requirement of any reverse reactions. Although a reaction pathway cannot be inferred from these values, without accurate estimations of transition state energies, previous first-principles models can help provide a system-specific hypothesis for the progress of the reaction.

The oxygen glow discharges produced during experiments were found to be composed mainly of molecular ions, so adsorption of square bonded oxygen molecules is likely the beginning of the process. The square bonded oxygen admolecule will spontaneously form a carbonyl pair, with a overall energy change of -1 eV, which concurs with findings reported in literature [Guo et al., 2010a]. This is also supported by experimental work on covalent plasma oxidation of CNTs, as discussed previously. The migration

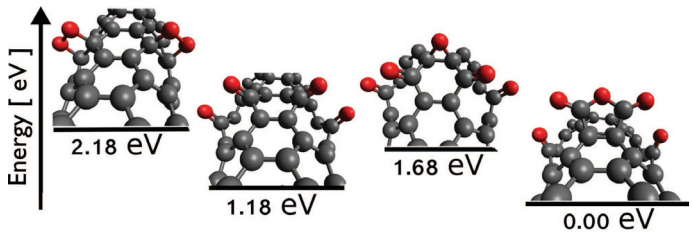

Figure 4.10: Hypothetical structures formed by oxygen adatoms and a CNT, from left to right: Square bonded ad-molecules; A ten member ring with two carbonyl groups; An epoxide bonded O adatom in the 2,3 position; And the carboxylic anhydride group, rotated away from the CNT axis.

of the oxygen adatom into higher energy positions can be induced by a strong electric field, as shown in literature [Zhao et al., 2012b]. It was found in that study that under an applied field of 1 V/Å, oxygen adatoms can migrate into new positions on the surface of a CNT requiring an energy change far exceeding +0.5 eV. Due to the presence of cathode sheaths and constriction of the glow to the surface of DC electrodes, as well as field enhancement, the voltage drop on the CNT tips could reach these levels.

4.6 Conclusion

Oxidation by exposure to low-pressure oxygen glow discharges of CNTs grown on a metal cathode has been found to selectively produce poly-cyclic aromatic hydrocarbons. The findings of molecular absorption spectroscopy indicate that the 2,3 carboxylic anhydride is favored instead of the 1,8 structure, which further limits the possible explanations of the reaction mechanism. SEM images show that CNT oxidation first occurs at long CNTs extending beyond the entangled felt-structure, and is then localized to the CNT tips and progressively shortens the CNTs until complete oxidation occurs. Molecular structure models based on a SWNT compare the energies of adsorbed oxy-

gen molecular ions to carbonyl bonded structures and finally to carboxylic anhydride groups. These findings indicate that oxygen will prevent long term functioning of CNT composite electrodes at the voltages that are currently required for operation in low-pressure applications. Nitrogen gas can also be used as a UV-photon source, and will not form the same dicarboxylic anhydride group in the absence of oxygen, so it will be examined as an alternative to water vapor. The effect of externally applied DC bias, discharge voltage and thus, the energy with which ions reach the CNT tips will be a focus of further study, to assess whether CNTs will withstand a less aggressive environment.

4.7 Acknowledgments

The authors acknowledge the financial support provided by the Natural Sciences and Engineering Research Council of Canada (NSERC), the Fonds de recherche du Québec - Nature et technologies (FRQNT) and McGill University. The authors also acknowledge the technical support provided by Mr. Ranjan Roy and Mr. Frank Caporuscio.

CHAPTER 5

THERMAL DEGRADATION OF MWNTS BY ELECTRON BOMBARDMENT

Preface

This chapter presents the results of a further study of MWNT-plasma interactions has been published in *Journal of Physics D: Applied Physics* [Vandsburger et al., 2013b]. The work was planned, executed, and analyzed by L. Vandsburger. Research supervision and reviewing of the manuscript were the shared responsibilities of the two academic advisors, S. Coulombe and J.L. Meunier.

The citation for the following chapter is:

> L. Vandsburger, S. Coulombe, J.L. Meunier. *Electron Bombardment Degradation of Carbon Nanotubes in Radio Frequency Discharge Afterglows*. **Journal of Physics D: Applied Physics** Volume 46-47, November 2013, 485301.

MWNT-covered stainless steel mesh samples were prepared as described in the methods section and were positively biased to elicit electron bombardment. This chapter complements the study presented in Chapter 4 and helps to improve our understanding of the effect of charged particle bombardment on CNT stability. Although no estimation of the temperature of the CNTs is possible, the thermal nature of the degradation process is concluded from the nature of the organic products that are detected in GC-MS measurements and by kinetic modelling of the optical emission from important oxidation species, such as CO and O.

It has been found that MWNTs degrade into short unsaturated hydrocarbons during electron bombardment. The degradation is not due to chemical reaction, because only unsaturated hydrocarbon fragments, lacking any oxygen groups, were detected in

MS spectra. In oxygen limited plasma oxidation, the oxygen consumption reaction was found to proceed by a fractional order reaction rate. Fractional order reactions are typical of oxidation systems where the concentration of the carbon source is decoupled from the oxygen concentration. This indicates that carbon in the plasma is produced by an external process, which in this case is thermal evaporation by electron bombardment.

Degradation of carbon nanotubes by electron bombardment in radio frequency glow discharge afterglows

L. Vandsburger, S. Coulombe, J.-L. Meunier

Plasma Processing Laboratory, McGill University, Department of Chemical Engineering, M.H. Wong Building, 3610 University St., Montreal, Quebec, H3A 0C5

5.1 Abstract

A capacitively coupled RF afterglow is used to isolate the role of electron bombardment in the degradation process of muti-walled carbon nanotubes (MWNTs). MWNTs grown on a metal substrate act as a nanostructured anode that accelerate and focus electron bombardment, facilitated by the field enhancement effect. Tip localized MWNT degradation has been observed in SEM images showing the progression of the MWNT degradation process. GC-MS measurements indicate that the major products of MWNT degradation are short unsaturated hydrocarbons, identified as both propyne and 1,3-butadiyne vapors. This finding is corroborated by time-resolved optical emission spectroscopy during plasma oxidation of the degradation products. Analysis of the kinetics of plasma oxidation confirm that MWNT degradation produces species consistent with thermal evaporation, such as short carbon chains, C3-C4, but not monatomic or diatomic species, C1 and C2.

5.2 Introduction and Background

In recent years, research work on carbon nanotubes (MWNTs) has advanced from fundamental investigations of physical and chemical properties to development of new applications. It has become clear that the possible applications of MWNTs in technology are wide ranging, and extend from continued efforts in composite materials to work on

biocompatible electronics and nanocomposite electronic materials [Bakshi et al., 2010, Bokobza, 2007]. With the expansion of MWNT technology into new fields, new issues and limitations are becoming apparent. These include potential mutagenicity and unforeseen incompatibility with various media [Roldo and Fatouros, 2013, Hordy et al., 2013]. Although much is known of single walled carbon nanotube (SWNT) and MWNT chemical funtionalization [Hodge et al., 2012], little is yet understood of the reactivity of carbon nanotubes in energized gas systems. This article reports an effort to aid in the development of the application of MWNTs for low pressure electrical discharge devices, by helping to better understand MWNT-plasma interactions. It has been found that MWNTs are degraded by exposure to low pressure discharges [Vandsburger et al., 2013a], and it is the goal of this work to describe the chemistry of MWNT degradation that results from electron bombardment during operation of MWNTs as a nanostructured anode.

Numerous potential applications have spurred considerable research into MWNT-field emission devices [Nakahara et al., 2011, Heo et al., 2010]. Research into failure mechanisms of MWNTs during field-emission has produced important findings describing the various phenomena that govern the destructive failure of MWNTs [Baik et al., 2010]. In general, field emission has been found to induce destructive failure by resistive heating caused by electron conduction [Huang et al., 2004, Bonard et al., 2003], by tip-localized phenomena[Wang et al., 2002], and by mechanical vibrations [Bonard et al., 2003]. All these reports deal with systems under ultrahigh vacuum, but gas pressure has been shown to have an effect on field emission properties [Vasil'eva et al., 2012]. The effect of electron current is most important to the work reported here, since field emission and its related effects are negligible in glow discharges sustained with metallic electrodes.

The effect of resistive heating has been found to produce evaporation of MWNTs

in experiments where the effect of current was isolated. The effect of joule heating has been found to induce temperatures up to 2000 K along the lengths of MWNTs [Purcell et al., 2002], and electrical current has been shown to cause heating of MWNT composite materials to the point of incandescence [Natarajan et al., 2011]. When placing a counter-electrode in direct contact with the tips of MWNTs making up an aligned MWNT array, it was found that electrical current caused failure at the midpoint of the MWNT lengths [Bonard et al., 2003]. This finding was supported by theoretical work treating MWNTs as solids with a given resistance, thermal conductivity and heat of vaporization [Dionne et al., 2009]. Direct bombardment by high-energy electrons has been found to produce holes in SWNT lattices [Rodriguez-Manzo and Banhart, 2009], although in this instance the electrons were directed in a beam, and were not attracted by an electric field. No work has yet been reported describing the products of joule heating failure of MWNTs, but work on laser ablation of graphite and graphene targets for MWNT synthesis has found MWNT precursors in the laser plume to be short, unsaturated hydrocarbons [Ikegami et al., 2004, Voevodin et al., 2002].

The interaction of MWNTs with low-pressure gas discharges is also an active area of research. This is essentially linked to the versatility of plasma functionalization and coating techniques to produce tailored surface properties. Plasmas have been explored as methods to sort and tailor MWNT morphologies as well, in an effort to produce ideal aligned arrays for improved performance as field-emission materials [Zhang et al., 2011b, Mathur et al., 2012]. Interactions based on plasma-surface chemistry are fairly well understood, although no work has been reported on the effect of strong electric fields on MWNT degradation in low-pressure plasmas. Of importance to the present work, direct exposure to glow discharges has been shown to allow for relatively tight length control of MWNT arrays by oxidative degradation [Zhang et al., 2011b] as well as both introduction of MWNT defects [Mathur et al., 2012, Koh et al., 2013] and ame-

lioration of defects [Wang et al., 2012, Kim et al., 2013].

5.3 Methods

From previous studies it was found that exposure to a low pressure glow discharge caused significant degradation of MWNTs, but the mechanisms of degradation were unclear [Vandsburger et al., 2013a]. Specifically, the respective roles of ion bombardment, plasma surface reactions, and electron bombardment/resistive thermal degradation, were not readily apparent. To that end, the experiments reported in this study were designed to identify the mechanism of degradation of MWNTs caused by electron current, by subjecting MWNTs to electron bombardment from a radio-frequency (RF) discharge afterglow.

Samples for the experiments consisted of a MWNT-covered stainless steel mesh composite material, produced by thermal chemical vapour deposition (t-CVD). The method produces dense MWNT forests that are in direct electrical contact with the stainless steel surface beneath [Baddour et al., 2009]. This aspect of the material was exploited to produce a MWNT-composite anode connected via a DC feedthrough to a 650 W AMETEK G850 DC power supply.

Using the setup described in prior work, a capacitively coupled RF glow discharge (13.56 MHz continuous wave) was used as a source of electrons and reactive species [Vandsburger et al., 2013a]. The plasma power was set at 30 W and the chamber pressure at 0.75 Torr, with a gas flow rate of 5 sccm. Ar, O_2, and N_2 were each used as the plasma gas at various stages of the work. The vacuum chamber was equipped with a rotary mechanical pump backing a separate molecular drag pump, operated in tandem as a two stage vacuum system. The base pressure for each stage was 5-6 mTorr and 4×10^{-6} torr, respectively. The experimental setup was designed to collect data aimed

at understanding the species produced by MWNT degradation, as well as to observe the morphological changes associated with it. To identify the equilibrium products of degradation, organic vapours produced during experiments were condensed onto compressed carbon pellets using a cold finger cooled to -80°C by dry ice. The pellets were subsequently degassed in a sealed vial and the gas was sampled and analyzed by a gas chromatograph − mass spectrometer (GC-MS). Plasma-produced excited species and transient species were measured by time-resolved optical emission spectroscopy (OES). The progression of MWNT degradation was revealed in images taken in the scanning electron microscope (SEM), which is also used to show the morphological changes induced by electron bombardment. Raman spectra were collected at positions corresponding to those used for SEM images. These cannot be confirmed to be identical to the locations shown in Fig. 5.1, but they were collected using the same samples, as well as from other samples that had undergone identical RF-afterglow discharge treatment. Raman spectra were produced by laser excitation at 754 nm and 50 mW. They were collected for an integration time of 80 sec with 3 coadditions per spectrum, and were adjusted to remove cosmic spikes and were fitted to a baseline. Each sampling position was measured in three lateral locations to control for possible non-uniformity in the MWNT forest layer and in electron bombardment.

During experiments, MWNT-covered stainless steel mesh samples were connected to the DC feedthrough and positively biased. The polarity was selected to recruit electrons and induce electron bombardment of the outer edges of the MWNT forest. Samples were placed in the afterglow region of the capacitively coupled radio-frequency glow discharge, to avoid exposure to the high density of reactive species that are found in the discharge. Placing the sample in the afterglow allowed for the isolation of the effect of electron bombardment on MWNT degradation and to reduce the impact of plasma-surface interaction. The magnitude of the positive bias was set at +200 V_{DC}, to

produce a net electron bombardment current of 5 mA, corresponding to a surface electron flux of $6.7 - 8.6$ A/m^2. Ultra high purity (UHP) oxygen plasma treatment provided information on plasma oxidation kinetics and both UHP oxygen and nitrogen gases were used to investigate the equilibrium products. By observing the species produced during oxidation, as well as the kinetics of the reactions in the plasma under oxygen limitation, OES data would corroborate the findings of GC-MS. In general, samples were treated for a total duration of one hour, after which the surface of the stainless steel substrate would be exposed. At this point a substantial fraction of the incident electrons would no longer interact with energized MWNTs.

Optical emission spectra were collected through a quartz window, placed at the centre of the glow discharge. To trace the development of species emission, particularly strong lines from each species were measured at a sampling period of 5 seconds. In these experiments, the procedure was determined to isolate the various contributions to the OES spectrum such as the RF glow, the effect of the bias, changes in the plasma chemistry and the background radiation. The background light in the chamber was measured first, followed by the ignition of the RF discharge. Six spectra were taken of the RF discharge, equivalent to 35 seconds, before the sample bias was applied. Six further spectra were collected with the bias applied. This approach provided information on the excited species produced by each of the steps without oxygen limitation.

The chamber was sealed 35 seconds after the bias was applied, to observe the kinetics of oxidation under oxygen limitation. The species of interest during carbon rich oxidation were identified from literature sources detailing the oxidation kinetics of 1,3-butadiene [Laskin et al., 2000]. These were chosen based on the findings of GC-MS analysis, and were also used as sources for curve-fitting of time-resolved intensity curves. OES measurements were concluded when the change in the intensity of the peak of interest approached zero, which typically occurred after approximately 20 minutes.

The spectral window of the spectrometer was 55 nm-wide at the highest resolution. As a result, spectral lines that were distant from each other could not be observed simultaneously. To control for non-uniformity in degradation rates over time, each spectral emission line was observed in a separate experiment with an untested sample, following the same procedure. Emission spectra were measured for multiple characteristic wavelengths from each species, to control for the effect of non-uniformities in the instrumentation and reactor window.

5.4 Results

5.4.1 MWNT Morphology

Morphological information was collected by examining the progression of MWNT degradation on samples after electron bombardment for a total duration of 60 minutes in O_2 plasma. It was found that the MWNT forest was degraded most severely in the region closest to the RF glow discharge, causing a distinct transition region to develop between the unaffected MWNT surface farthest from the glow and the region most strongly affected by electron bombardment. By imaging the sample in the SEM at regularly spaced intervals of distance between these extremes, information was collected to show an effect analogous to measuring the same region at regular intervals of time [Vandsburger et al., 2013a].

The five images shown in Fig. 5.1 are arranged in order of increasing electron bombardment intensity (A-E). They show the effect of electron bombardment strength, and in this way also show the temporal progression of MWNT degradation and the morphological changes associated with electron bombardment-induced MWNT degradation. The figure shows that degradation proceeds from the tips of the MWNTs and progressively shortens the forest to the point that it is negligible. In addition, the morphol-

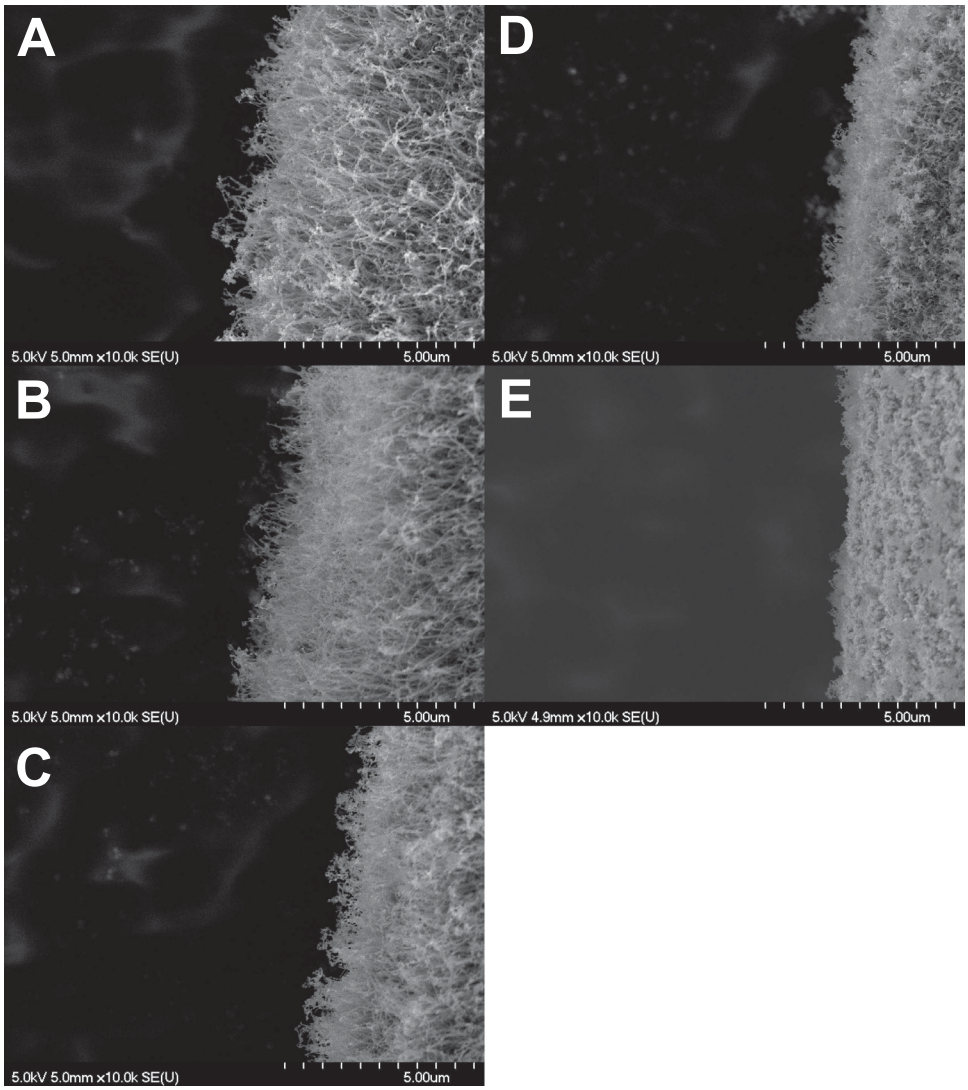

Figure 5.1: SEM images showing degradation that occurred during electron bombardment. Images presented in alphabetical order corresponding to increasing progress of degradation.

ogy of the MWNTs that make up the forest is seemingly unaffected by the degradation that occurs at their outermost edges. What is seen is a uniform reduction in average MWNT length, without the development of defect induced morphological changes that typically occur during RF plasma functionalization. The absence, in SEM images, of oxidation-induced curvature or morphology change in the entangled MWNT forest structure serves to indicate that the observed degradation is caused by electron impact that is restricted to the region nearest the tips of the MWNTs.

It has been shown that the carbon nanotubes produced by the t-CVD method are MWNTs [Baddour et al., 2009], with many concentric walls, making it likely that most of the MWNTs making up the MWNT forest structure are electrically conductive [Charlier and Issi, 1998]. Electrons that are accelerated to the surface are directed to isolated points on the MWNT surface by the concentration of the electric field that occurs on conductive nanostructured surfaces. In the case of vertically-aligned and entangled MWNT forests, is has been found that both the tips and the side-walls of conductive MWNTs can act as field enhancement points [Wang et al., 2002]. The effect of electric field-induced concentration of electron bombardment is to localize the energy transfer from incident electrons. Electrons that are attracted to and absorbed by the tips of MWNTs must rapidly decelerate in response to the increased resistivity of the MWNT, causing a transfer of energy into the MWNT lattice and a subsequent transformation of kinetic energy into thermal and chemical energy. This is in addition to the transfer of energy corresponding to the work function of the MWNT material that is part of the process of electron absorption. It is this concentration of energy transfer at the MWNT-tip that leads to tip-localized degradation.

It has been shown in literature that electrical current can induce resistive heating that is sufficient to cause thermal failure in field emitter applications [Bonard et al., 2003]. MWNT restructuring has been observed in SEM during field-emission experiments us-

ing MWNT forest samples [Ho et al., 2001]. The energy imparted by emitted electrons, as well as resistive heating caused by emitter current, can cause heating throughout the lengths of field-emitting carbon nanotubes giving rise to a destabilization of the molecular structure near the emitter-tip [Dionne et al., 2009]. The change in MWNT morphology that accompanies junction formation can be considered to be an effect of field-emission. The absence of visible junction formation in favour of the development of a disordered surface layer in Fig. 5.1 implies that the energy required to cause restructuring is restricted to the tips of MWNTs. These findings indicate that degradation is localized at the tips of MWNT anodes, but by a thermal effect, in light of the absence in these experiments of both field emission and ion bombardment.

The type and quality of MWNTs present in the MWNTs-covered stainless steel mesh samples dictate the extent of electron bombardment induced-degradation, through their effect on MWNT conductivity and current-carrying capacity. The conductivity of each metallic wall will add to the total conductivity of the MWNT, making more metallic MWNTs capable of absorbing higher electron bombardment flux. The higher resistance of semi-conducting MWNTS causes a higher transfer of energy from incident electrons at the point of absorption. This, in turn, leads to a tip-localization of bombardment-induced degradation. MWNT lattice defects have an adverse effect on electron conductivity in MWNTs, by disrupting the regular sp^2 hybridized carbon molecular structure. The MWNTs produced by the t-CVD method have a high concentration of lattice defects, which helps support the hypothesis that tip-localization of degradation is connected to defects in the MWNT structure. SEM imaging cannot be used to assess the concentration of defects, or the effect of bombardment degradation on defect content.

5.4.2 MWNT molecular structure

Raman measurements provided important evidence to demonstrate that degradation is localized to the tips of the MWNTs, without concurrent modification of the MWNT molecular structure. The spectra shown in Fig. 5.2 were collected at positions corresponding to the SEM images in Fig. 5.1, and are labeled accordingly. The spectra in Fig. 5.2 are presented without magnification to compare their relative intensities. These spectra are typical of MWNTs grown by CVD [Sveningsson et al., 2001, Liu et al., 2003], and show strong D, G and 2D peaks. In spectra A and B the radial breathing modes (labeled *"RBM"*) are visible as well. The peaks of the radial breathing mode are sensitive to diameter of MWNTs, so the peaks in A and B are likely from inner-shells. The intensity of the Raman signal is closely correlated to the length of MWNTs as seen in SEM images, showing a steady decrease with reduction in MWNT length. Raman signal intensity from MWNTs is sensitive to many factors, such as lattice chirality and MWNT diameter, so the effects of these factors were minimized by keeping laser parameters constant and measuring samples repeatedly. After correcting for the other effects, the change in Raman signal intensity from A-E can be attributed to the degradation of MWNTs on the surface, which helps to confirm the correlation with CNT length shortening.

Raman spectra also provide information on the chemical structure of MWNTs, by comparing the relative intensities of the principal peaks. The ratio of the intensities of the D and G peaks can give an indication of the ideality of the MWNT graphitic lattice. The D/G ratio cannot be used as a direct indicator of MWNT diameter, but is applicable to differentiate between double-walled and many-walled MWNTs. Because it reflects the presence of defects in the MWNT walls, the D/G ratio is proportional to the number of concentric walls in MWNTs. The effect of electron bombardment on

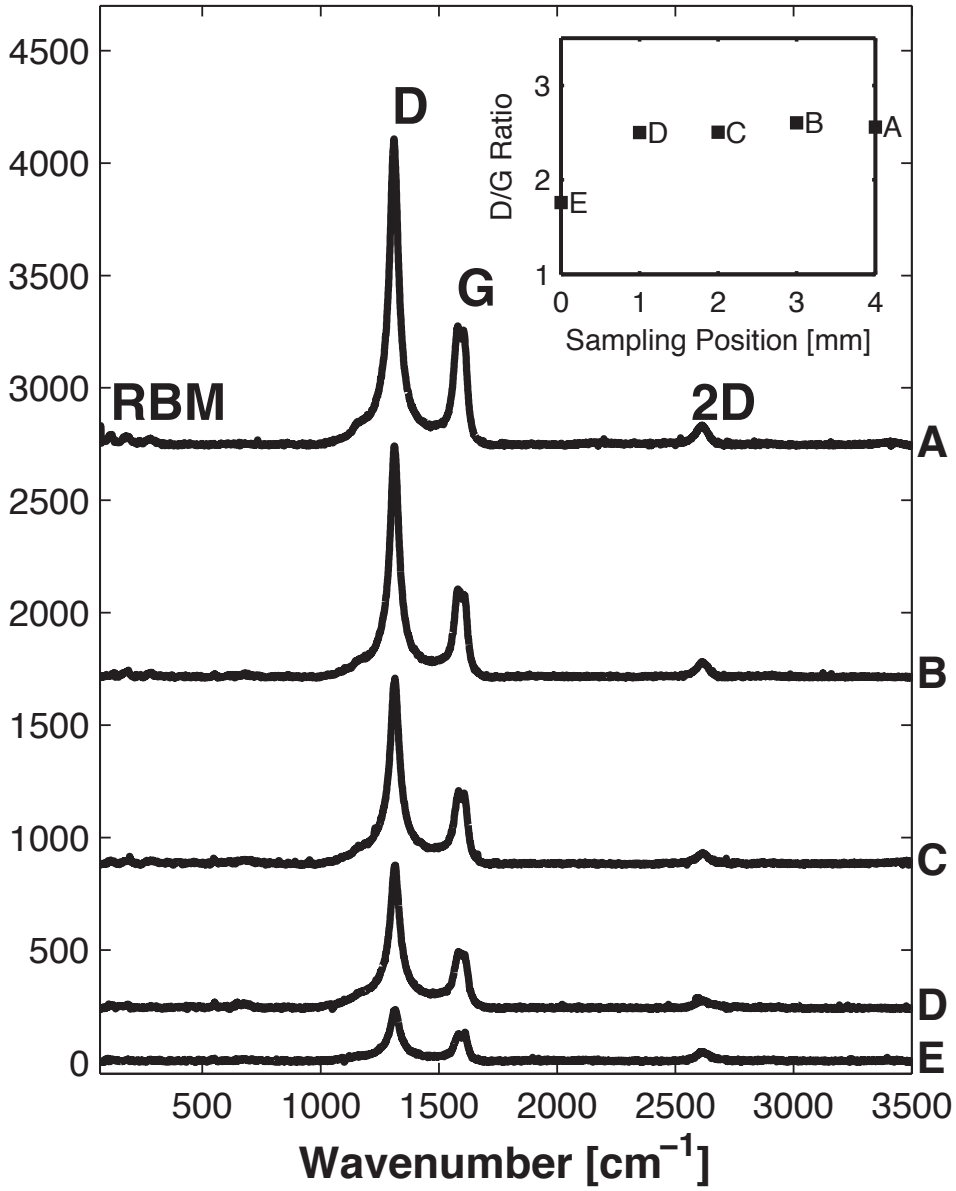

Figure 5.2: Raman spectra of the MWNT-covered stainless steel sample *post*-RF afterglow discharge treatment. Spectra **A-E** correspond to the same positions as imaged in **A-E** of Fig. 5.1. **Inset:** Average D/G ratios for each sampling position.

lattice ideality, and thus MWNT molecular structure, can be traced by observing the changes in the D/G ratio as a function of electron bombardment intensity. The average ratio of the D/G peaks were calculated from three measurements at laterally separated points for each sampling position. These values are shown in the inset in Fig. 5.2. With the exception of the final sample position, the average D/G ratios have consistent values of approximately 2.55. In the final spectrum (E) the average D/G ratio is lower, at approximately 1.75. The exact values are given in Table 5.1.

Table 5.1: List of Average D/G Ratios from Raman Spectra

Spectrum	**D/G**
A	2.56
B	2.61
C	2.51
D	2.50
E	1.76

The D/G ratios for spectra A-D show that the MWNTs that make up the forest layer are unaffected by the tip-localized electron bombardment. Thermal graphitization would appear as a steady decrease in D/G, which is not observable [Park et al., 2013]. Chemical functionalization, which is the cause of degradation in direct plasma-MWNT interactions and in ion-bombardment[Vandsburger et al., 2013a] would increase the D/G ratio [Osswald et al., 2007, Natarajan et al., 2011]. This is also not observable in Fig. 5.2. The lower average D/G ratio in spectrum E is understandable, considering the appearance of the sample surface at the same sampling distance in Fig. 5.1 E. The MWNT forest layer appears to have been degraded extensively at the position where spectrum E was collected, so the deviation from the other D/G values is attributable to

this diminished presence of MWNTs.

5.4.3 Equilibrium products

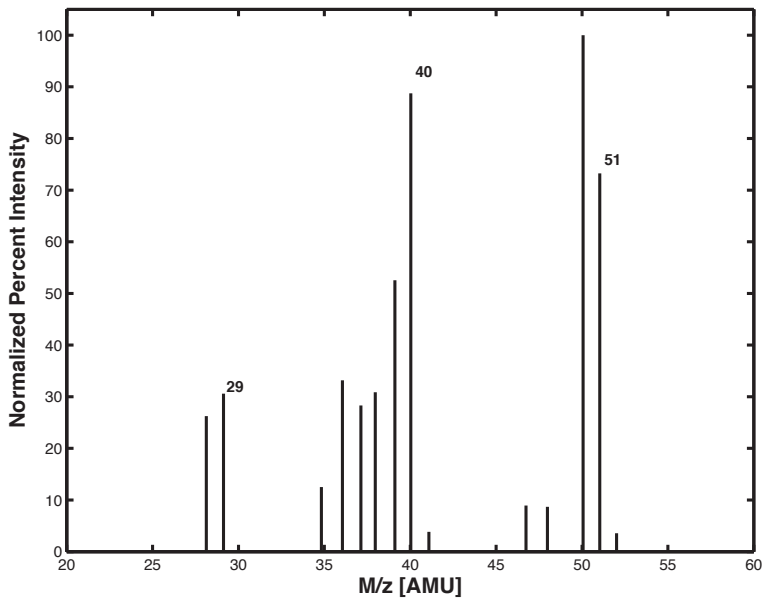

Figure 5.3: Mass spectrum showing ion fragmentation patterns attributed to propyne (m/z 40) and butadiyne (m/z 51)

The chemical species produced during MWNT degradation were expected to be short, unsaturated hydrocarbons, produced by thermal evaporation of MWNTs. MWNTs being composed of sp^2 hybridized carbon, thermal degradation would necessarily produce unsaturated or aromatic fragments. Based on the prevalence of unsaturated bonds in CNT chemistry, thermal degradation would likely produce unsaturated carbon fragments. Organic vapours produced during electron bombardment tests in Ar and N_2 plasmas were condensed and tested in a headspace analyzer - GC-MS. Inert gases were used to reduce the effect of oxidative plasma reactions that would alter the composition of the equilibrium products of degradation. A typical spectrum in the range of 0-60

AMU is presented in Fig. 5.3. Spectra taken in this region revealed patterns attributable to two parent ions at m/z of 52 and 40. These ions correspond to 1,3 butadiyne and propyne, both short and unsaturated hydrocarbons. Results from tests in N_2, Ar, and O_2 plasma treatments contained similar signals from propyne and its fragments, as well as 1,3 butadiyne.

Plasma processes that occur after degradation can have a significant effect on the composition of the degradation products prior to passing through the collection stage. However, the consistency in the GC-MS findings between both reactive and inert plasmas, as well as with predictions based on the chemical structure of MWNTs indicates that the species observed in the condensed equilibrium products are likely produced by degradation of MWNTs. These data also support the hypothesis that electron bombardment degradation is a thermal process, and not a chemical process, since the equilibrium products are insensitive to plasma composition.

5.4.4 Oxidation kinetics

The presence of CO_2 was detected in the equilibrium products collected during experiments, but its origin could not be determined. Understanding the source of CO_2, as well as the dynamic formation of carbon species, would help explain the range of carbonaceous species produced during MWNT-degradation. Studying the oxidation kinetics of MWNT degradation products under O_2 limitation granted the ability to trace the presence of small hydrocarbons that would not be detected downstream in the equilibrium products. The tendency of carbon vapour to form soot, for example, would limit the visibility of small carbon species in condensed samples. Most importantly, carbon monoxide is only produced under O_2 limitation, as in oxygen-rich conditions it oxidizes further to CO_2. Furthermore, while CO was easily observed in OES spectra, CO_2 was not. Sealing the chamber further improved the quality of the oxidation kinetics data

by allowing for the accumulation of oxidation products. Less reactive gases were initially explored for this purpose, but the OES spectrum of N_2 was found to obscure the characteristic lines intended for the observation of short hydrocarbons, like C_2 and C.

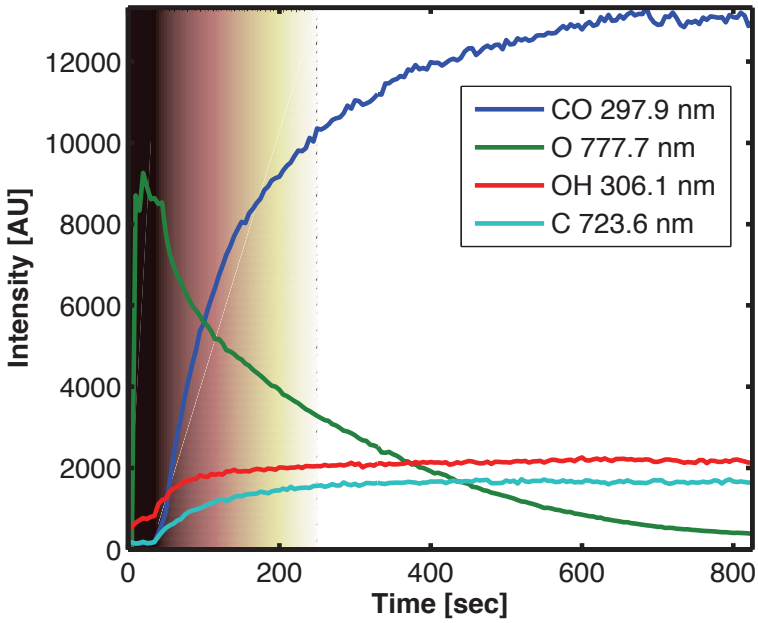

Figure 5.4: Optical emission spectroscopy data showing development of species lines during O_2 plasma treatment: Plasma power = 30 W, P_O = 0.75 Torr, V_{DC}=+200V (Shading is used to show the transition to oxygen limitation)

Fig. 5.4 shows the temporal development profiles for four important species present in the plasma during oxidation kinetics measurements. Each was taken in separate experiments, but reproduces the same trend. The figure highlights the dynamics of oxidation and the production of primary oxidation products. To show the timing of the sequence of steps discussed previously, the figure has been shaded in the leftmost section. The beginning of the gradient in the shading indicates the sealing of the chamber and the beginning of oxygen limitation. In oxygen-limited conditions, oxidation of hy-

drocarbons produces water vapour and carbon monoxide, as well as a large variety of other hydrocarbon species, which can aid in determining the nature of the hydrocarbon reactants. The curves in the figure show the increase in emission intensity from CO and OH and the decrease in emission intensity from atomic oxygen (777 nm) over the course of a 20 minute experiment. Optical emission from OH is used as an indicator of the presence of water vapour in the plasma. The initial period of the curves, where the emission intensity is stable, shows the baseline emission from the RF discharge and the effect of applying a bias to the sample. The change occurring at 35 seconds corresponds to the sealing of the chamber, signalling the beginning of oxygen limited oxidation. The shading corresponds to the decreasing oxygen concentration after the chamber has been sealed.

Considering, for the purpose of qualitative assessment, the emission intensity from each species to be proportional to its partial pressure in the plasma, the lines in fig(4) reveal important information about the products of MWNT degradation by electron bombardment. The intensity is proportional to electronic properties of the plasma as well. This will be discussed in detail as part of the analysis of reaction kinetics. The relative concentrations of OH to CO are good indicators of the type of hydrocarbons present in the plasma. Oxidation of a saturated hydrocarbon produces a ratio of n+1:n moles of H_2O:CO. Unsaturated hydrocarbons are oxidized into fewer moles of H_2O per mole of CO, and the ratio can be smaller than one. For example, oxidation of 1,3-butadiyne (C_4H_3) produces 3:8 moles H_2O:CO and propyne (C_3H_4) gives 2:3. These ratios are stoichiometric, since it is considered that atomic oxygen is available as a reactant. In Fig. 5.4 the emission intensity from CO grows much faster than for H_2O and the magnitude of the change is greater as well, which helps support the finding that the hydrocarbon from which the CO is produced is unsaturated.

The development of emission from lines attributed to atomic carbon also provides

important information to explain the correlation between the equilibrium condensed products and the species produced directly by MWNT degradation. The curves for atomic O and atomic C (723.6 nm) emission show a direct correlation, where the consumption of O accompanies a corresponding increase in emission intensity from atomic carbon. In the initial stages of the experiment emission from carbon is negligible, but after the chamber is sealed the intensity increases rapidly. As the emission from oxygen decreases, however, the rate of change in optical emission from atomic carbon also decreases.

Emission intensity is proportional to species concentration, or partial pressure. However, the electron density (n_e) and temperature (T_e) also have a strong influence on species emission intensity. Understandably, the composition of the plasma itself impacts both n_e and T_e, resulting in a degree of uncertainty about the reliability of the correlation between emission intensity and species partial pressure in the plasma. The significance of the dynamics in n_e and T_e has been addressed by injecting a trace amount of an inert gas into the plasma prior to oxidation. The intensity of characteristic lines from the inert gas over time will serve as a good compensation for instabilities in n_e and T_e. For this purpose, small concentrations of Ar and N_2 were included in the plasma gas for several experiments. N_2 was used, despite not being an inert gas, for it's low reactivity with unsaturated hydrocarbons relative to oxygen. Additionally, N_2 emits photons from several systems that are energetically close to spectral lines from CO and atomic carbon, whereas Ar does not emit as significantly in the near-UV range.

Emission intensity from inert gases depend entirely on n_e and T_e, but the choice of lines for comparison is important. Changes in the electron energy distribution may cause opposing changes in line intensity, depending on the discharge electron energy distribution function (EEDF), which is a function of T_e. To avoid errors in spectral correction, it is necessary to record the emission from a line that will respond to changes in

T_e and n_e in a similar way to the characteristic line being observed. Assuming that excitation by energy transfer between excited species is rare compared to electron impact excitation, selecting a line with a similar energy to the characteristic line of interest will minimize the effect of the EEDF. For that purpose, the Ar line at 750 nm was used to correct the intensity measurement of O at 777 nm. Similarly, the (0,0) line of the second positive system of N2 at 337.1 nm was used to correct readings of the CO $a^3\Pi$ (0,1) line from the third positive system, at 297.3 nm. The correction was done by taking the ratio of the spectrum of interest and the inert spectrum for the same experiment. The result was then normalized to help standardize the analysis.

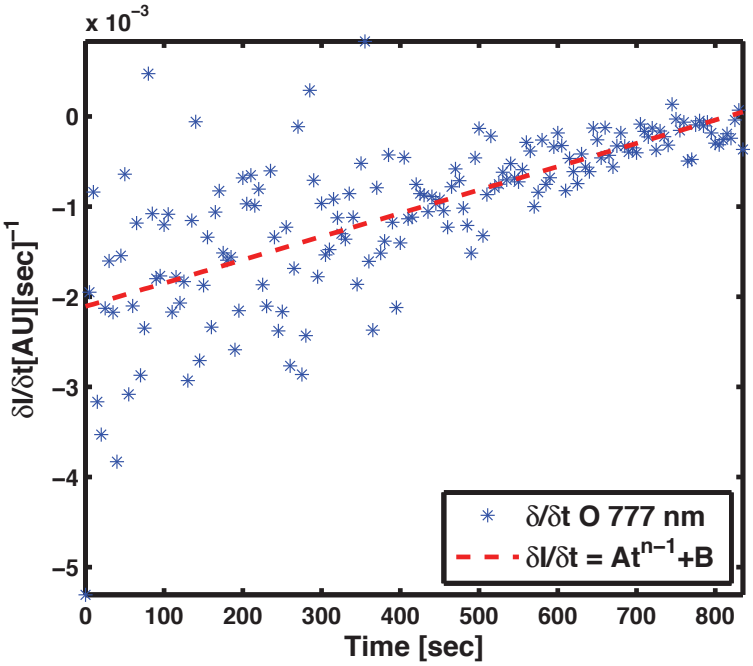

Figure 5.5: $\delta I/\delta t$ for the corrected intensity measurement of atomic oxygen (777 nm)

The information most sought from these experiments was an understanding of the reaction kinetics, in terms of reaction orders, in order to draw a conclusion about the form of the hydrocarbon feed. For this analysis the emission lines previously mentioned

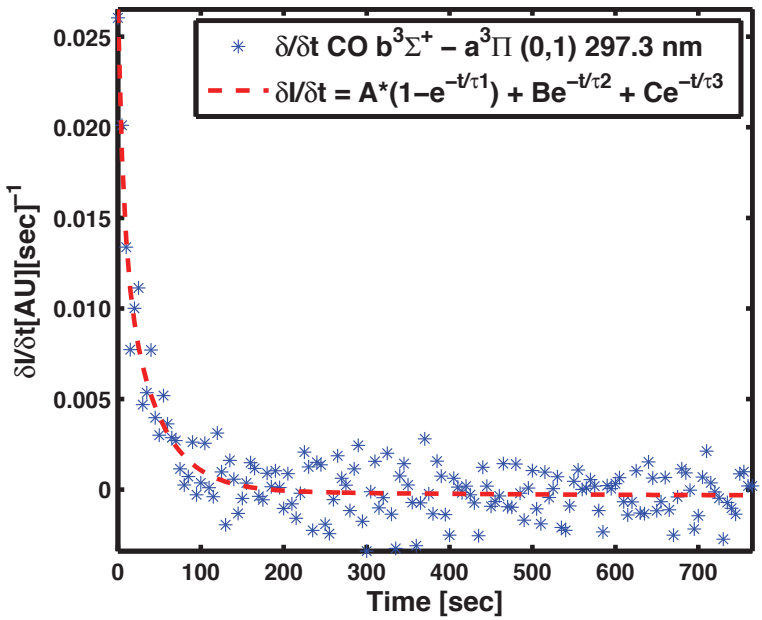

Figure 5.6: $\delta I/\delta t$ for the corrected intensity measurement of CO $b^3\Sigma^+$ - $a^3\Pi$ (0,1) line from the third positive system at 297.3 nm.

were deemed most relevant, and analysis focused on consumption of O and production of CO. Reaction rate models were developed using the first derivatives of the normalized and corrected intensities for each line, presented in Figs. 5.5 and 5.6. The rate of decrease in intensity from the O line at 777 nm was consistently negative and was fitted using a linear model. The slope of the model, however, was very small, as can be seen by the scale of the y-axis in the plot. The rate of increase of the CO line at 297.3 nm was fitted using a complex exponential function, which was taken from literature on oxygen-limited oxidation of butadiene. The rate model corresponds to the simultaneous production of CO from several carbon sources, C1-C3, and oxidation of CO to CO_2. The slope of the model drops below zero at approximately t = 235 sec, signalling a shift from net CO production to consumption.

Once fitted, the rate models were used to develop time-integrated models for emission line intensity. A fractional order model was selected for O, adapted from literature sources describing pyrolysis of hydrocarbons [Suuberg et al., 1989, Hurt and Haynes, 2005, Frank et al., 2010]. The plot of the fitted data is shown in Fig. 5.7. A fractional-order model helps describe the system of electron bombardment-induced MWNT degradation, in that it shows the concentration of hydrocarbon reactants to be almost entirely decoupled from the composition of the plasma. Unsaturated hydrocarbons are produced into the plasma by electron bombardment, which was tightly controlled during all experiments. For that reason, the consumption of atomic oxygen should almost not depend at all on the concentration of hydrocarbons in the system. A fractional order model helps to confirm that aspect of the hypothesis.

The time-integrated model for the corrected intensity of CO is a compound model comprising a second order reaction and a first order reaction. The plot of the fitted data is shown in Fig. 5.8. The model, having been assigned based on literature descriptions of the mechanism of unsaturated hydrocarbon oxidation [Dagaut and Cathonnet,

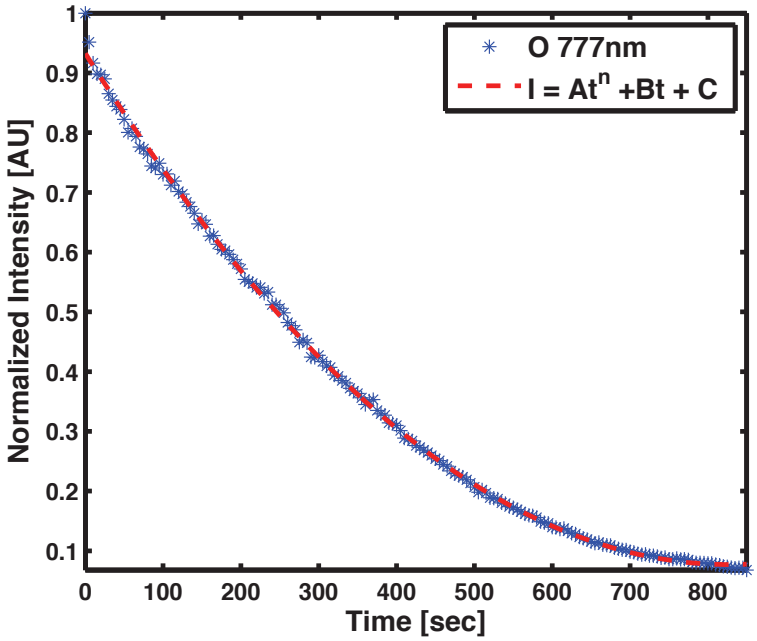

Figure 5.7: Corrected intensity measurement vs. time of atomic oxygen for the course of a twenty-minute experiment. Fractional order kinetics are typical of pyrolysis reactions where the hydrocarbon concentration is decoupled from the reaction rate.

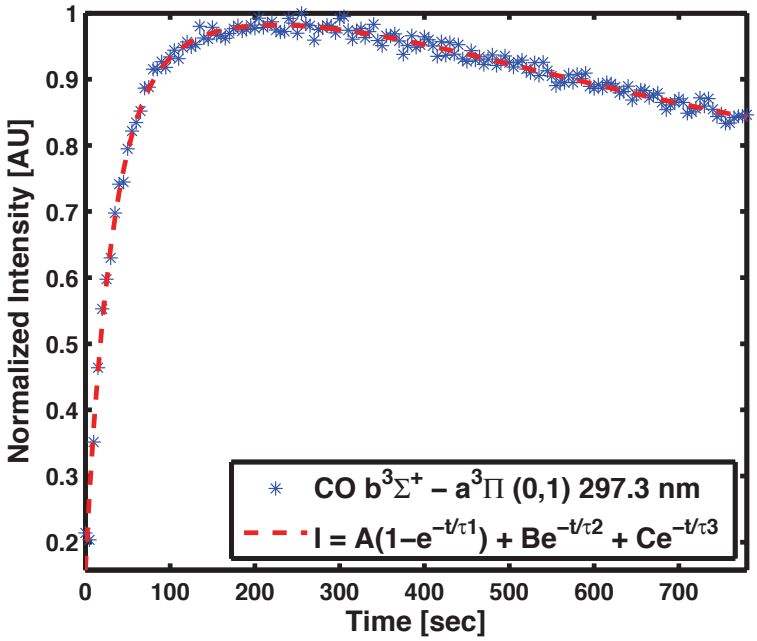

Figure 5.8: Corrected intensity measurement vs. time of CO $b^3\Sigma^+$ - $a^3\Pi$ (0,1) line from the third positive system at 297.3 nm. Transition from production to consumption corresponds to t = 250 sec.

1998, Hansen et al., 2009, Laskin et al., 2000] , reflects the initial production of CO during an oxygen-rich period and subsequent consumption. This trend has been observed frequently in literature, occurring as a result of both CO-CO collisions and oxidation by reaction between CO and O, CO and O_2, and in carbon recombination reactions [Brezinsky et al., 1985]. The similarity of the chosen model to models based on data for experiments where unsaturated hydrocarbons were oxidized directly helps confirm that the products of MWNT-degradation by electron bombardment are also unsaturated hydrocarbons.

5.5 Conclusions

Over a time-scale of approximately twenty minutes, significant degradation of MWNTs can be observed during electron bombardment by electrons recruited from a glow discharge, with complete removal after approximately one hour. The time scale is caused by electron bombardment, and is independent of gas composition. The same plasma that is used as an electron source can also by used to observe active species produced by the degradation process, as well as the subsequent plasma chemical reactions that occur in the gas phase. By studying both the dynamics and the equilibrium products of MWNT degradation during electron bombardment, important information has been gathered to explain both the nature of the degradation products and the effects of plasma kinetics and plasma composition on the degradation process. Equilibrium measurements of condensed species showed both C_3 and C_4 unsaturated hydrocarbons, propyne and butadiyne, which were later confirmed by time-resolved OES spectroscopy.

The findings of this work present a promising opportunity for the development of CNT plasma-polymer composites. Work on plasma processing of short, unsaturated hydrocarbons has been found to develop heavier hydrocarbons that can be used for in-situ

plasma polymer synthesis and deposition [Thejaswini et al., 2011]. Taking advantage of the unique synthesis mechanism that produces MWNTs in direct electrical contact with a stainless steel substrate, this topic is currently the focus of an effort to develop MWNT-polymer composite electrodes.

5.6 Acknowledgements

The authors gratefully acknowledge the financial support provided by the Natural Sciences and Engineering Research Council of Canada and the Fonds de recherche du Québec - Nature et technologies. The authors also acknowledge the expertise of Mr. Ranjan Roy in operating the GC-MS instrument.

CHAPTER 6

STUDY OF GAS-PHASE PLASMA REACTIONS DURING ELECTRON BOMBARDMENT OF MWNTS

Preface

The work presented in this chapter has been accepted for publication in the journal, *Plasma Processes and Polymers*. The work was planned, executed, and analyzed by L. Vandsburger. Research supervision and reviewing of the manuscript were the shared responsibilities of the two academic advisors, S. Coulombe and J.L. Meunier.

It contains the results of a study of the gas phase plasma polymerization and subsequent surface deposition of plasma-polymer films. The study builds on the findings of the previous chapter by investigating the effect of plasma composition on plasma polymerization reactions. This constitutes a significant development in MWNT-polymer composite research, as well as in MWNT-plasma interaction in the presence of strong electric fields.

The composition of the films offers great promise for development of conductive polymer film coatings on MWNTS, since the plasma polymer films were found to contain numerous conductive poly-cyclic aromatic hydrocarbons. Species such as pyrrole, pyridine, polypyrrole, acridine, and carbazole were detected in MS spectra and in OAS measurements. The production of plasma polymer coatings on MWNTS was confirmed by FTIR-GIR measurements, as described in Chapter 3.

Carbon nanotube-polypyrrole composite electrode materials produced in situ by electron bombardment in radio frequency plasma afterglows

L. Vandsburger, S. Coulombe, J.-L. Meunier

Plasma Processing Laboratory, McGill University, Department of Chemical Engineering, M.H. Wong Building, 3610 rue University, Montreal, Quebec, H3A 0C5

6.1 abstract

Free electrons, produced in radio-frequency (13.56 MHz) glow discharges of O_2, N_2, and Ar, are recruited to multi-walled carbon nanotubes (MWNTs) by a positive electric field. Electron bombardment degradation is restricted to the tips of the MWNTs. SEM images show that a surface deposited layer develops during degradation. Gas phase plasma reactions form polycyclic aromatic hydrocarbons and plasma polymers, which are re-deposited on the MWNTs as thin films. The plasma polymer is identified as a polypyrrole (Ppy)-like plasma polymer, as shown by molecular optical absorption spectroscopy and GC-MS. FT-IR spectra confirm that the surface films are composed of the same plasma polymer. Inert gas plasmas produce higher-molecular weight plasma polymers, while O_2 plasma treatments produce over-oxidized polypyrrole films.

6.2 Introduction and Background

Carbon nanotube - electrically conductive polymer (CNT-ECP) composites are promising new materials, for their potential application in numerous types of devices and reinforced conductive polymers [Jeyabharathi et al., 2010, Marega et al., 2012, Huyen et al., 2012]. These include exciting alternatives to current neural interface devices, which present distinct issues with biocompatibility [Chen et al., 2011b, Jan et al., 2009, Green et al., 2008]. Work on their preparation, however, has thus far focused on wet chemical

means [Wu et al., 2005, Zelikman et al., 2008, Zhang et al., 2011a, Shigi et al., 2002, Nguyen and Shim, 2011, Ghatak et al., 2011]. The drawbacks of these methods are numerous, and include dispersing CNTs into a liquid polymer medium, ensuring uniformity of any coating process, and limiting agglomeration and settling of CNTs during synthesis. Also important, considering the intended application in electrode devices, is creating a good electrical contact between a deposited CNT-polymer composite layer and a metal electrode substrate beneath. This has been done previously by spreading a CNT suspension onto a thin gold film or onto a platinum tip, which inevitably introduces an interfacial resistance between the coating and metal surface that increases the power requirements of the device.

Gas phase plasma chemistry offers an alternative method for producing conductive polymer thin films. Plasma surface functionalization/coating of CNTs serves the dual purpose of stabilizing CNT dispersions in polymer solutions [Vandsburger et al., 2009, Hordy et al., 2013], which further improves incorporation of CNTs into composites for applications such as field induced polymer electroluminescent devices [Chen et al., 2013]. Surface functionalization takes advantage of the structure of multi-walled carbon nanotubes (MWNT) by adding functionalities to the outer layer, while the inner layers are maintained intact for optimal transport properties. Work on plasma polymerization in inert and reactive plasmas has reported the synthesis of polycyclic aromatic hydrocarbons (PAHs) and other plasma polymers directly from both saturated and unsaturated hydrocarbons of mass below C_6 [Shih et al., 2005, Guo et al., 2006, Thejaswini et al., 2011, De Bleecker et al., 2006, Benedikt, 2010]. Work in this area was directed at explaining other phenomena rather than producing plasma polymer films. Nonetheless, the findings clearly showed a plasma synthesis mechanism that produced higher molecular weight cyclical molecules during plasma treatments. The synthesis of pyrrole and other amide molecules by plasma cyclization of unsaturated hydrocarbons has

been known for some time [Suhr, 1972, Tsukamoto and Lichtin, 1960]. Addition of oxygen inhibited this mechanism in experiments that were undertaken in excess oxygen [Shih et al., 2005]. The inhibition was explained by reactive oxidation of carbon rings into CO and CO_2. Findings have shown that CNT failure during field emission can be caused by electron current [Wang et al., 2002], leading to evaporation and structural failure. Following these results, this report looks at electron bombardment degradation as means of providing one-step, targeted functionalization/coating of CNT surfaces.

6.3 Methods

6.3.1 Sample Preparation

The following work describes a simple method to produce CNT-ECP composites, without any wet chemical treatment, by taking advantage of a unique synthesis method that produces MWNT layers in native electrical contact with a metal subtrate. Entangled MWNT forests have been grown by thermal chemical vapor deposition (t-CVD) directly from the surface of 400 mesh-size stainless steel meshes [Baddour et al., 2009]. This method produces MWNTs with many walls and a high density of lattice defects, which is highly suitable for functionalization in glow discharge plasmas [Vandsburger et al., 2013a,b].

6.3.2 Plasma System

After synthesis, the MWNT-covered stainless steel mesh samples have been treated in the afterglow region of a capacitively coupled radio-frequency glow discharge (RF, 13.56 MHz continuous wave). The setup consisted of a cylindrical vacuum chamber equipped with quartz windows to allow optical absorption spectroscopy (OAS) at the sample location. Prior to experiments, the chamber was evacuated to a base pressure

of 4 μTorr using a turbomolecular pump backed by a two-stage rotary vane pump. The complete setup is described in more detail in a previously published report [Vandsburger et al., 2013a]. The chamber pressure was set at 0.75 Torr and the flowrate of ultra-high-purity (UHP, 99.999%) O_2, Ar, or N_2 at 5 sccm. MWNT covered stainless steel mesh samples were positioned within the plasma afterglow. The RF power was 30 W for all tests. Langmuir probe measurements confirmed that active species, such as ions and electrons, were present at the sample position. Also, even though the plasma gas used in experiments was UHP, atomic emission spectra of the glow discharge indicated trace nitrogen and water vapor impurities are present in the treatment chamber[Vandsburger et al., 2013a].

6.3.3 Electron Bombardment

The samples were biased at +200 V_{DC}, except for tests in Ar for which the bias was set at +75 V_{DC}, in order to produce a total electron bombardment current between 4-5 mA. The electron bombardment flux corresponded to a current density of $6.7 - 8.6$ A/m^2 on the planar mesh area that was affected by the bombardment. All electron bombardment degradation/plasma polymerization experiments were undertaken for a total of 60 min.

6.3.4 Analytical Techniques

During experiments, condensable vapors were collected near the exhaust of the vacuum chamber using compressed carbon pellets cooled externally by dry ice to approximately -80 ^{o}C. This technique has been shown to be effective at collecting pyrrole and pyrrolic compounds downstream of a glow-discharge [Tsukamoto and Lichtin, 1960], and has been used previously to collect PAH products of MWNT degradation [Vandsburger et al., 2013a]. FT-IR transmission/absorption measurements were recorded using a Bruker 2000 IR microscope in transmission mode. IR light was passed through the

mesh sample with a sampling area of 250 μm^2. The instrument had a resolution of 3 cm^-1 and a spectral range from 750 cm^{-1} – 4000 cm^{-1}. Each spectrum was collected as the sum of 200 scans. Background spectra were collected in the same way. All spectra were adjusted to correct for baseline curvature and smoothed automatically. A background spectrum was collected using a bare stainless steel mesh to eliminate the effect of the substrate beneath the CNTs. Atmospheric compensation during background removal also removed the signatures of water vapor and carbon dioxide.

6.4 Results and Discussion

Samples were examined using a scanning electron microscope (SEM) to collect morphological information on the degraded CNT-stainless steel samples. A series of images was taken on treated samples progressing from relatively unaffected areas toward the edge nearest the RF antenna. The sequence corresponds to a survey of the sample from the regions of low to high electron bombardment intensity. This technique has been described in more detail in a previously published report, showing the gradient of afterglow intensity [Vandsburger et al., 2013a]. The development of the degradation is detailed by taking images at intervals of 1 mm on the surface of the mesh. This provides insight similar to collecting images at one location for increasing treatment duration. The series of images in **Figure 4.3** indicate clearly that the degradation reaction occurs predominantly at the outer surface of the CNT forest, progressively shortening the CNTs. Deposits can be seen to form on the remaining CNTs, beginning with individual CNTs in the first image and forming a visible film in the final image.

The process of electron bombardment degradation differs from oxygen ion bombardment degradation in the development of these deposits. Surface oxidation by ion bombardment did not lead to the accumulation of surface deposits, even to the point that

the MWNT layer was completely removed [Vandsburger et al., 2013a]. For this reason, it is unlikely that oxidation is responsible for the development of the disordered surface film in these images, since the positive bias on the sample repelled the like-charged oxygen ions in the RF-afterglow.

Some degree of degradation of MWNTs occurs in all plasma modification processes, typically at locations of high surface energy such as lattice defects or other strained regions [Zhang et al., 2011a]. The images in Figure 4.3 concur with previously published images [Vandsburger et al., 2013b], and show that the reaction is essentially restricted to the outermost surfaces of the CNT forest. In substrate-bonded MWNTs, the electric field concentrates at the MWNT tips at strengths on the order of 0.1-1 V/nm [Wang et al., 2002, Huang et al., 2005, Jung et al., 2007, Zou et al., 2010]. The tip-down degradation process helps to demonstrate that the CNTs are in strong electrical contact with the stainless steel substrate since the DC bias is applied to the metal substrate beneath, rather than to the CNTs themselves. This verifies previously published work on the subject [Baddour et al., 2009, Hordy et al., 2013] and has considerable significance for the application of this material as an electrode. Strong electrical contact reduces the interfacial resistance between the metal surface and MWNTs that is unavoidable in solution-deposited coatings, which in turn has implications for power and voltage requirements during operation.

The chemical identity of the plasma polymer deposits was established using grazing angle FTIR spectroscopy. Spectra from MWNT samples taken before and after afterglow treatment in N_2 and O_2 are presented in Figure 6.2. The polypyrrolic plasma polymer (PPy-PP) coating is revealed by comparing the spectrum from the treated surfaces to the untreated surface, labeled CNTs. Most notably, the difference is seen in the peak at 3300 cm^{-1} that is absent in the untreated sample, as well as in the spectrum region located between 850 and 1800 cm^{-1}. This is magnified in Figure 6.3 showing

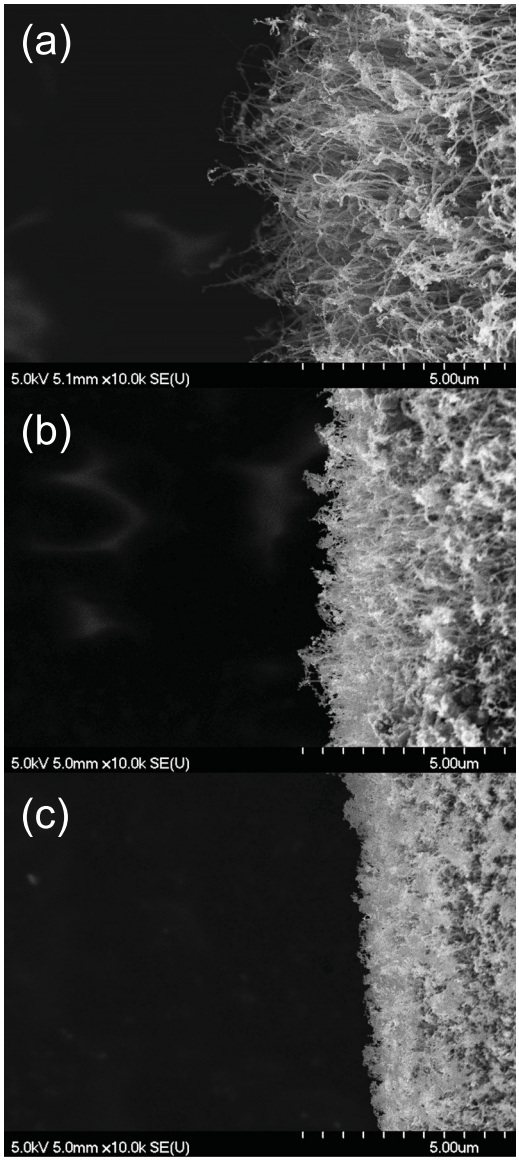

Figure 6.1: SEM images evidencing the processes of electron bombardment decomposition and thin film deposition by plasma polymerization. (a) shows an undamaged region of the sample, while (c) shows a region after significant degradation and surface deposit accumulation. Each image (a-c) shows a progressive decrease in the height of the CNT layer and a corresponding increase in the density of a deposited coating. Electron bombardment flux for images a-c is within the range of 6.7 - 8.6 A/m^2.

the so-called fingerprint region for both N_2 and O_2 tests, and compared to the native CNT signal. It is important to note that in the spectrum taken from an untreated sample, peaks seen in the 500-1080 cm^{-1} range are present in all samples. For this reason, the spectra in Figure 6.2 have been normalized to the intensity of the peak marked with an asterisk (*) to facilitate comparison.

Analysis of the peaks in Figure 6.2 show a strong effect of plasma gas composition, especially in the 3000-3550 cm^{-1} band, which has been labeled 3 in Figure 6.2. This band contains contributions from N-H and O-H groups for aromatic amines and for polypyrrole. Important N-H peaks for polypyrrole are 3100, 3350, 3400 and 3527 cm^{-1} [Lei et al., 1992, Lin and Wu, 2011]. These correspond to ring vibration and stretching, and a significant increase is seen at these wavenumbers between (a) and (b)-(c), even though the band is unresolved. The overlap in these peaks is a result of the PPy-PP being deposited as a film. Since this large band is sensitive to hydrogen bonding, the higher intensity seen in (c) is attributable to the presence of oxygen containing functional groups, such as isocyanate or hydroxyls. Correspondingly, a slight signature directly from isocyanate groups (C-N-O) at 2275 cm^{-1} is seen in Figure 6.2(c), but is not visible in (a) or (b) [Zhao et al., 2004]. This contributes to the finding that oxygen plasma treatment produces oxidation of amine bonds. The peak labeled 1 in Figure 6.2 is stronger in (c) than in the previous two spectra. This is the peak at 1080-1087 cm^{-1}, which corresponds to C-O stretching in cyclical molecules. This shows that oxygen plasmas lead to the development of oxygen groups in the deposited coating. The peaks between 500-1080 cm^{-1}, are mostly present in all three spectra and correspond to C-H and O-H stretches and adsorbed nitrogen from the atmosphere [Biniak et al., 1997]. These are seemingly unaffected by electron bombardment degradation, and are likely caused by adsorption of atmospheric gases.

The spectra in Figure 6.3 correspond closely to the specific peak signature of PPy

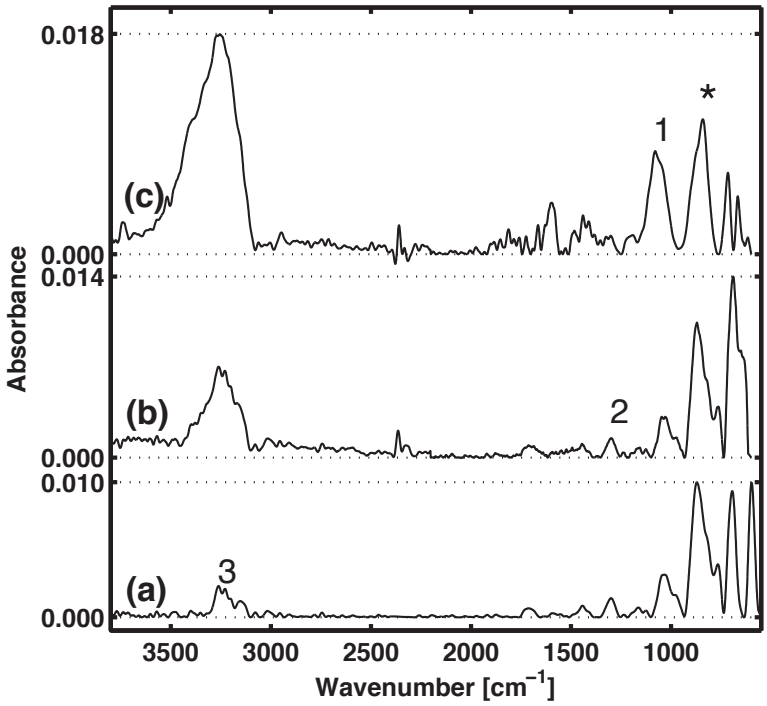

Figure 6.2: Grazing angle FTIR spectra collected from the untreated native MWNT layer and PPy-PP coated samples from N_2 and O_2 tests [Jeyabharathi et al., 2010].

[Lin and Wu, 2011, Sahoo et al., 2011, Menon et al., 1996]. This confirms that the plasma polymer is chemically identifiable with PPy and reveals the effect of plasma gas composition on the chemical structure of the deposited film. The spectrum taken from a sample treated in an O_2 plasma afterglow contains absorbance peaks specific to over-oxidized PPy-PP. Overoxidation occurs when an external driving force, in this case the energized constituents of the plasma afterglow, induces oxidation of a polymer [Li and Qian, 2000]. The signs of over-oxidation can be found in the fingerprint region, as well as in the entire spectrum. The peak at 1075 cm^{-1}, for example, is found in literature sources to result from PPy formed in oxidizing conditions [López et al., 2010]. The deposition of an aromatic coating is demonstrated by the peaks 1560 cm^{-1} and 1497 cm^{-1}, which relate to the symmetric and asymmetric aromatic ring stretching [Zhang et al., 2004]. These peaks are present in spectra from both N_2 and O_2 treated MWNT samples, but not in spectra from native MWNT samples. The peak at 1035 cm^{-1}, and the broad peak between 1150-1250 cm^{-1} are also attributed to C=C bending modes, which is convoluted with a peak at 1167 cm^{-1}, attributed to C-H in plane vibration in PPy. The presence of the same peak, although at lower intensity, in native MWNT spectra can be explained as absorption from defective outer shells of MWNTs. The peak labeled 2 in Figure 6.2 is important, as it corresponds to the N-H stretch in pyrrole. N-H stretches in aminated hydrocarbons are reported at many positions around 1300 cm^{-1}, and in spectra for untreated MWNT samples an N-H stretch was found at that location. In both N_2 and O_2 treated samples, there was a broader peak extending from approximately 1300-1375 cm^{-1}. Although the peaks are in a different position, they can nonetheless be identified as an N-H stretch in a PPy-like polymer [Lei et al., 1992, Zerbi et al., 1994, Bora and Dolui, 2012].

The formation of PPy is further confirmed by investigating the composition of the gas phase reaction products. Optical absorption spectroscopy (OAS) measurements per-

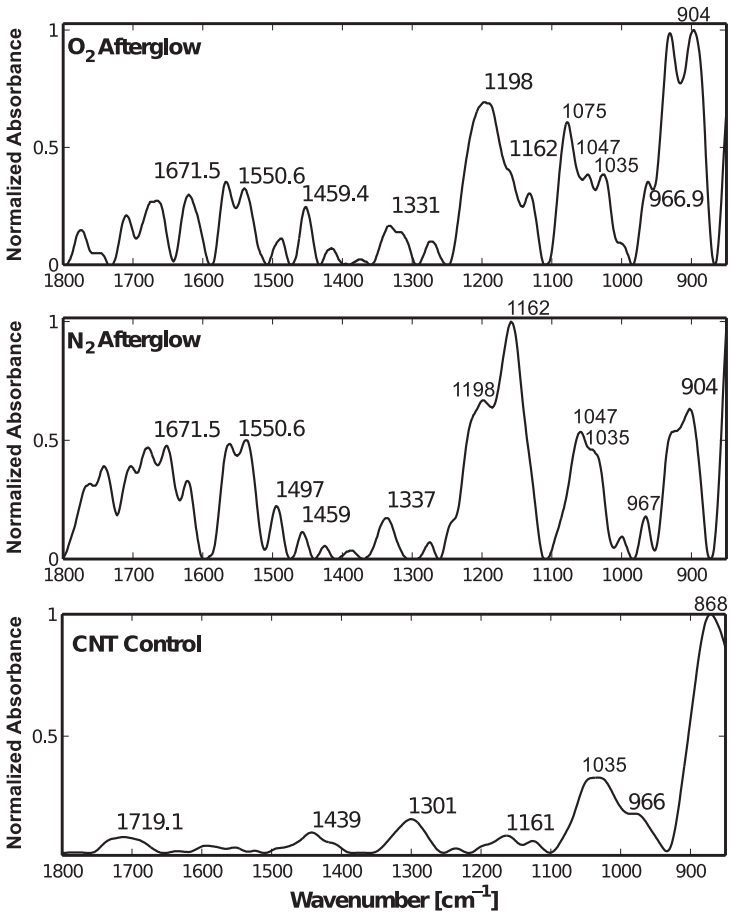

Figure 6.3: Spectra from a magnified section from treated samples showing the specific peak signature characteristic of PPy [López et al., 2010]. Peaks attributable to oxidized polypyrrole-plasma polymer are visible in FTIR spectra, indicating sensitivity to plasma gas composition.

formed near the surface of the sample show the characteristic shape of PPy, shown in Fig. 6.4 [Shigi et al., 2002]. Spectra show a large absorption band centered at 455 nm that develops quickly after the positive sample bias is applied. The effect of plasma composition is seen in the effect on an increasing absorbance tail towards longer wavelengths. Over–oxidized PPy absorbs broadly in the near infrared (NIR), while native PPy does not. This was seen clearly in Fig. 6.4, which showed spectra taken from experiments in all three plasma environments. The tests undertaken in N_2 and Ar show little or no increase in absorption at wavelengths above 570 nm, while the spectrum shown from an O_2 plasma afterglow experiment contains a marked absorption, increasing toward the NIR. This finding confirms that the oxidized plasma polymer identified in FTIR measurements originates in a gas phase plasma polymerization reaction. The peak marked by an asterisk (*) in the OAS spectra for N_2 and Ar was absent in O_2 tests. Judging by previously reported findings it is likely attributable to a polycyclic aromatic hydrocarbon (PAH) [Vandsburger et al., 2013a]. Identification of OAS peaks for PAHs is not trivial, but in this case, the chemistry of the system and the presence of PPy in a plasma polymerization reaction allows the attribution of this peak to acridine (molar mass 179), which has a single broad absorption band centred at 350 nm [Friedel and Orchin, 1951]. Formation of larger multi-ringed PAHs during plasma polymerization is characteristic of inert systems, and three ring PAHs have been found to be most prevalent in experiments on soot formation using benzene in inert plasmas [Shih et al., 2005]. The presence of PPy in spectra confirms that it is present in the gas phase around the sample, and that deposition occurs from the plasma onto the surface, but it does not give any information on the molecular weight of the plasma polymer or whether it is stable in the RF afterglow.

The number of small peaks in Figure 6.3 can be explained partially by the nature of plasma polymerization. Since plasma polymerization does not produce a consistent

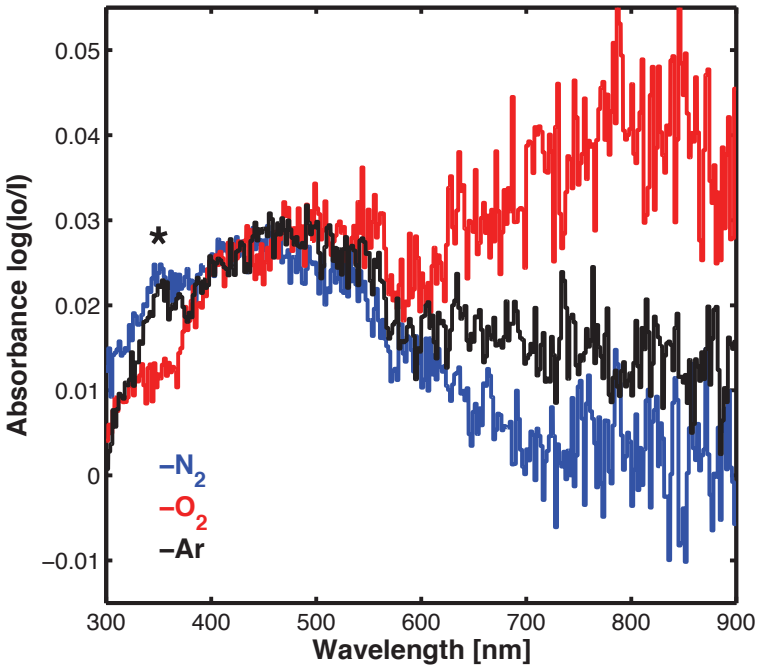

Figure 6.4: Optical absorption spectra taken in situ near the MWNT sample. The broad absorption band centered at 455 nm (A) is characteristic of PPy. The rising absorption between 600 and 900 nm indicates that the PPy-PP is over-oxidized.The peak marked with an asterisk (*) is identified as acridine.

molecular structure, the deposited coating will contain polymeric deposits with numerous different types of bonds [Zerbi et al., 1994]. As a result the spectra for N_2 and O_2 contain numerous small peaks that are not visible in the spectrum from native MWNT-covered stainless steel mesh samples. A list summarizing the important peaks in Figure 6.2 and Figure 6.3 is given in Table 6.1.

Table 6.1: Characteristic Peaks of PPy vs Experimentally Obtained Signals of PPy-PP (Condition column shows relative strength(S/M/W) and whether the peak is resolved (R/U))

Literature Values [cm^{-1}]	Bond Assignment	Experimental Values [cm^{-1}]	Condition
3527	N-H stretch in pyrrole	3525	W,R
3410	N-H vibration in the Pyrrole	3410	S, U
3100	C-H stretch in PPy	3100	S, U
3000-3500	N-H and O-H stretching	3080-3550	S, U
2275	C-N-O	2275	W, U
1540-1560, 1460	C=C stretch	1550, 1460	M,U
1497	C=C stretch	1497	W,R
1300-1330	C-N stretch	1331-1337	M, R
1167	C-H in plane	1162	S, R
1075	N-H in plane (oxidized)	1075	S,U
1035-1043	N-H in plane	1035-1043	S, U
908	C-H out of plane	904	S, R

Condensed samples of the volatile organic components produced in the plasma chamber were analyzed using a gas chromatograph - mass spectrometer (GC-MS). A characteristic spectrum from this analysis is shown in Figure 6.5. The spectrum in the inset is presented separately, because the maximum intensity at m/z = 50 amu is approximately an order of magnitude higher than for the larger ions. It contains peaks attributable to pyrrole itself, at a mass to charge ratio (m/z) of 67 amu, as well as its 2-5 monomer chain polymers at m/z of 130 amu through 329 amu in increments of 65-67 amu. The fragmentation pattern in the inset matches unsaturated alkynes, such as propyne (m/z 40 amu) and butadiyne (m/z 51 amu) [Guo et al., 2006]. Analysis of inert plasma reactions with unsaturated hydrocarbons has shown to produce similar molecules in literature, [Thejaswini et al., 2011, Consoli et al., 2008] from short hydrocarbons like C_2H_2. This is supported by the finding that the these species are the main products of electron bombardment degradation [Vandsburger et al., 2013b]. It thus seems likely that pyrrole synthesis occurs in the gas phase, as has been shown to occur in literature [Suhr, 1972]. Excited nitrogen species, present as trace impurities in the nearly pure O_2 RF afterglow, react with the short carbon chains to form terminal amine radicals, which can spontaneously form pyrrolidine or pyrrolic ring systems by radical cyclization [Suhr, 1972, Tsukamoto and Lichtin, 1960]. The source of the nitrogen impurities in oxygen plasma experiments can be attributed to gas molecules desorbed from the MWNTs as a result of electron bombardment and localized thermal heating, as has been shown in literature [Hata et al., 2001, Saito et al., 2002, Dean and Chalamala, 2000].

The effect of plasma composition is visible in GC-MS data, as well. Figure 6.6 presents a set of four mass spectra corresponding to a set of standards from the NIST and a characteristic spectrum from experiments in each of the plasma gases investigated. The standard peaks were selected to aid in comparison of the spectra, based on the

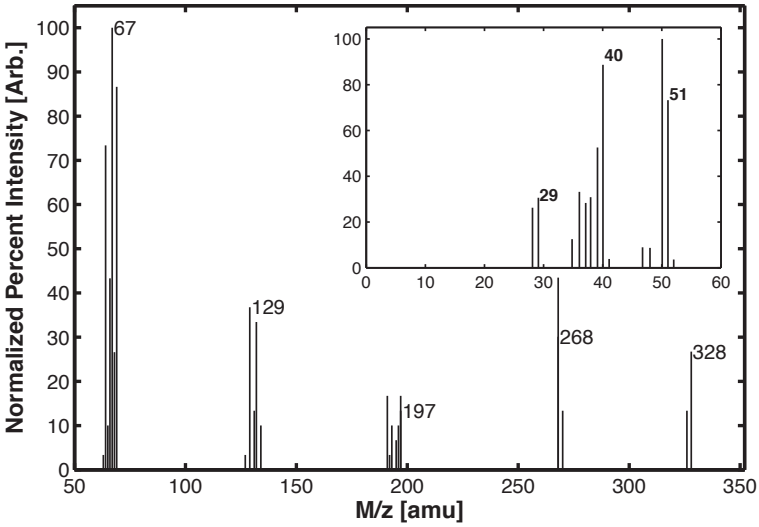

Figure 6.5: Mass spectrum of condensed organic vapor from a RF N_2 afterglow experiment of 60 min duration. The labeled peaks are all identifiable as pyrrole (m/z = 67), or its polymer (up to five lengths). The fragments are grouped around these peaks, showing that some plasma modification has occurred. The inset (approx. 10X the intensity of the main plot) shows the fragmentation patterns of unsaturated alkynes, matching butadiyne and propyne, at parent ion masses of m/z = 40 and 51 amu[Guo et al., 2006], detected in large quantities in the equilibrium products of the plasma gas.

species found in previously detailed analyses and in literature. The peaks in the standard are, in order from left to right, pyrrole, pyridine, aniline, quinoline, bipyridine, and acridine. Table 6.2 lists the molecular weights and chemical structures of each of these standards to show that they are all PAHs containing nitrogen. The spectra were all nearly identical below m/z = 60 amu, so the spectra shown here are in the range m/z 60-190 amu, where the greatest difference was seen. A further reason to avoid drawing conclusions from the MS spectra below 60 amu is that the main decomposition products of MWNTs are found there [Vandsburger et al., 2013b]. The fragments of major parent ions of interest, namely pyrrolic and polycyclic molecules, occur at nearly the same m/z positions in MS spectra as these decomposition products. Nonetheless, the spectrum below 60 amu is given in the inset to Figure 6.5, to show that the data matches short, unsaturated linear hydrocarbons.

The presence of a molecule with m/z = 67 amu is confirmed in all spectra. Judging from FTIR and OAS analysis, this has been identified as pyrrole and the fragmentation pattern is in good agreement with the standard provided by the NIST. The spectra from O_2 tests all contained a signal from a parent ion at 83 amu, which has been attributed to oxidized pyrrole (C_4H_4NO). O_2 spectra also contained parent ions around 150 amu, corresponding to over-oxidized PPy, which helps to confirm the findings of oxidized PPy in FTIR and OAS data. The ions m/z = 83 amu and 149-150 amu were absent from inert gas tests, thereby supporting their identification as oxidized aromatics. All spectra contained signals at 135 amu, which has been identified as two-monomer length PPy. The peaks at 167 amu and 128 amu are attributable to the PAHs carbozole and quinoline. The peak at 78 amu that is absent from O_2 tests has been shown to be produced in inert plasma treatments of unsaturated hydrocarbon gases. For this reason, it can be identified as a linear alkyne or pyridine [Thejaswini et al., 2011]. Pyridine is indicated by the presence of an ion corresponding to bi-pyridine (m/z 158 amu) in spectra taken in Ar and

the absence of characteristic fragmentation patterns of linear hydrocarbons.The absence of bi-pyridine in N_2 data is attributed to the higher concentration of active nitrogen in N_2 tests. This favours the formation of lighter rings, as has been seen in comparing the spectra from Ar and N_2 experiments. N_2 tests show stronger signals at m/z = 67 and 135 amu, corresponding to pyrrole-like molecules and PPy-PP, than in Ar tests, as well as a weaker signal at m/z = 78 amu and 105-108 amu, which are attributable to linear alkynes as well as to PAHs. The peak at m/z = 100 amu is likely a fragment of the peak at m/z = 129 amu, as shown in the spectrum of NIST standards. Finally, the peak at 179 amu that is present in Ar and N_2 spectra, but is absent from O_2 spectra matches acridine and serves to confirm the finding that acridine synthesis occurs in inert plasma experiments. Acridine, as seen in Table 6.2, is a PAH comprised of two six member rings formed on either side of a pyrrolic ring. The inhibition of the formation of multi-ring systems that has been reported in literature explains the absence of this peak in spectra from O_2 experiments, and further supports the hypothesis that the plasma polymer coating observed in FTIR measurements is indeed produced by gas phase plasma processes.

It is possible that surface nucleation of PAHs is catalyzed by the carbon pellets. It is likely that those reactions do occur, but it is also likely that the products of those reactions would not by pyrrolic. If the carbon pellets act as a template for carbon ring nucleation, soot nucleation mechanisms would dominate [Fincke et al., 2002]. This seems probable, considering the composition of the major products of electron bombardment degradation. The formation of soot is a nucleation process that begins with the formation of benzene and toluene, neither of which was detected in the late-eluting products in the GC. Toluene has been detected in previously reported work and was found to elute in a separate part of the chromatography procedure, since the GC instrument used a non-polar column [Vandsburger et al., 2013a].

Table 6.2: List of Parent Ions Detected in Reaction Products

Chemical Structure	Parent Ion Mass
Pyrrole 	67
Pyridine 	78
Aniline 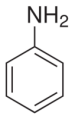	92
Quinoline 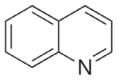	129
Bipyridine 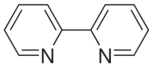	156
Carbazole 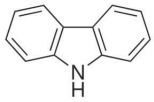	167
Acridine 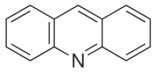	179

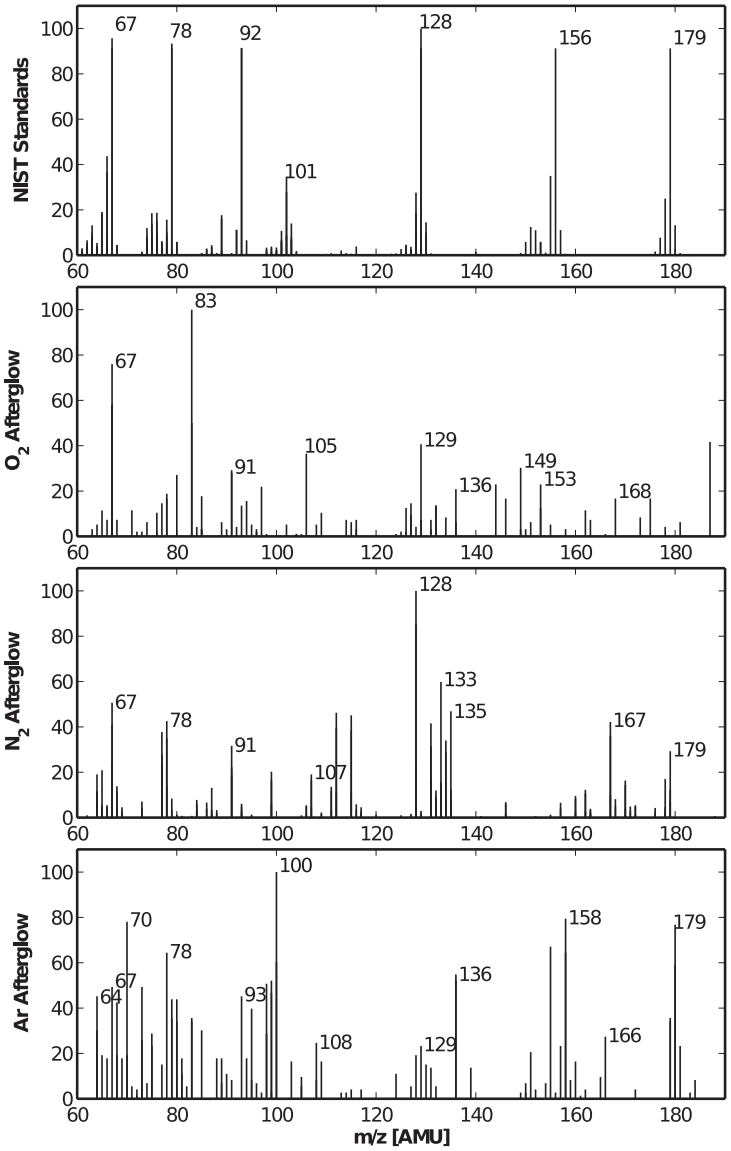

Figure 6.6: Mass spectra of condensed organic vapors from RF afterglow experiments in O_2, N_2, and Ar, with NIST standards given for reference. The presence of acridine is confirmed in Ar and N_2 spectra, as observed in OAS measurements. O_2 plasma treatment produces over-oxidized pyrrole and PPy, as shown in OAS, but favours short chain polymers, while spectra from inert gas treatments show a higher presence of polycyclic molecules.

6.5 Conclusion

The present work provides clear evidence for a subtle reaction scheme beginning with the localized degradation of MWNTs, proceeding with the formation of plasma phase precursors, and ending with the plasma polymerization of PPy-PP onto the remaining section of the MWCNTs to ultimately form a MWNT-PPy-PP nanocomposite coating. This MWNT-PPy-PP nanocomposite coating is in native electrical contact with the metal substrate beneath, thus providing a base structure for the future development of new biocompatible electrode materials or electro-luminescent devices.

6.6 Acknowledgements

The authors gratefully acknowledge the financial support provided by the Natural Sciences and Engineering Research Council of Canada and the Fonds de recherche du Québec - Nature et technologies. The authors also acknowledge the expertise of Mr. Ranjan Roy in operating the GC-MS instrument.

CHAPTER 7

CONCLUSION

7.1 Project Summary

The work that has been presented in the preceding chapters comprises the results of a fundamental study of the interaction between MWNTs and energized gases, by means of charged particle bombardment in RF afterglows. The individual effects of electron bombardment, ion bombardment, and gas phase plasma reactions have been found and have been confirmed to occur in concert during cathodic operation in DC glow discharges. In addition, pioneering work has begun on the development of MWNT-polymer composite materials with electrically conductive polymers (ECPs). The initial results of this work indicate that incorporation of ECP-coated MWNTs can improve charge distribution in OLET devices.

Preliminary experiments were designed to test the use of MWNTs as a nanostructured surface for enhancement of electron emission from metal electrode surfaces. Significant degradation of the MWNT surface was observed in DC operation when the MWNT-covered samples were being used as cathodes in direct contact with an oxidizing plasma. Sputtering of the stainless steel mesh-substrate was limited, however, so the cause of MWNT degradation was not attributed to the kinetic effects of ion bombardment, but rather to plasma chemical reactions taking place at the surface of the MWNT layers.

The MWNT-covered stainless steel mesh material provided the ideal starting point for experimental investigation of the various causes of chemical degradation in MWNT-plasma systems. A new plasma system was designed to "force" a particular type of surface interaction. In the new arrangement, a capacitively coupled radio-frequency

glow discharge produced charged particles in a separate circuit from the MWNT samples, which were placed in the afterglow region of the discharge. The MWNTs were electrically decoupled from the plasma and did not act as electrodes in the system. By applying a DC surface bias on the MWNT-covered mesh samples, the charged particles present in the plasma could be selectively recruited to the MWNTs and the resulting chemical reactions could be studied.

The specific goals of investigation were to identify the major types of covalent functionalization occurring during ion bombardment, the effect of electron bombardment on CNT stability, and to characterize the effect of plasma composition on plasma chemistry and plasma polymerization that occurred simultaneously with MWNT degradation. Optical spectroscopy of the plasma (OES) and of the gas in the chamber (OAS) revealed that the bombardment of MWNTs by charged particles has a distinct dependence on charge, with electrons and positive ions yielding entirely different forms of degradation. Analysis of condensed vapours from the plasma chamber revealed the types of products produced during degradation, and helped to develop a greater understanding of plasma reactions.

The findings of experimental studies of ion bombardment tests indicated that a carboxylic-anhydride surface functional group was preferred over other forms of covalent functionalization. Computational chemistry techniques were explored to justify this finding, and initial results corroborated that carboxylic-anhydrides indeed were the lowest energy state in the particular system of interest. Electron microscope images showed that degradation occured during oxygen functionalization, implicating the disruption of the MWNT lattice by oxidation. The images also showed that degradation was localized to the tips of the MWNT forest that covered the stainless steel substrate. The discovery of tip-localization supported the hypothesis that degradation is inherent in the use of MWNTs for electric field enhancement, at least in low pressure systems

with significant electron and ion densities.

A hypothesis based on numerous literature sources proposed that electric current can cause spontaneous failure in CNTs by thermal evaporation. Using the same system to induce electron bombardment, a similar tip localization of degradation was observed. The molecular products of degradation were found to be short unsaturated hydrocarbons, consistent with the thermal decomposition of graphitic carbon. By studying the kinetics of the oxidation of these products it was found that the rate of consumption of oxygen followed a fractional-order rate model. A fractional reaction order indicates that the production of carbon from the degradation of MWNTs is decoupled from the consumption of oxygen, as is typically seen in gasification processes, where gaseous carbon is produced by thermal volatilization of solid carbon sources. It is therefore a reasonable conclusion that the degradation under electron bombardment was not elicited by chemical reaction with atoms or molecules in the plasma, but rather by thermal effects resulting from electron bombardment.

Investigation of the effect of plasma composition helped to support the conclusion that MWNT degradation did not result from plasma chemistry. Measurements of the gas-phase chemistry in N_2, O_2, and Ar plasmas produced identical compositions of short-unsaturated hydrocarbons, which had been shown to result from electron-bombardment induced degradation. Plasma synthesis of cyclic and polycyclic hydrocarbons, however, showed a significant dependence on plasma composition. The reaction products were primarily pyrrole and poly-pyrrole, with up to five-molecular weight polymers being detected. In addition, plasmas in Ar and N_2 showed an increased presence of higher ring-number molecules and the presence of carbazole and acridine. These molecules are pyrrole and pyridine, respectively, surrounded by two aromatic rings and are fluorescent molecules that form a part of electroluminescent polymer composites.

7.2 Discussion and Synthesis of a Unified Conclusion

The initial hypothesis put forward for this work predicted that MWNTs would provide a stable alternative to conventional tungsten-coil electrode materials for DC glow discharge applications. However, the findings of this study indicate that there is a chemical limitation to the stability of MWNTs in low-pressure glow discharge applications. The magnitude of the operating voltage was not found to have a strong effect. Ar tests for both types of experiment were found to elicit similar degradation to electron bombardment from O_2 plasma, despite operating at a sample bias of + 75 VDC relative to the + 200 VDC of O_2 and N_2 tests. The findings of ion bombardment tests did not show the same effect, understandably, since Ar does not lead to the same covalent functionalization and does not cause reactive cleaving of the CNT lattice. The data gathered during this project allow for the development of a unified understanding of the degradation processes of MWNTs in the presence of electron and ion bombardment from plasmas with significant charge densities.

The impact of charge density was not tested directly, but can be deduced by studies of degradation in field-emission applications under ultra-high vacuum (UHV). The degradation mechanism of MWNT field-emitters is dominated by electric current induced evaporation by resistive heating. Covalent functionalization is not a significant contributor, due to the low density of particles under UHV conditions. In low-pressure glow discharge applications the high density of charged particles prevents field-emission. Ion bombardment of MWNTs causes charge recombination at the tips of MWNTs, leading to adsorption of ions and covalent functionalization. It is not surprising, then, to observe that the ion bombardment degradation that was described in this project dominates in low-pressure glow discharges. Indeed, the types of reaction products typical of oxidation of unsaturated hydrocarbons, CO, C, and CO_2, were not

observed during DC electrode experiments, indicating that thermal evaporation is a minor effect in the degradation process.

After considering the findings, it can be concluded that the chemical inactivity of graphitic carbon, which has been one of the leading reasons behind the materials' enthusiastic adoption for technologies involving exposure to plasmas [Hirsch, 2010, Ostrikov et al., 2013], is compromised by exposure to focused bombardment by energized particles. While the MWNTs are allowed to float at the plasma potential the increased chemical reactivity allows for useful functionalization, but the effect becomes destructive when electric fields are applied and the MWNT tips act to concentrate the bombardment of incoming charged particles. Excess energy overrides the natural tendency of reactive species to prefer energetic sites on the CNT lattice, and causes reactions to occur despite energy barriers that render them unlikely in normal conditions.

The impact of these findings is considerable, based on the ability to induce highly-localized covalent functionalization as well as very strict length-control. The type of chemical functionalization can be controlled by specification of the plasma composition. Since the plasma is produced independently of the MWNT substrate that is the target of ion bombardment, plasma composition is independent and can be tailored to contain atoms and molecules of choice. This has already been done with simple gases in this project, but the possibility of introducing more interesting gases is obvious. The importance of length control is to be found in work on MWNT micro-electronics [Lim et al., 2009, Bandaru, 2012]. A uniform MWNT forest layer can be used to produce strong and stable circuit interconnects [Kreupl et al., 2002]. Uniform layers are also desirable for broad-area field-emission applications [Choi et al., 1999, Lee et al., 2012]. The use of electron bombardment offers the additional advantage of tip localization of the thermal evaporation that is responsible for length-shortening. By localizing the thermal effects to the region near the tips of MWNTs, defects and other lattice non-idealities are

preserved over the remaining MWNT length. These defects are useful locations for nucleation of metal nanoparticles or as targets for non-directed sidewall-functionalization. The conservation of these defects will allow for the production of uniform functionalized MWNT layers for sensor applications or for biocompatible electrode materials.

The development of MWNT-ECP composites is a natural development of the work on mechanism determination, since plasma polymer deposition is a typical effect observed in organic-containing plasmas. MWNT-ECPs constitute a valuable product that could be used for production of OLETs, as was begun in this project, as well as in other conductive-polymer applications. Potential results could include polymer-coated MWNT electrodes, MWNT inks that contain iron nanoparticles for bio-marking and nano-magnetic applications such as organic computing.

7.3 Summary of Contributions

The work in this project led to the formulation of several important findings that constitute original contributions to the fields of nanomaterials, plasma-surface interactions, and plasma chemistry. They are summarized in the list below:

- **New method for tailored functionalization of MWNTs:** The plasma system that was developed to isolate the effects of ion and electron bombardment on MWNT degradation constituted the first report of a method to selectively induce localized surface functionalization at the tips of MWNTs by taking advantage of tip-localized electric field concentration. Charged particles in the plasma are recruited directly to the tips of MWNTs to elicit covalent functionalization. Current plasma functionalization techniques cannot localize functionalization, but rather cause random reactions throughout the lengths of affected CNTs.

- **Covalent functionalization of MWNTs:** The exact chemistry of covalent func-

tionalization of MWNTs by oxygen atoms was observed during oxygen ion bombardment of MWNTs. It was found that functionalization by a mixture of diatomic and atomic oxygen forms carboxylic anhydride groups, even in the presence of hydrogen ions. The formation of dicarboxylic anhydride groups has not yet been reported in literature, which typically uses XPS to identify the products of oxygen functionalization of MWNTs.

- **Electron bombardment degradation of MWNTs:** The products of thermal degradation of MWNTs by electron bombardment have been identified, for the first time. Prior work on thermal stability of MWNTs in field-emission applications has shown that electrical current causes thermal failure, but the products have not been reported prior to this project. It was found that thermal degradation produces a gas of short unsaturated hydrocarbons, mostly butadiyne and propyne.

- **Plasma polymer films:** For the first time in literature, this project reported the *in situ* production of MWNT-ECP composites by gas phase plasma polymerization and deposition. The importance of this approach is that it produces a composite of native-MWNTs and luminescent-conductive polymers, without requiring suspension of MWNTs in a polymer liquid or in a functionalization medium. The tip-localized degradation that produced the reactants for plasma polymerization reactions did not alter the chemistry of the remaining CNTs, so functionalization and coating are separated in this method, which has also not yet been demonstrated.

7.4 Suggestions for Future Work

The following avenues for future work would likely yield further innovative findings. The suggested work would help in the effort to develop the scientific community's un-

derstanding of plasma-MWNT interaction; and it would aid the work of technologists to develop new nanomaterials incorporating functionalized MWNT forests.

- **Tailored Functionalization:** It is suggested that the field-enhanced bombardment functionalization approach be explored with more complex functionalization chemicals. A local functionalization with ammonia or halogens, for example could be exceedingly useful for building complex organic conjugates. Deposition of aerosols by this method could also be achieved, in a new way to produce MWNT-biochemical composites.

- **Plasma polymer film composites:** The production of MWNT-ECPs has never been reported for a system where the MWNTs remain in native contact with the CVD growth substrate. This technique could prove very useful for development of MWNT-composite electrodes, wherein the MWNTs protect the metal substrate beneath from environmental exposure while maintaining strong electrical contact with both the metal surface and the environment. CNT bio-electrodes have already been reported in literature, and have been shown to improve biocompatibility of neural stimulation electrodes. The MWNT-ECP materials produced during this project could potentially represent a significant improvement over what has already been developed. It is suggested, therefore, that the development of electrode materials for neural stimulation be investigated.

- **OLET development:** Application development work has produced stabilized nanofluid suspensions of CNTs in ir[ppy]3:PVK and chlorobenzene. Thin film composite materials have been assembled from these nanofluids by spin-coating. This has been reported in literature recently, but the use of functionalized CNTs that have plasma deposited ECP coatings is a new development that has not been reported elsewhere.

The purpose of functionalization and ECP-coatings is to better interface the MWNTs with the polymer film matrix, which thus far not been attempted by experimental applications of CNT-ECP composites. This project has developed a feasible avenue for the development of MWNT-plasma polymer materials that could be used in electroluminescent films, fluorescent nanofluids, or in fluorescent nano-inks. The development of technologies based on MWNT-plasma polymer composites could yield significant results in a short time-frame.

BIBLIOGRAPHY

Allen, B., Kichambare, P., and Star, A. (2007). Carbon nanotube field-effect-transistor-based biosensors. *Advanced Materials*, 19(11):1439–1451.

Andrews, R., Jacques, D., Qian, D., and Dickey, E. (2001). Purification and structural annealing of multiwalled carbon nanotubes at graphitization temperatures. *Carbon*, 39(11):1681 – 1687.

Artemenko, A., Kylián, O., Choukourov, A., Gordeev, I., Petr, M., Vandrovcová, M., Polonskyi, O., Bačáková, L., Slavinska, D., and Biederman, H. (2012). Effect of sterilization procedures on properties of plasma polymers relevant to biomedical applications. *Thin Solid Films*, 520(24):7115 – 7124.

Ayala, P., Arenal, R., Rmmeli, M., Rubio, A., and Pichler, T. (2010). The doping of carbon nanotubes with nitrogen and their potential applications. *Carbon*, 48(3):575 – 586.

Baddour, C. E., Fadlallah, F., Nasuhoglu, D., Mitra, R., Vandsburger, L., and Meunier, J.-L. (2009). A simple thermal cvd method for carbon nanotube synthesis on stainless steel 304 without the addition of an external catalyst. *Carbon*, 47(1):313 – 318.

Baik, C.-W., Lee, J., Choi, J. H., Jung, I., Choi, H. R., Jin, Y. W., and Kim, J. M. (2010). Structural degradation mechanism of multiwalled carbon nanotubes in electrically treated field emission. *Applied Physics Letters*, 96(2):023105.

Bakshi, S. R., Lahiri, D., and Agarwal, A. (2010). Carbon nanotube reinforced metal matrix composites - a review. *International Materials Reviews*, 55(1):41–64.

Bandaru, P. R. (2012). Carbon nanotube y-junctions. *Microelectronics to Nanoelectronics: Materials, Devices & Manufacturability*, page 277.

Barros, T., Molinari, G., Filho, P. B., Toscano, V., and Politi, M. (1993). Photophysical properties of n-alkylnaphthalimides and analogs. *Journal of Photochemistry and Photobiology A: Chemistry*, 76(1–2):55 – 60.

Barros, T., Yunes, S., Menegon, G., Nome, F., Chaimovich, H., Politi, M., Dias, L., and Cuccovia, I. (2001). Hydrolysis of 1,8- and 2,3-naphthalic anhydrides and the mechanism of cyclization of 1,8-naphthalic acid in aqueous solutions. *Journal of the Chemical Society, Perkin Transactions 2*, (12):2342–2350.

Benedikt, J. (2010). Plasma–chemical reactions: low pressure acetylene plasmas. *Journal of Physics D: Applied Physics*, 43(4):043001–22.

Biniak, S., Szymański, G., Siedlewski, J., and Światkowski, A. (1997). The characterization of activated carbons with oxygen and nitrogen surface groups. *Carbon*, 35(12):1799–1810.

Bokobza, L. (2007). Multiwall carbon nanotube elastomeric composites: A review. *Polymer*, 48(17):4907 – 4920.

Bonanni, A. and del Valle, M. (2010). Use of nanomaterials for impedimetric dna sensors: A review. *Analytica Chimica Acta*, 678(1):7 – 17.

Bonard, J.-M., Klinke, C., Dean, K. A., and Coll, B. F. (2003). Degradation and failure of carbon nanotube field emitters. *Phys. Rev. B*, 67:115406.

Bora, C. and Dolui, S. (2012). Fabrication of polypyrrole/graphene oxide nanocomposites by liquid/liquid interfacial polymerization and evaluation of their optical, electrical and electrochemical properties. *Polymer*, 53(4):923–932.

Brezinsky, K., Burke, E., and Glassman, I. (1985). The high temperature oxidation of butadiene. *Symposium (International) on Combustion*, 20(1):613 – 622.

Bruckner, A. and Baerns, M. (1997). Selective gas-phase oxidation of polycyclic aromatic hydrocarbons on vanadium oxide-based catalysts. *Applied Catalysis A: General*, 157(1,2):311 – 334.

Bsoul, A., Ali, M., and Takahata, K. (2011). Piezoresistive pressure sensor using vertically aligned carbon-nanotube forests. *Electronics letters*, 47(14):807–808.

Charlier, J.-C. and Issi, J.-P. (1998). Electronic structure and quantum transport in carbon nanotubes. *Applied Physics A*, 67(1):79–87.

Chen, C., Liang, B., Lu, D., Ogino, A., Wang, X., and Nagatsu, M. (2010). Amino group introduction onto multiwall carbon nanotubes by nh3/ar plasma treatment. *Carbon*, 48(4):939 – 948.

Chen, C., Liang, B., Ogino, A., Wang, X., and Nagatsu, M. (2009). Oxygen functionalization of multiwall carbon nanotubes by microwave-excited surface-wave plasma treatment. *The Journal of Physical Chemistry C*, 113(18):7659–7665.

Chen, C., Ogino, A., Wang, X., and Nagatsu, M. (2011a). Oxygen functionalization of multiwall carbon nanotubes by ar/h2o plasma treatment. *Diamond and Related Materials*, 20(2):153 – 156.

Chen, H., Guo, L., Ferhan, A. R., and Kim, D.-H. (2011b). Multilayered polypyrrole-coated carbon nanotubes to improve functional stability and electrical properties of neural electrodes. *The Journal of Physical Chemistry C*, 115(13):5492–5499.

Chen, Y., Haddon, R., Fang, S., Rao, A., Eklund, P., Lee, W., Dickey, E., Grulke, E.,

Pendergrass, J., Chavan, A., et al. (1998). Chemical attachment of organic functional groups to single-walled carbon nanotube material. *J. Mater. Res*, 13(9):2423–2431.

Chen, Y., Smith, G. M., Loughman, E., Li, Y., Nie, W., and Carroll, D. L. (2013). Effect of multi-walled carbon nanotubes on electron injection and charge generation in ac field-induced polymer electroluminescence. *Organic Electronics*, 14(1):8 – 18.

Cheung, C. L., Kurtz, A., Park, H., and Lieber, C. M. (2002). Diameter-controlled synthesis of carbon nanotubes. *The Journal of Physical Chemistry B*, 106(10):2429–2433.

Cho, B., Chung, S., Kim, K., Kang, T., Park, C., and Kim, B. (2000). Direct observation of oxygen-induced structural changes in stainless-steel surfaces. *Journal of Vacuum Science & Technology B: Microelectronics and Nanometer Structures*, 18(2):868–872.

Choi, W., Chung, D., Kang, J., Kim, H., Jin, Y., Han, I., Lee, Y., Jung, J., Lee, N., Park, G., et al. (1999). Fully sealed, high-brightness carbon-nanotube field-emission display. *Applied physics letters*, 75:3129.

Christophorou, L. G. and Olthoff, J. K. (2004). *Fundamental Electron Interactions With Plasma Processing Gases*. Springer Science+Business Media.

Chung, O. N. and Chung, S. (2003). Scanning tunneling microscopy and spectroscopy studies of the oxide nanofilms on the stainless steel surface. *Journal of Vacuum Science & Technology B: Microelectronics and Nanometer Structures*, 21(4):1297–1300.

Collins, P. G., Arnold, M. S., and Avouris, P. (2001). Engineering carbon nanotubes and nanotube circuits using electrical breakdown. *Science*, 292(5517):706–709.

Conrads, H. and Schmidt, M. (2000). Plasma generation and plasma sources. *Plasma Sources Science and Technology*, 9(4):441.

Consoli, A., Benedikt, J., and Von Keudell, A. (2008). Initial polymerization reactions in particle-forming ar/he/c2h2 plasmas studied via quantitative mass spectrometry. *The Journal of Physical Chemistry A*, 112(45):11319–11329.

Dagaut, P. and Cathonnet, M. (1998). The oxidation of 1,3-butadiene: Experimental results and kinetic modeling. *Combustion Science and Technology*, 140(1-6):225–257.

Dahmardeh, M., Mohamed Ali, M. S., Saleh, T., Hian, T. M., Moghaddam, M. V., Nojeh, A., and Takahata, K. (2013). High-power mems switch enabled by carbon-nanotube contact and shape-memory-alloy actuator. *physica status solidi (a)*, 210(4):631–638.

de Barros, T. C., Filho, P. B., Loos, M., Politi, M. J., Chaimovich, H., and Cuccovia, I. M. (2011). Formation and decomposition of n-alkylnaphthalimides: experimental evidences and ab initio description of the reaction pathways. *Journal of Physical Organic Chemistry*, 24(5):385–397.

De Bleecker, K., Bogaerts, A., and Goedheer, W. (2006). Aromatic ring generation as a dust precursor in acetylene discharges. *Applied physics letters*, 88(15):151501–151501.

De Volder, M. F., Tawfick, S. H., Baughman, R. H., and Hart, A. J. (2013). Carbon nanotubes: present and future commercial applications. *science*, 339(6119):535–539.

Dean, K. A. and Chalamala, B. R. (2000). Current saturation mechanisms in carbon nanotube field emitters. *Applied Physics Letters*, 76(3):375–377.

Dionne, M., Coulombe, S., and Meunier, J.-L. (2008). Screening effects between field-enhancing patterned carbon nanotubes: A numerical study. *Electron Devices, IEEE Transactions on*, 55(6):1298 –1305.

Dionne, M., Coulombe, S., and Meunier, J.-L. (2009). Energy exchange during electron emission from carbon nanotubes: Considerations on tip cooling effect and destruction of the emitter. *Phys. Rev. B*, 80.

Dresselhaus, M., Dresselhaus, G., Eklund, P., and Rao, A. (2000). Carbon nanotubes. In Andreoni, W., editor, *The Physics of Fullerene-Based and Fullerene-Related Materials*, volume 23 of *Physics and Chemistry of Materials with Low-Dimensional Structures*, pages 331–379. Springer Netherlands.

Dresselhaus, M. S., Dresselhaus, G., Saito, R., and Jorio, A. (2005). Raman spectroscopy of carbon nanotubes. *Physics Reports*, 409(2):47–99.

Dresselhaus, M. S. and Eklund, P. C. (2000). Phonons in carbon nanotubes. *Advances in Physics*, 49(6):705–814.

Eliasson, B. and Kogelschatz, U. (1991). Nonequilibrium volume plasma chemical processing. *Plasma Science, IEEE Transactions on*, 19(6):1063–1077.

Fan, S., Chapline, M. G., Franklin, N. R., Tombler, T. W., Cassell, A. M., and Dai, H. (1999). Self-oriented regular arrays of carbon nanotubes and their field emission properties. *Science*, 283(5401):512–514.

Felten, A., Bittencourt, C., Pireaux, J. J., Van Lier, G., and Charlier, J. C. (2005). Radio-frequency plasma functionalization of carbon nanotubes surface o_2, nh_3, and cf_4 treatments. *Journal of Applied Physics*, 98(7):074308–9.

Felten, A., Ghijsen, J., Pireaux, J.-J., Johnson, R. L., Whelan, C. M., Liang, D., Tendeloo, G. V., and Bittencourt, C. (2007). Effect of oxygen rf-plasma on electronic properties of cnts. *Journal of Physics D: Applied Physics*, 40(23):7379.

Fincke, J. R., Anderson, R. P., Hyde, T. A., and Detering, B. A. (2002). Plasma pyrolysis of methane to hydrogen and carbon black. *Industrial & engineering chemistry research*, 41(6):1425–1435.

Franceschi, P., Guella, G., Scarduelli, G., Tosi, P., Dilecce, G., and De Benedictis, S. (2007). Chemical processes in the atmospheric pressure plasma treatment of benzene. *Plasma Processes and Polymers*, 4(5):548–555.

Frank, B., Rinaldi, A., Blume, R., Schlägl, R., and Su, D. S. (2010). Oxidation stability of multiwalled carbon nanotubes for catalytic applications. *Chemistry of Materials*, 22(15):4462–4470.

Friedel, R. and Orchin, M. (1951). *Ultraviolet Spectra of Aromatic Compounds*. John Wiley & Sons, Inc.

Furuhashi, M. and Komeda, T. (2008). Chiral vector determination of carbon nanotubes by observation of interference patterns near the end cap. *Physical review letters*, 101(18):185503.

General, A., Kel'man, V., Zhmenjak, Y., and Shpenik, Y. (2010). A uv source on hydroxyl molecules operating in a pulsed-periodic mode. *Instruments and Experimental Techniques*, 53:558–560.

Ghatak, S., Chakraborty, G., Meikap, A. K., Woods, T., Babu, R., and Blau, W. J. (2011). Synthesis and characterization of polyaniline/carbon nanotube composites. *Journal of Applied Polymer Science*, 119(2):1016–1025.

Gilman, A., Yablokov, M., and Kuznetsov, A. (2012). Modification of carbon nano-objects in low-temperature plasma for use in polymer nanocomposites. *High Energy Chemistry*, 46(4):219–228.

Ginic-Markovic, M., Matisons, J. G., Cervini, R., Simon, G. P., and Fredericks, P. M. (2006). Synthesis of new polyaniline/nanotube composites using ultrasonically initiated emulsion polymerization. *Chemistry of Materials*, 18(26):6258–6265.

Green, A. A. and Hersam, M. C. (2011). Cnt electronics: Nearly single-chirality single-walled carbon nanotubes produced via orthogonal iterative density gradient ultracentrifugation (adv. mater. 19/2011). *Advanced Materials*, 23(19):2127–2127.

Green, R., Williams, C., Lovell, N., and Poole-Warren, L. (2008). Novel neural interface for implant electrodes: improving electroactivity of polypyrrole through mwnt incorporation. *Journal of Materials Science: Materials in Medicine*, 19:1625–1629.

Guo, T., Nikolaev, P., Thess, A., Colbert, D., and Smalley, R. (1995). Catalytic growth of single-walled manotubes by laser vaporization. *Chemical Physics Letters*, 243(12):49 – 54.

Guo, Y., Gu, X., and Kaiser, R. I. (2006). Mass spectrum of the 1-butene-3-yne-2-yl radical (i-c_4h_3; x^2aå). *International Journal of Mass Spectrometry*, 249 - 250(0):420 – 425.

Guo, Y., Jiang, L., and Guo, W. (2010a). Opening carbon nanotubes into zigzag graphene nanoribbons by energy-optimum oxidation. *PHYSICAL REVIEW B*, 82(115440).

Guo, Y., Zhang, Z., and Guo, W. (2010b). Selective oxidation of carbon nanotubes into

zigzag graphene nanoribbons. *The Journal of Physical Chemistry C*, 114(35):14729–14733.

Hansen, N., Miller, J., Kasper, T., Kohse-Höinghaus, K., Westmoreland, P., Wang, J., and Cool, T. (2009). Benzene formation in premixed fuel-rich 1,3-butadiene flames. *Proceedings of the Combustion Institute*, 32(1):623 – 630.

Hanwell, M. D., Curtis, D. E., Lonie, D. C., Vandermeersch, T., Zurek, E., and Hutchison, G. R. (2012). Avogadro: An advanced semantic chemical editor, visualization, and analysis platform. *Journal of Cheminformatics*, 4(17).

Hata, K., Takakura, A., and Saito, Y. (2001). Field emission microscopy of adsorption and desorption of residual gas molecules on a carbon nanotube tip. *Surface science*, 490(3):296–300.

Heo, S., Ihsan, A., Yoo, S., Ali, G., and Cho, S. (2010). Stable field emitters for a miniature x-ray tube using carbon nanotube drop drying on a flat metal tip. *Nanoscale Research Letters*, 5(4):720–724.

Herzberg, G. (1944). *Atomic Spectra and Atomic Structure*, page 234. Dover Publications.

Hirsch, A. (2010). The era of carbon allotropes. *Nature Materials*, 9:868–871.

Hirsch, A. and Vostrowsky, O. (2005). Functionalization of carbon nanotubes. In Schlter, A., editor, *Functional Molecular Nanostructures*, volume 245 of *Topics in Current Chemistry*, pages 193–237. Springer Berlin Heidelberg.

Ho, G., Wee, A., and Lin, J. (2001). Electric field-induced carbon nanotube junction formation. *Applied Physics Letters*, 79(2):260–262.

Hodge, S. A., Bayazit, M. K., Coleman, K. S., and Shaffer, M. S. P. (2012). Unweaving the rainbow: a review of the relationship between single-walled carbon nanotube molecular structures and their chemical reactivity. *Chem. Soc. Rev.*, 41:4409–4429.

Hordy, N., Coulombe, S., and Meunier, J.-L. (2013). Plasma functionalization of carbon nanotubes for the synthesis of stable aqueous nanofluids and poly(vinyl alcohol) nanocomposites. *Plasma Processes and Polymers*, 10(2):110–118.

Hrdlovic, P., Chmela, S., Sarakha, M., and Lacoste, J. (2001). Transient absorption spectra of bifunctional probes of a chromophore-sterically hindered amine type in solution; study of the triplet route to deactivation. *Journal of Photochemistry and Photobiology A: Chemistry*, 138(2):95 – 109.

Hu, H., Ni, Y., Montana, V., Haddon, R. C., and Parpura, V. (2004). Chemically functionalized carbon nanotubes as substrates for neuronal growth. *Nano Letters*, 4(3):507–511.

Hu, J., Odom, T. W., and Lieber, C. M. (1999). Chemistry and physics in one dimension: synthesis and properties of nanowires and nanotubes. *Accounts of Chemical Research*, 32(5):435–445.

Huang, J. Y., Kempa, K., Jo, S. H., Chen, S., and Ren, Z. F. (2005). Giant field enhancement at carbon nanotube tips induced by multistage effect. *Applied Physics Letters*, 87(5):053110.

Huang, N. Y., She, J. C., Chen, J., Deng, S. Z., Xu, N. S., Bishop, H., Huq, S. E., Wang, L., Zhong, D. Y., Wang, E. G., and Chen, D. M. (2004). Mechanism responsible for initiating carbon nanotube vacuum breakdown. *Phys. Rev. Lett.*, 93:075501.

Hurt, R. H. and Haynes, B. S. (2005). On the origin of power-law kinetics in carbon oxidation. *Proceedings of the Combustion Institute*, 30(2):2161 – 2168.

Huyen, D. N., Tung, N. T., Vinh, T. D., and Thien, N. D. (2012). Synergistic effects in the gas sensitivity of polypyrrole/single wall carbon nanotube composites. *Sensors*, 12(6):7965–7974.

Iijima, S. (1991). Helical microtubules of graphitic carbon. *Nature*, 354:56 – 58.

Ikegami, T., Nakanishi, F., Uchiyama, M., and Ebihara, K. (2004). Optical measurement in carbon nanotubes formation by pulsed laser ablation. *Thin Solid Films*, 457(1):7 – 11.

Jan, E., Hendricks, J. L., Husaini, V., Richardson-Burns, S. M., Sereno, A., Martin, D. C., and Kotov, N. A. (2009). Layered carbon nanotube-polyelectrolyte electrodes outperform traditional neural interface materials. *Nano Letters*, 9(12):4012–4018. PMID: 19785391.

Jeyabharathi, C., Venkateshkumar, P., Mathiyarasu, J., and Phani, K. L. N. (2010). Carbon-supported palladium - polypyrrole nanocomposite for oxygen reduction and its tolerance to methanol. *J. Electrochem. Soc.*, 157(11):B1740–B1745.

Jhi, S.-H., Louie, S. G., and Cohen, M. L. (2000). Electronic properties of oxidized carbon nanotubes. *Phys. Rev. Lett.*, 85:1710–1713.

Jorio, A., Dresselhaus, G., and Dresselhaus, M. S. (2008). *Carbon Nanotubes : Advanced Topics in the Synthesis, Structure, Properties and Applications*. Springer-Verlag Berlin/Heidelberg.

Joselevich, E., Dai, H., Liu, J., Hata, K., and H.Windle, A. (2008). Carbon nanotube

synthesis and organization. In *Carbon Nanotubes*, volume 111 of *Topics in Applied Physics*, pages 101–164. Springer Berlin Heidelberg.

Jung, S. M., Jung, H. Y., and Suh, J. S. (2007). Horizontally aligned carbon nanotube field emitters having a long term stability. *Carbon*, 45(15):2917 – 2921.

Kalra, N., Santhanam, K., and Olney, D. (2012). Nickel multi-walled carbon nanotube composite electrode for hydrogen generation. *MRS Online Proceedings Library*, 1387(1).

Kautzman, K. E., Surratt, J. D., Chan, M. N., Chan, A. W. H., Hersey, S. P., Chhabra, P. S., Dalleska, N. F., Wennberg, P. O., Flagan, R. C., and Seinfeld, J. H. (2010). Chemical composition of gas- and aerosol-phase products from the photooxidation of naphthalene. *The Journal of Physical Chemistry A*, 114(2):913–934.

Kim, J., Choi, W., Lee, N., and Jung, J. (2000). Field emission from carbon nanotubes for displays. *Diamond and Related Materials*, 9(3):1184–1189.

Kim, J.-Y., Jeong, T., Baik, C.-W., Park, S. H., Han, I., Kim, G.-H., and Yu, S. (2013). Field-emission performance and structural change mechanism of multiwalled carbon nanotubes by oxygen plasma treatment. *Thin Solid Films*, (0):–.

Kitaura, R., Nakanishi, R., Saito, T., Yoshikawa, H., Awaga, K., and Shinohara, H. (2009). High-yield synthesis of ultrathin metal nanowires in carbon nanotubes. *Angewandte Chemie International Edition*, 48(44):8298–8302.

Kochkodan, V. M. and Sharma, V. K. (2012). Graft polymerization and plasma treatment of polymer membranes for fouling reduction: A review. *Journal of Environmental Science and Health, Part A*, 47(12):1713–1727.

Koh, A. L., Gidcumb, E., Zhou, O., and Sinclair, R. (2013). Observations of carbon nanotube oxidation in an aberration-corrected environmental transmission electron microscope. *ACS Nano*, 7(3):2566–2572.

Kong, J., Cassell, A. M., and Dai, H. (1998). Chemical vapor deposition of methane for single-walled carbon nanotubes. *Chemical Physics Letters*, 292(4):567–574.

Kordas, K., Tóth, G., Moilanen, P., Kumpumaki, M., Vahakangas, J., Uusimaki, A., Vajtai, R., and Ajayan, P. (2007). Chip cooling with integrated carbon nanotube microfin architectures. *Applied Physics Letters*, 90(12):123105–123105.

Kosynkin, D. V., Higginbotham, A. L., Sinitskii, A., Lomeda, J. R., Dimiev, A., Price, B. K., and Tour, J. M. (2009). Longitudinal unzipping of carbon nanotubes to form graphene nanoribbons. *Nature*, 458:872 – 876.

Kreupl, F., Graham, A., Duesberg, G., Steinhögl, W., Liebau, M., Unger, E., and Hönlein, W. (2002). Carbon nanotubes in interconnect applications. *Microelectronic Engineering*, 64(14):399 – 408.

Lamberti, F., Ferraro, D., Giomo, M., and Elvassore, N. (2013). Enhancement of heterogeneous electron transfer dynamics tuning single-walled carbon nanotube forest height and density. *Electrochimica Acta*.

Laskin, A., Wang, H., and Law, C. K. (2000). Detailed kinetic modeling of 1,3-butadiene oxidation at high temperatures. *International Journal of Chemical Kinetics*, 32(10):589–614.

Lee, J., Jung, Y., Song, J., Kim, J. S., Lee, G.-W., Jeong, H. J., and Jeong, Y. (2012). High-performance field emission from a carbon nanotube carpet. *Carbon*, 50(10):3889–3896.

Lei, J., Liang, W., and Martin, C. R. (1992). Infrared investigations of pristine, doped and partially doped polypyrrole. *Synthetic metals*, 48(3):301–312.

Li, F., Kan, E., Lu, R., Xiao, C., Deng, K., and Su, H. (2012). Unzipping carbon nanotubes into nanoribbons upon oxidation: A first-principles study. *Nanoscale*, 4:1254–1257.

Li, H., Jo, J. K., Zhang, L., Ha, C.-S., Suh, H., and Kim, I. (2010). A general and efficient route to fabricate carbon nanotube-metal nanoparticles and carbon nanotube-inorganic oxides hybrids. *Advanced Functional Materials*, 20(22):3864–3873.

Li, J., Lu, Y., Ye, Q., Cinke, M., Han, J., and Meyyappan, M. (2003). Carbon nanotube sensors for gas and organic vapor detection. *Nano Letters*, 3(7):929–933.

Li, Y., Liu, J., Wang, Y., and Wang, Z. L. (2001). Preparation of monodispersed fe?mo nanoparticles as the catalyst for cvd synthesis of carbon nanotubes. *Chemistry of Materials*, 13(3):1008–1014.

Li, Y. and Qian, R. (2000). Electrochemical overoxidation of conducting polypyrrole nitrate film in aqueous solutions. *Electrochimica acta*, 45(11):1727–1731.

Lim, S. C., Jang, J. H., Bae, D. J., Han, G. H., Lee, S., Yeo, I.-S., and Lee, Y. H. (2009). Contact resistance between metal and carbon nanotube interconnects: Effect of work function and wettability. *Applied Physics Letters*, 95(26):264103.

Lin, Y.-W. and Wu, T.-M. (2011). Synthesis and characterization of water-soluble polypyrrole/multi-walled carbon nanotube composites. *Polymer International*, 60(3):382–388.

Liu, B., Jiang, H., Krasheninnikov, A. V., Nasibulin, A. G., Ren, W., Liu, C., Kauppinen,

E. I., and Cheng, H.-M. (2013). Chirality-dependent reactivity of individual single-walled carbon nanotubes. *Small*, 9(8):1379–1386.

Liu, L., Wang, T., Li, J., Guo, Z.-X., Dai, L., Zhang, D., and Zhu, D. (2003). Self-assembly of gold nanoparticles to carbon nanotubes using a thiol-terminated pyrene as interlinker. *Chemical physics letters*, 367(5):747–752.

Liu, R., Duay, J., and Lee, S. B. (2011). Heterogeneous nanostructured electrode materials for electrochemical energy storage. *Chemical Communications*, 47(5):1384–1404.

Liu, Z., Tabakman, S., Welsher, K., and Dai, H. (2009). Carbon nanotubes in biology and medicine: in vitro and in vivo detection, imaging and drug delivery. *Nano research*, 2(2):85–120.

López, J., Parres, F., Rico, I., Molina, J., Bonastre, J., and Cases, F. (2010). Monitoring the polymerization process of polypyrrole films by thermogravimetric and x-ray analysis. *Journal of Thermal Analysis and Calorimetry*, 102(2):695–701.

Lourdes, A., Yáñez-Sedeño, P., and Pingarrón, J. M. (2008). Role of carbon nanotubes in electroanalytical chemistry: A review. *Analytica Chimica Acta*, 622(1):11 – 47.

Luo, L., Zhu, L., Xu, Y., Shen, L., Wang, X., Ding, Y., Li, Q., and Deng, D. (2011). Hydrogen peroxide biosensor based on horseradish peroxidase immobilized on chitosan-wrapped nife2o4 nanoparticles. *Microchimica Acta*, 174(1-2):55–61.

Ma, L., Wang, J., and Ding, F. (2012). Strain-induced orientation-selective cutting of graphene into graphene nanoribbons on oxidation. *Angewandte Chemie International Edition*, 51(5):1161–1164.

Marega, R., Giust, D., Kremer, A., and Bonifazi, D. (2012). *Supramolecular Chemistry of Fullerenes and Carbon Nanotubes at Interfaces: Toward Applications*, pages 301–347. Wiley-VCH Verlag GmbH & Co. KGaA.

Marx, R., Wölk, H.-J., Mestl, G., and Turek, T. (2011). Reaction scheme of o-xylene oxidation on vanadia catalyst. *Applied Catalysis A: General*, 398(1–2):37 – 43.

Mathur, A., Roy, S., Hazra, K., Wadhwa, S., Ray, S., Mitra, S., Misra, D., and McLaughlin, J. (2012). Oxygen plasma assisted end-opening and field emission enhancement in vertically aligned multiwall carbon nanotubes. *Materials Chemistry and Physics*, 134(1):425 – 429.

McCreery, R. L. (2008). Advanced carbon electrode materials for molecular electrochemistry. *Chemical Reviews*, 108(7):2646–2687.

Meng, Z., Liu, B., Zheng, J., Sheng, Q., and Zhang, H. (2011). Electrodeposition of cobalt oxide nanoparticles on carbon nanotubes, and their electrocatalytic properties for nitrite electrooxidation. *Microchimica Acta*, 175(3-4):251–257.

Menon, V. P., Lei, J., and Martin, C. R. (1996). Investigation of molecular and supermolecular structure in template-synthesized polypyrrole tubules and fibrils. *Chemistry of materials*, 8(9):2382–2390.

Meunier, J.-L., Mendoza-Gonzalez, N., Pristavita, R., Binny, D., and Berk, D. (2012). Generation and functionalization of pure graphene flake structures in thermal plasma reactors. In *Plasma Science (ICOPS), 2012 Abstracts IEEE International Conference on*, pages 7D–1. IEEE.

Minoux, E., Groening, O., Teo, K. B. K., Dalal, S. H., Gangloff, L., Schnell, J.-P., Hudanski, L., Bu, I. Y. Y., Vincent, P., Legagneux, P., Amaratunga, G. A. J., and

Milne, W. I. (2005). Achieving high-current carbon nanotube emitters. *Nano Letters*, 5(11):2135–2138.

Moisan, M. and Pelletier, J. (2012). *Physics of Collisional Plasmas: Introduction to High-Frequency Discharges*.

Musameh, M., Notivoli, M. R., Hickey, M., Kyratzis, I. L., Gao, Y., Huynh, C., and Hawkins, S. C. (2011). Carbon nanotube webs: a novel material for sensor applications. *Advanced Materials*, 23(7):906–910.

Nakahara, H., Ichikawa, S., Ochiai, T., Kusano, Y., and Saito, Y. (2011). Carbon nanotube electron source for field emission scanning electron microscopy. *e-Journal of Surface Science and Nanotechnology*, 9:400–403.

Naseh, M. V., Khodadadi, A. A., Mortazavi, Y., Pourfayaz, F., Alizadeh, O., and Maghrebi, M. (2010). Fast and clean functionalization of carbon nanotubes by dielectric barrier discharge plasma in air compared to acid treatment. *Carbon*, 48(5):1369 – 1379.

Natarajan, S., Lim, Z., Wee, G., Mhaisalkar, S., Sow, C.-H., and Ho, G. (2011). Electrically driven incandescence of carbon nanotubes in controlled gaseous environments. *Scripta Materialia*, 64(6):564 – 567.

Neira-Velázquez, M. G., Hernández-Hernández, E., Ramos-deValle, L. F., Ávila-Orta, C. A., Perera-Mercado, Y. A., Solís-Rosales, S. G., González-Morones, P., Ponce-Pedraza, A., Ávalos-Borja, M., Narro-Céspedes, R. I., and Bartolo-Pérez, P. (2013). Chemical modification of carbon nanofibers with plasma of acrylic acid. *Plasma Processes and Polymers*.

Neupane, S., Lastres, M., Chiarella, M., Li, W., Su, Q., and Du, G. (2012). Synthesis and field emission properties of vertically aligned carbon nanotube arrays on copper. *Carbon*, 50(7):2641 – 2650.

Nguyen, V. H. and Shim, J.-J. (2011). Facile synthesis and characterization of carbon nanotubes/silver nanohybrids coated with polyaniline. *Synthetic Metals*, 161(19):2078 – 2082.

Nishino, T., Ito, T., and Umezawa, Y. (2002). Carbon nanotube scanning tunneling microscopy tips for chemically selective imaging. *Analytical chemistry*, 74(16):4275–4278.

Nozaki, T., Yoshida, S., and Okazaki, K. (2012). Plasma-induced damage and surface functionalization of double-walled carbon nanotubes using atmospheric pressure rf discharge. *Plasma Processes and Polymers*.

Nyamori, V. O., Mhlanga, S. D., and Coville, N. J. (2008). The use of organometallic transition metal complexes in the synthesis of shaped carbon nanomaterials. *Journal of Organometallic Chemistry*, 693(13):2205 – 2222.

Odom, T. W., Huang, J.-L., and Lieber, C. M. (2002). Stm studies of single-walled carbon nanotubes. *Journal of Physics: Condensed Matter*, 14(6):R145.

Onwudili, J. A. and Williams, P. T. (2007). Reaction mechanisms for the decomposition of phenanthrene and naphthalene under hydrothermal conditions. *The Journal of Supercritical Fluids*, 39(3):399 – 408.

Osswald, S., Havel, M., and Gogotsi, Y. (2007). Monitoring oxidation of multi-walled carbon nanotubes by raman spectroscopy. *Journal of Raman Spectroscopy*, 38(6):728–736.

Ostrikov, K., Neyts, E. C., and Meyyappan, M. (2013). Plasma nanoscience: from nano-solids in plasmas to nano-plasmas in solids. *Advances in Physics*, 62(2):113–224.

Park, S., Vosguerichian, M., and Bao, Z. (2013). A review of fabrication and applications of carbon nanotube film-based flexible electronics. *Nanoscale*, 5:1727–1752.

Parker, V. (1970). Anodic oxidation of anthracenes and related compounds. *Acta Chemica Scandinavica*, 24:2757–2767.

Peng, H., Alemany, L. B., Margrave, J. L., and Khabashesku, V. N. (2003). Sidewall carboxylic acid functionalization of single-walled carbon nanotubes. *Journal of the American Chemical Society*, 125(49):15174–15182.

Peng, X. and Wong, S. S. (2009). Functional covalent chemistry of carbon nanotube surfaces. *Advanced Materials*, 21(6):625–642.

Purcell, S. T., Vincent, P., Journet, C., and Binh, V. T. (2002). Hot nanotubes: Stable heating of individual multiwall carbon nanotubes to 2000 k induced by the field-emission current. *Phys. Rev. Lett.*, 88:105502.

Qin, C. and Coulombe, S. (2007). Organic layer-coated metal nanoparticles prepared by a combined arc evaporation/condensation and plasma polymerization process. *Plasma Sources Science and Technology*, 16(2):240.

Radovic, L. R., Silva-Tapia, A. B., and Vallejos-Burgos, F. (2011a). Oxygen migration on the graphene surface. 1. origin of epoxide groups. *Carbon*, 49(13):4218 – 4225.

Radovic, L. R., Suarez, A., Vallejos-Burgos, F., and Sofo, J. O. (2011b). Oxygen migration on the graphene surface. 2. thermochemistry of basal-plane diffusion (hopping). *Carbon*, 49(13):4226 – 4238.

Ramos-deValle, L. F., Neira-Velázquez, M. G., and Hernández-Hernández, E. (2008). Surface modification of cnfs via plasma polymerization of styrene monomer and its effect on the properties of ps/cnf nanocomposites. *Journal of Applied Polymer Science*, 107(3):1893–1899.

Reisen, F. and Arey, J. (2002). Reactions of hydroxyl radicals and ozone with acenaphthene and acenaphthylene. *Environmental Science & Technology*, 36(20):4302–4311.

Ren, Z., Huang, Z., Xu, J., Wang, J., Bush, P., Siegal, M., and Provencio, P. (1998). Synthesis of large arrays of well-aligned carbon nanotubes on glass. *Science*, 282(5391):1105–1107.

Richter, H. and Howard, J. (2000). Formation of polycyclic aromatic hydrocarbons and their growth to soot—a review of chemical reaction pathways. *Progress in Energy and Combustion Science*, 26(4–6):565 – 608.

Rodriguez-Manzo, J. A. and Banhart, F. (2009). Creation of individual vacancies in carbon nanotubes by using an electron beam of 1 ådiameter. *Nano Letters*, 9(6):2285–2289.

Rodriguez-Manzo, J. A., Terrones, M., Terrones, H., Kroto, H. W., Sun, L., and Banhart, F. (2007). In situ nucleation of carbon nanotubes by the injection of carbon atoms into metal particles. *Nature Nanotechnology*, 2:307– 311.

Roldo, M. and Fatouros, D. G. (2013). Biomedical applications of carbon nanotubes. *Annual Reports Section" C"(Physical Chemistry)*.

Rotkin, S. V., Perebeinos, V., Petrov, A. G., and Avouris, P. (2009). An essential mechanism of heat dissipation in carbon nanotube electronics. *Nano letters*, 9(5):1850–1855.

Sahoo, S., Karthikeyan, G., Nayak, G. C., and Das, C. K. (2011). Electrochemical characterization of in situ polypyrrole coated graphene nanocomposites. *Synthetic Metals*, 161(15):1713–1719.

Saito, Y., Hata, K., Takakura, A., Yotani, J., and Uemura, S. (2002). Field emission of carbon nanotubes and its application as electron sources of ultra-high luminance light-source devices. *Physica B: Condensed Matter*, 323(1):30–37.

Schaper, A. K., Hou, H., Greiner, A., and Phillipp, F. (2004). The role of iron carbide in multiwalled carbon nanotube growth. *Journal of Catalysis*, 222(1):250 – 254.

Shi, D., Lian, J., He, P., Wang, L. M., van Ooij, W. J., Schulz, M., Liu, Y., and Mast, D. B. (2002). Plasma deposition of ultrathin polymer films on carbon nanotubes. *Applied Physics Letters*, 81(27):5216–5218.

Shi, Z., Lian, Y., Zhou, X., Gu, Z., Zhang, Y., Iijima, S., Zhou, L., Yue, K. T., and Zhang, S. (1999). Mass-production of single-wall carbon nanotubes by arc discharge method. *Carbon*, 37(9):1449 – 1453.

Shigi, H., Kishimoto, M., Yakabe, H., Deore, B., and Nagaoka, T. (2002). Highly selective molecularly imprinted overoxidized polypyrrole colloids: One-step preparation technique. *Analytical Sciences*, 18(1):41–44.

Shih, S.-I., Lin, T.-C., and Shih, M. (2005). Decomposition of benzene in the rf plasma environment: Part ii. formation of polycyclic aromatic hydrocarbons. *Journal of Hazardous Materials*, 117(2–3):149 – 159.

Shuaibov, A., General, A., Kel'man, V., and Shevera, I. (2008). The emission characteristics of low-pressure water vapor discharge uv emitters. *Technical Physics Letters*, 34:588–590.

Shuaibov, A., Heneral, A., Shpenik, Y., Zhmenyak, Y., Shevera, I., and Gritsak, R. (2009). Ultraviolet radiation sources on (h_2o, d_2o) water vapor. *Technical Physics*, 54:1238–1240. 10.1134/S1063784209080258.

Silva-Tapia, A. B., García-Carmona, X., and Radovic, L. R. (2012). Similarities and differences in o_2 chemisorption on graphene nanoribbon vs. carbon nanotube. *Carbon*, 50(3):1152 – 1162.

Suhr, H. (1972). Organic syntheses in the plasma of glow discharges and their preparative application. *Angewandte Chemie International Edition in English*, 11(9):781–792.

Suuberg, E., Wojtowicz, M., and Calo, J. (1989). Reaction order for low temperature oxidation of carbons. *Symposium (International) on Combustion*, 22(1):79 – 87.

Sveningsson, M., Morjan, R.-E., Nerushev, O. A., Sato, Y., Bäckström, J., Campbell, E. E., and Rohmund, F. (2001). Raman spectroscopy and field-emission properties of cvd–grown carbon-=nanotube films. *Applied Physics A*, 73(4):409–418.

Tang, Q., Zhou, Z., and Chen, Z. (2013). Graphene-related nanomaterials: tuning properties by functionalization. *Nanoscale*, 5:4541–4583.

Tasis, D., Tagmatarchis, N., Bianco, A., and Prato, M. (2006). Chemistry of carbon nanotubes. *Chemical Reviews*, 106(3):1105–1136.

Tavares, J., Swanson, E. J., and Coulombe, S. (2008). Plasma synthesis of coated metal nanoparticles with surface properties tailored for dispersion. *Plasma Processes and Polymers*, 5(8):759–769.

Taylor, R., Coulombe, S., Otanicar, T., Phelan, P., Gunawan, A., Lv, W., Rosengarten, G., Prasher, R., and Tyagi, H. (2013). Small particles, big impacts: A review of

the diverse applications of nanofluids. *Journal of Applied Physics*, 113(1):011301–011301.

Thejaswini, H., Majumdar, A., Tun, T., and Hippler, R. (2011). Plasma chemical reactions in c_2h_2/n_2, c_2h_4/n_2, and c_2h_6/n_2 gas mixtures of a laboratory dielectric barrier discharge. *Advances in Space Research*, 48(5):857–861.

Tong, D., Luo, Y., Chu, W., Guo, Y., and Tian, W. (2010). Cutting of carbon nanotubes via solution plasma processing. *Plasma Chemistry and Plasma Processing*, 30:897–905.

Tsakadze, Z., Ostrikov, K., Sow, C., Mhaisalkar, S., and Boey, Y. (2010). Effect of gas pressure on electron field emission from carbon nanotube forests. *Journal of Nanoscience and Nanotechnology*, 10(10):6575–6579.

Tseng, W.-S., Tseng, C.-Y., and Kuo, C.-T. (2009). Effects of gas composition on highly efficient surface modification of multi-walled carbon nanotubes by cation treatment. *Nanoscale Research Letters*, 4(3):234–239.

Tsukamoto, A. and Lichtin, N. N. (1960). Non-degradative reaction of active nitrogen with conjugated dienes1. *Journal of the American Chemical Society*, 82(14):3798–3799.

Vandsburger, L., Coulombe, S., and Meunier, J. (2013a). Degradation of carbon nanotubes in oxygen glow discharges. *Carbon*, 57(0):248 – 258.

Vandsburger, L., Coulombe, S., and Meunier, J.-L. (2013b). Degradation of carbon nanotubes by electron bombardment in radio-frequency glow discharge afterglows. *Journal of Physics D: Applied Physics*, 46(48):485301.

Vandsburger, L., Swanson, E., Tavares, J., Meunier, J.-L., and Coulombe, S. (2009). Stabilized aqueous dispersion of multi-walled carbon nanotubes obtained by rf glow-discharge treatment. *Journal of Nanoparticle Research*, 11:1817–1822.

Vasil'eva, E., Kleshch, V., and Obraztsov, A. (2012). Effect of vacuum level on field emission from nanographite films. *Technical Physics*, 57(7):1003–1007.

Veilleux, J. and Coulombe, S. (2010). A total internal reflection fluorescence microscopy study of mass diffusion enhancement in water-based alumina nanofluids. *Journal of Applied Physics*, 108(10):104316–104316.

Voevodin, A. A., Jones, J. G., Zabinski, J. S., and Hultman, L. (2002). Plasma characterization during laser ablation of graphite in nitrogen for the growth of fullerene-like cn[sub x] films. *Journal of Applied Physics*, 92(2):724–735.

Vohrer, U., Zschoerper, N. P., Koehne, Y., Langowski, S., and Oehr, C. (2007). Plasma modification of carbon nanotubes and bucky papers. *Plasma Processes and Polymers*, 4(S1):S871–S877.

Wang, B., Puzyrev, Y. S., and Pantelides, S. T. (2013). Enhanced chemical reactions of oxygen at grain boundaries in polycrystalline graphene. *Polyhedron*, (0):–.

Wang, B. B., Cheng, Q. J., Zhong, X. X., Wang, Y. Q., Chen, Y. A., and Ostrikov, K. (2012). Enhanced electron field emission from plasma-nitrogenated carbon nanotips. *Journal of Applied Physics*, 111(4):044317.

Wang, F., Chen, X., and Chen, Z. (2011a). Eletrodeposited nickel oxide on a film of carbon nanotubes for monitoring nitric oxide release from rat kidney and drug samples. *Microchimica Acta*, 173(1-2):65–72.

Wang, J. (2005). Carbon-nanotube based electrochemical biosensors: A review. *Electroanalysis*, 17(1):7–14.

Wang, J., Ma, L., Yuan, Q., Zhu, L., and Ding, F. (2011b). Transition-metal-catalyzed unzipping of single-walled carbon nanotubes into narrow graphene nanoribbons at low temperature. *Angewandte Chemie International Edition*, 50(35):8041–8045.

Wang, Q., Cheng, Y., Wang, L., and Li, X. (2007). Semicontinuous studies on the reaction mechanism and kinetics for the liquid-phase oxidation of p-xylene to terephthalic acid. *Industrial & Engineering Chemistry Research*, 46(26):8980–8992.

Wang, Z., Gao, R., de Heer, W., and Poncharal, P. (2002). In situ imaging of field emission from individual carbon nanotubes and their structural damage. *Applied Physics Letters*, 80(5):856–858.

Wildgoose, G. G., Banks, C. E., Leventis, H. C., and Compton, R. G. (2006). Chemically modified carbon nanotubes for use in electroanalysis. *Microchimica Acta*, 152(3-4):187–214.

Wu, T.-M., Lin, Y.-W., and Liao, C.-S. (2005). Preparation and characterization of polyaniline/multi-walled carbon nanotube composites. *Carbon*, 43(4):734 – 740.

Xie, G., Sueishi, Y., and Yamamoto, S. (2005). Analysis of the effects of protic, aprotic, and multi-component solvents on the fluorescence emission of naphthalene and its exciplex with triethylamine. *Journal of Fluorescence*, 15:475–483.

Xu, L., Fang, Z., Song, P., and Peng, M. (2010). Functionalization of carbon nanotubes by corona-discharge induced graft polymerization for the reinforcement of epoxy nanocomposites. *Plasma Processes and Polymers*, 7(9-10):785–793.

Xu, Y., Jiang, Y., Cai, H., He, P.-G., and Fang, Y.-Z. (2004). Electrochemical impedance detection of dna hybridization based on the formation of m-dna on polypyrrole/carbon nanotube modified electrode. *Analytica Chimica Acta*, 516(1):19 – 27.

Yasuda, H. (1985). *Plasma Polymerization*, page 419. Academic Press.

Ye, Y., Mao, Y., Wang, F., Lu, H., Qu, L., and Dai, L. (2011). Solvent-free functionalization and transfer of aligned carbon nanotubes with vapor-deposited polymer nanocoatings. *J. Mater. Chem.*, 21:837–842.

Yu, W. J., Lee, S. Y., Chae, S. H., Perello, D., Han, G. H., Yun, M., and Lee, Y. H. (2011). Small hysteresis nanocarbon-based integrated circuits on flexible and transparent plastic substrate. *Nano Letters*, 11(3):1344–1350.

Yu, Y., Che, B., Si, Z., Li, L., Chen, W., and Xue, G. (2005). Carbon nanotube/polyaniline core-shell nanowires prepared by in situ inverse microemulsion. *Synthetic metals*, 150(3):271–277.

Zelikman, E., Narkis, M., Siegmann, A., Valentini, L., and Kenny, J. M. (2008). Polyaniline/multiwalled carbon nanotube systems: Dispersion of cnt and cnt/pani interaction. *Polymer Engineering & Science*, 48(10):1872–1877.

Zerbi, G., Veronelli, M., Martina, S., Schlüter, A., and Wegner, G. (1994). Delocalization length and structure of oligopyrroles and of polypyrrole from their vibrational spectra. *The Journal of chemical physics*, 100:978.

Zhang, B., Xu, Y., Zheng, Y., Dai, L., Zhang, M., Yang, J., Chen, Y., Chen, X., and Zhou, J. (2011a). A facile synthesis of polypyrrole/carbon nanotube composites with ultrathin, uniform and thickness-tunable polypyrrole shells. *Nanoscale Research Letters*, 6(1):1–9.

Zhang, L., Feng, C., Chen, Z., Liu, L., Jiang, K., Li, Q., and Fan, S. (2008). Super-aligned carbon nanotube grid for high resolution transmission electron microscopy of nanomaterials. *Nano Letters*, 8(8):2564–2569.

Zhang, X., Zhang, J., Wang, R., Zhu, T., and Liu, Z. (2004). Surfactant-directed polypyrrole/cnt nanocables: Synthesis, characterization, and enhanced electrical properties. *ChemPhysChem*, 5(7):998–1002.

Zhang, Y., Liao, M., Deng, S., Chen, J., and Xu, N. (2011b). In situ oxygen-assisted field emission treatment for improving the uniformity of carbon nanotube pixel arrays and the underlying mechanism. *Carbon*, 49(10):3299 – 3306.

Zhang, Y.-F. and Liu, Z.-F. (2006). Pressure induced reactivity change on the side-wall of a carbon nanotube: A case study on the addition of singlet o_2. *Carbon*, 44(5):928 – 938.

Zhao, B., Zhang, L., Wang, X., and Yang, J. (2012a). Surface functionalization of vertically-aligned carbon nanotube forests by radio-frequency ar/o_2 plasma. *Carbon*, 50(8):2710–2716.

Zhao, C., Ji, L., Liu, H., Hu, G., Zhang, S., Yang, M., and Yang, Z. (2004). Functionalized carbon nanotubes containing isocyanate groups. *Journal of Solid State Chemistry*, 177(12):4394–4398.

Zhao, H., Xu, W., Song, L., Mei, Q., Chen, C., Miao, L., and Jiang, J. (2012b). External electric field induced oxygen-driven unzipping of carbon nanotubes. *Journal of Applied Physics*, 112(7):074316 –074316–5.

Zhao, X., Ando, Y., Qin, L.-C., Kataura, H., Maniwa, Y., and Saito, R. (2002). Ra-